Particle Simulation of Lower Hybrid Waves and Electron-ion Hybrid Instability

by

Lei Qi

A dissertation submitted to the Graduate Faculty of
Auburn University
in partial fulfillment of the
requirements for the Degree of
Doctor of Philosophy

Auburn, Alabama
May 03, 2014

Keywords: Particle simulation, Landau damping, Lower Hybrid Wave, parametric instability, Electron-ion hybrid (EIH) instability

Approved by

Yu Lin, Chair, Professor of Physics
J.D. Perez, Professor of Physics
Thomas H. Pate, Professor of Mathematics
Edward Thomas, Jr., Professor of Physics
Kaijun Liu, Assistant Professor of Physics

Abstract

Lower hybrid wave (LHW) has been of great interest to laboratory plasma physics for decades due to its important applications in particles heating and current drive in plasmas devices. There are two fundamental characteristics of LHWs, Landau damping and parametric instability (PI), both of which play key roles in particles heating and current drive problems. Linear physics of LHWs has been studied in great details in analytical theories, while nonlinear physics is usually too complicated to be resolved analytically. Computer kinetic simulation technique has developed to be one of the best tools for the investigation of kinetic physics, especially in the nonlinear stage. Although a great amount of theoretical work has been done in the investigation of LHWs, little particle simulation work can be found in published literatures. In this thesis, an electrostatic gyro-kinetic electron and fully kinetic ion (GeFi) particle simulation scheme is utilized to study the linear and nonlinear physics of LHWs. GeFi model is particularly suitable for plasma dynamics with wave frequencies lower than the electron gyrofrequency, and for problems in which the wave modes ranging from Alfvén waves to lower-hybrid/whistler waves that need to be handled on an equal footing with realistic electron-to-ion mass ratio.

Firstly, Interactions of LHWs with both electrons and ions through nonlinear Landau damping, as well as linear Landau damping, is investigated by utilization of GeFi particle simulation in electrostatic limit. Landau damping, a wave-particle interaction process, provides a way for LHWs to exchange energy and momentum with electrons and ions, thus to heat plasmas and generate electric currents in the plasmas. Unlike most other wave modes, LHWs can resonantly interact with both electrons and ions, with the former being highly magnetized and the latter being

nearly unmagnetized around lower hybrid frequency. Direct interactions of LHWs with electrons and/or ions are investigated for cases with various $k_{\|}/k$, T_i/T_e, and wave amplitudes. Here, k is wave vector, $k_{\|}$ is parallel (to static magnetic field) wave vector, T_i and T_e are ion and electron temperatures, respectively. In the linear electron Landau damping (ELD), real frequencies and damping rates obtained from our kinetic simulations have excellent agreement with the analytical linear dispersion relation. As wave amplitude increases, the nonlinear Landau effects are present, and a transition from strong decay at smaller amplitudes to weak decay at larger amplitudes is observed. In the nonlinear stage, LHWs in a long time evolution finally exhibit a steady BGK mode, in which the wave amplitude is saturated above noise level. While resonant electrons are trapped in the wave electric field in the nonlinear ELD, resonant ions are untrapped in LHWs time scales. Ion Landau damping is thus predominantly in a linear fashion, leading to a wave saturation level significantly lower than that in the ELD. On long time scales, however, ions are still weakly trapped. Simulation results show a coupling between LHW frequency and ion cyclotron frequency during the long-time LHW evolution.

Secondly, our investigation extends to a transverse sheared flow driven instability, electron-ion hybrid (EIH) instability, whose frequency is in the lower hybrid frequency range. EIH instability is studied by the GeFi model in a magnetized plasma with a localized electron cross-field flow. Macroscopic flows are commonly encountered in various plasmas, such as plasmas in tokamak devices, laser-produced plasmas, Earth's magnetopause, plasma sheet boundary layer, and the Earth's magnetotail. As a benchmark, linear simulations of EIH are firstly performed in both slab geometry and cylindrical geometry with $k_z = 0$ in either uniform plasmas or nonuniform plasmas, and the results are compared with linear theories in a slab geometry. Here for the slab geometry, static magnetic field is at z axis, and electron shear flow as a function of x is put at y axis. And in the cylindrical geometry, static magnetic field is also

at z direction, while electron shear flow as a function of radial position r is in θ (poloidal) direction. Linear eigen mode structures and growth rates of EIH instability are calculated for various $k_y L$, $\alpha_1 = V_E^0/L\Omega_e$, and L/L_n. Here k_y (k_z) is the wave vector in y (z) direction, L the shear length of electric field, V_E^0 the peak value of the $\mathbf{E} \times \mathbf{B}$ drift velocity, Ω_e the electron gyro frequency, L_n the scale of density gradients. The results have very good agreement with the theoretical predications. Nonlinear simulations are performed to investigate the nonlinear evolution of EIH instabitly. It is found that the EIH instability nonlinearly evolves from a short wave length ($k_x\rho_i \sim 12$) mode to a long wave length ($k_x\rho_i \sim 3$) mode with frequency $\sim \omega_{LH}$. Simulation results under realistic plasma conditions of the Auburn Linear Experiment for Instability Studies (ALEXIS) device are discussed and compared with ALEXIS experimental results as well.

Finally, parametric instability of LHWs is investigated using the GeFi model. Parametric instability is a nonlinear process that involves wave-wave interactions, and is of great interest. In the propagation of LHWs, a pump LHW $(\omega_0, \mathbf{k_0})$ decays into a low frequency wave mode $(\omega, \mathbf{k})$ and two high frequency sidebands $(\omega \pm \omega_0, \mathbf{k} \pm \mathbf{k_0})$, where ω represent the wave frequency, $\mathbf{k}$ represent the wave vector, and the subscript "0" indicates the pump wave. Two different cases with parametric instability are discussed in great details. The parametric decay process is found to occur very fast within several lower hybrid wave periods. Growth rates of the excited modes are estimated as well, and results are compared with the analytical theory. The simulation shows that the parametric instability process is complicated due to multiple decay channels. These multiple parametric instability processes usually occur simultaneously. The corresponding electron and ion particle distributions are investigated in the decay process. Finally, a discussion is presented for the future study of electron and ion nonlinear physics of the PI instability.

Acknowledgments

I would like to express my great gratitudes to my supervisor Dr. Yu Lin for her patient guidance in my research work. Without her, I would never be able to complete my research program. I am also greatly appreciative of helpful discussions with my collaborator Dr. Xueyi Wang.

Table of Contents

List of Figures

List of Tables

Chapter 1

An Introduction of Lower Hybrid Waves and Their Landau Damping and Parametric Instability

The existence of a damping mechanism by which plasma particles absorb wave energy even in a collisionless plasma was found by L.D. Landau[1], under the condition that the plasma is not cold and the velocity distribution is of finite extent. Energy-exchange processes between particles and waves play important roles in plasma heating by waves and in the mechanism of instabilities. Previous investigation of Landau damping mechanism mainly used Langmuir waves, typical electrostatic longitudinal plasma waves. Electrostatic lower hybrid wave (LHW) is a preferable source to heat both electrons and ions to the thermonuclear temperature and generate electric currents in plasmas under Landau damping. Thus the Landau damping of LHWs is fundamentally important. In this chapter, I will introduce and give an overview of linear dispersion relation of LHWs, Landau damping theory, theory of Landau damping of LHWs, and theory of parametric instability (PI).

1.1 Introduction of Lower Hybrid Waves

Lower hybrid wave is of great interest for decades due to its important applications in the magnetic controlled fusion devices. Electrostatic LHW is a potential source to heat both electrons and ions to thermonuclear temperature and generate electric currents[50] in plasma fusion devices. LHWs have been investigated extensively in linear theories[16, 17, 18], nonlinear parametric instability theories[19, 20, 21], and experiments[22]. Some experiments were performed to heat electrons in plasmas by the direct electron Landau interactions in the lower hybrid

waves[23, 24, 25], and a sufficiently high increase of the electron temperature was obtained. In this section, an introduction of the lower hybrid waves are presented, including electromagnetic dispersion relation in a cold plasma, electrostatic dispersion relation in a cold plasma, and dispersion relations in warm plasmas.

1.1.1 Electromagnetic dispersion relation in a cold plasma

Consider a plasma with density gradient in the x direction $N(x)$, an external static magnetic field in the z direction $\mathbf{B_0} = B_0\mathbf{e_z}$, unperturbed electric field $\mathbf{E_0} = 0$, and unperturbed electron and ion fluid velocities $\mathbf{v_{e0}} = \mathbf{0}$ and $\mathbf{v_{i0}} = \mathbf{0}$. The perturbed electric field $\mathbf{E}$, magnetic field $\mathbf{B}$, and the current density $\mathbf{J}$ are then described by Maxwell's equations

$$\nabla \times \mathbf{B} = \mu_0\epsilon_0\frac{\partial \mathbf{E}}{\partial t} + \mu_0\mathbf{J} \tag{1.1}$$

$$\nabla \times \mathbf{E} = -\frac{\partial \mathbf{B}}{\partial t}. \tag{1.2}$$

Assuming that the wave fields vary as a wave, i.e., $\exp[i(\mathbf{k}\cdot\mathbf{x} - \omega t)]$ and the WKB approximation ($|\mathbf{k}| \gg |\partial/\partial\mathbf{x}|$). Eqs. 1.1 and 1.2 can be analyzed by Fourier methods in space and time

$$-\mathbf{k}\times\mathbf{k}\times\mathbf{E} = (\omega/c)^2\mathbf{E} + i\omega\mu_0\mathbf{J}. \tag{1.3}$$

Where $\mathbf{J} = Ne(\mathbf{v_i} - \mathbf{v_e})$, with the electron (ion) velocity $\mathbf{v_e}$ ($\mathbf{v_i}$) governed by the equations of motion

$$m_e\frac{\partial \mathbf{v_e}}{\partial t} = -e(\mathbf{E} + \mathbf{v_e}\times\mathbf{B_0}) \tag{1.4}$$

$$m_i\frac{\partial \mathbf{v_i}}{\partial t} = e(\mathbf{E} + \mathbf{v_i}\times\mathbf{B_0}) \tag{1.5}$$

Combining Eqs. 1.3, 1.4 and 1.5, it yields the following equations

$$\mathbf{k}\times\mathbf{k}\times\mathbf{E} + (\omega/c)^2\bar{\epsilon}\cdot\mathbf{E} = 0, \tag{1.6}$$

$$\bar{\epsilon} = \begin{pmatrix} \epsilon_\perp & -i\epsilon_{xy} & 0 \\ i\epsilon_{xy} & \epsilon_\perp & 0 \\ 0 & 0 & \epsilon_\parallel \end{pmatrix}. \tag{1.7}$$

$\bar{\epsilon}$ is so called the cold plasma dielectric tensor. Taking the approximations that the LHW's frequency $\Omega_i \ll \omega \ll \Omega_e$, where $\Omega_e = eB_0/m_e$ ($\Omega_i = eB_0/m_i$) is the electron (ion) cyclotron frequency, one can obtain the elements of the tensor

$$\epsilon_\perp = 1 + (\omega_{pe}/\Omega_e)^2 - (\omega_{pi}/\omega)^2, \tag{1.8}$$

$$\epsilon_\parallel = 1 - (\omega_{pe}/\omega)^2 - (\omega_{pi}/\omega)^2, \tag{1.9}$$

$$\epsilon_{xy} = \omega_{pe}^2/(\omega\Omega_e). \tag{1.10}$$

Note that $\omega_{pe} = \sqrt{Ne^2/\varepsilon_0 m_e}$ ($\omega_{pi} = \sqrt{Ne^2/\varepsilon_0 m_i}$) is the electron (ion) plasma frequency. Eq. 1.6 can be written in another form as

$$\bar{\mathbf{D}} \cdot \mathbf{E} = 0, \tag{1.11}$$

$$\bar{\mathbf{D}} = \mathbf{k} \times \mathbf{k} \times \bar{\mathbf{I}} + (\omega/c)^2 \bar{\epsilon}. \tag{1.12}$$

Let the determinant of $\bar{\mathbf{D}}$ vanish to obtain the nontrivial solutions to Eq. 1.11. This results in the LHW electromagnetic dispersion relation in a cold plasma

$$\begin{aligned} D_0(\mathbf{x}, \mathbf{k}, \omega) &= \det(\bar{\mathbf{D}}) = P_4 n_\perp^4 + P_2 n_\perp^2 + P_0 = 0 \\ P_0 &= \epsilon_\parallel[(n_\parallel^2 - \epsilon_\perp)^2 - \epsilon_{xy}^2] \\ P_2 &= (\epsilon_\perp + \epsilon_\parallel)(n_\parallel^2 - \epsilon_\perp) + \epsilon_{xy}^2 \\ P_4 &= \epsilon_\perp, \end{aligned} \tag{1.13}$$

where $n_\parallel = k_\parallel c/\omega$, $n_\perp = k_\perp c/\omega$, $k_\parallel$ ($k_\perp$) is the component of the wave vector parallel (perpendicular) to the external static magnetic field. Here and through this thesis, $\parallel$ ($\perp$) denotes the component parallel (perpendicular) to the static magnetic field. Eq. 1.13 indicates two wave modes in terms of $n_\perp$. By solving $n_\perp^2$ in Eq. 1.13, one can obtain

$$n_\perp^2 = \frac{1}{2P_4}(-P_2 \pm \Delta^{1/2}), \tag{1.14}$$

with $\Delta = (P_2)^2 - 4P_0P_4$. The positive sign in Eq. 1.14 corresponds to the "slow" wave branch (small $\omega/k_\perp$), and the minus sign corresponds to the "fast" wave branch. The slow wave branch has a cold plasma resonance condition $P_4 \to 0$, from which the lower hybrid wave frequency can be defined as $\omega_{LH} = \omega_{pi}/\sqrt{1+\omega_{pe}^2/\Omega_e^2}$. The slow wave branch of the dispersion relation, is typically associated with the lower hybrid wave.

Fig 1.1 shows the plots of $n_\perp^2$ versus density $N(x)$ for three different values of $n_\parallel$. Note that there is a critical value $n_\parallel = n_c$. Fig 1.1(a) shows there exists mode conversions between the slow wave mode and the fast wave mode with the condition $n_\parallel < n_c$. A wave launched at the slow wave cutoff N_S will mode convert into the fast wave mode at a density denoted as N_{T1}. With $n_\parallel > n_c$, as plotted in Fig 1.1(c), a wave launched at the slow wave cutoff will propagate to its resonance without converting to the fast wave. $n_\parallel = n_c$ is the lowest value for the slow wave mode to propagate from its cutoff to the maximum plasma density in the presence of density gradient without mode conversion to the fast wave, as plotted in Fig 1.1(b).

1.1.2 Electrostatic dispersion relation in a cold plasma

The wave polarization is essentially electrostatic ($kc/\omega \gg 1$) when the LHW propagates at densities much greater than cutoff densities N_S and N_F. Thus, to consider propagations of the electrostatic LHW nearly perpendicular to the magnetic

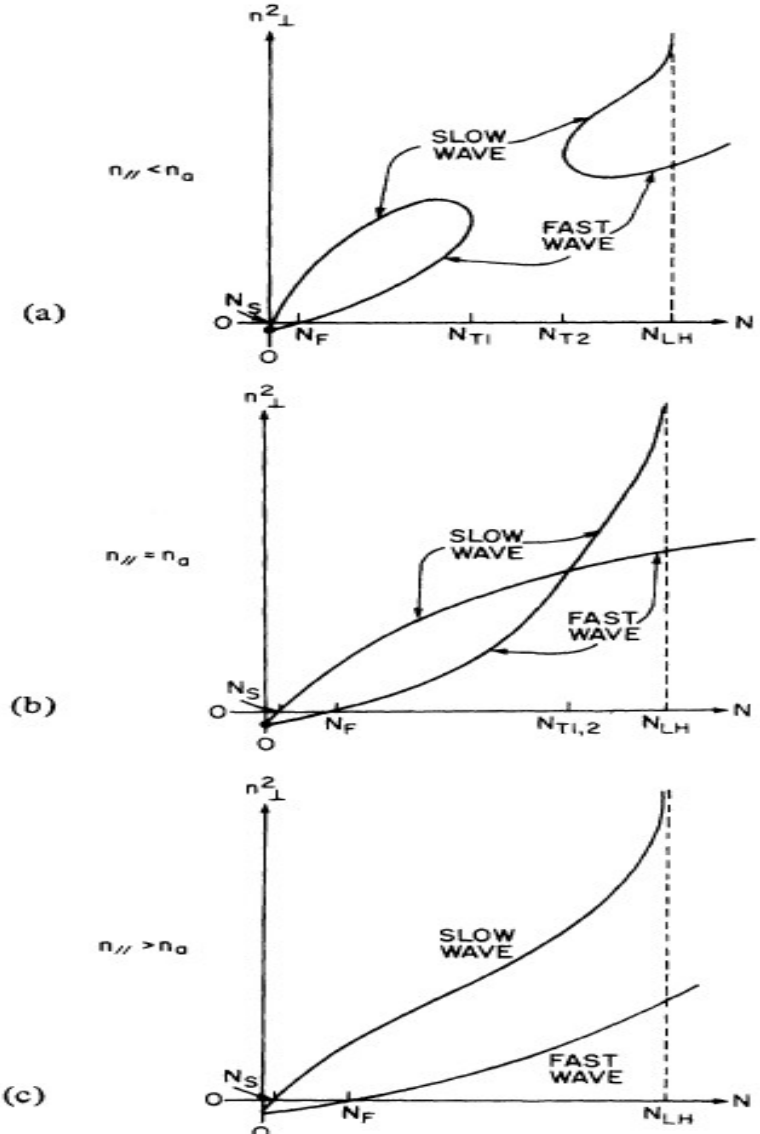

Figure 1.1: $n_\perp^2$ versus N for fixed $n_\parallel$, N_S (N_F) denotes the cutoff density to the slow (fast) wave.[Figure is from: Paul Bonoli, IEEE Transactions on plasma science, Vol. PS-12, NO. 2, June 1984.]

field, the dispersion relation can be obtained from Eq. 1.13

$$D_0(\mathbf{x}, \mathbf{k}, \omega) = k_\parallel^2 \epsilon_\parallel + k_\perp^2 \epsilon_\perp = 0. \tag{1.15}$$

Given the condition $k_\parallel \ll k_\perp$, the above dispersion relation can be reduced to

$$\omega^2 = \omega_{LH}^2 (1 + \frac{m_i}{m_e} \frac{k_\parallel^2}{k^2}). \tag{1.16}$$

Let us now understand the main features of Eqs. 1.15 and 1.16. Evaluation of $\partial\omega/\partial k_\perp$ shows that the wave is backward in the perpendicular direction (to static magnetic field) [i.e., $(\partial\omega/\partial k_\perp)(\omega/k_\perp) < 0$]. The dispersion relation also shows that, $k_\perp$ increases as the wave propagates into regions of increasing plasma density, when there exists a density gradient in the $\perp$ direction. In particular, for a fixed $k_\parallel$, $k_\perp$ becomes very large as the wave reaches regions, where the local lower hybrid frequency ω_{LH} is close to the wave frequency, ω. Mode conversion can occur near the lower hybrid layer.[26]

Resonance cones

Another interesting characteristic of the propagation of the electrostatic LHW is that point sources excite LHWs to propagate in resonance cones. To consider that a point source excites an electrostatic disturbance in a plasma with frequency and wave number $(\omega, \mathbf{k})$, satisfying the dispersion relation Eq. 1.15. For simplicity, take $\mathbf{k} = k_\perp \mathbf{e_x} + k_\parallel \mathbf{e_z}$ and $\mathbf{E} = -\nabla\phi$, where $\phi \sim \exp[i(k_\perp x + k_\parallel z - \omega t)]$. Then the Fourier transformation in Eq. 1.15 my be inverted to give

$$\frac{\partial^2 \phi}{\partial x^2} = -\frac{\epsilon_\parallel}{\epsilon_\perp} \frac{\partial^2 \phi}{\partial z^2}. \tag{1.17}$$

This equation is similar to the typical wave differential equation

$$\frac{\partial^2\psi}{\partial t^2} = C^2\frac{\partial^2\psi}{\partial z^2}. \tag{1.18}$$

The solutions of Eq. 1.18 propagate along the characteristics $z \pm Ct$. In analogous fashion, the solutions of Eq. 1.17 propagate along characteristics $z \pm (-\epsilon_\parallel/\epsilon_\perp)^{1/2}x$. These are the resonance cones, in which there exists the propagation of a singular electrostatic disturbance excited by a point source and obeying the LHW dispersion relation.

1.1.3 LHW dispersion relations in warm plasmas

Both the electromangetic and electrostatic LHW dispersion relations in a cold plasma were discussed in the previous introductions. Here, to include the warm plasma effects, both the electromagnetic and electrostatic LHW dispersion relations will be briefly reviewed. It is assumed that $\omega_{pe} \gg \Omega_e \gg \omega \gg \Omega_i$, $k^2V_{te}^2/\Omega_e^2 \ll 1$ with $V_{te} = \sqrt{\kappa T_e/m_e}$ the electron thermal speed, and the ions are singled charged, $m_e \ll m_i$. θ is defined to be the angle between $\mathbf{k}$ and $\mathbf{B}$, thus $\cos(\theta) = k_\parallel/k \sim m_e/m_i$ In the dispersion relation, terms are kept to the first order of $k^2V_{te}^2/\Omega_e^2$ and to all orders of the electromagnetic term ω_{pe}^2/k^2c^2. The LHW dispersion relation with both electromagnetic and warm effects included is found to be[27]

$$\omega^2 = \frac{\omega_{LH}^2}{1+\omega_{pe}^2/k^2c^2}[1 + \frac{(m_i/m_e)\cos^2(\theta)}{1+\omega_{pe}^2/k^2c^2} + W\frac{k^2V_{te}^2}{\Omega_e^2}], \tag{1.19}$$

$$\begin{aligned} W &= 3\frac{T_i}{T_e}(1+\frac{\omega_{pe}^2}{k^2c^2}) + \frac{\omega_{pe}^2}{2k^2c^2} + \frac{9}{2} - \frac{15+21\omega_{pe}^2/k^2c^2}{4(1+\omega_{pe}^2/k^2c^2)^2} \\ &- [3\frac{\omega_{pe}^2}{k^2c^2} + \frac{1-6\omega_{pe}^2/k^2c^2}{4(1+\omega_{pe}^2/k^2c^2)^2}]\frac{m_i}{m_e}\cos^2(\theta) \end{aligned}$$

$$+ \quad 3\frac{(m_i/m_e)\cos^2(\theta) + \omega_{pe}^2/k^2c^2 - T_i/T_e}{1 + \omega_{pe}^2/k^2c^2 + (m_i/m_e)\cos^2(\theta)}(1 + \frac{\omega_{pe}^2}{k^2c^2})\frac{m_i}{m_e}\cos^2(\theta). \qquad (1.20)$$

In the limit that ω_{pe}^2/k^2c^2 tends to zero and $(m_i/m_e)\cos^2(\theta)$ is small, the LHWs become longitudinal and nearly electrostatic, and $W = 3T_i/T_e + 3/4$ to lowest order. The dispersion relation for electrostatic LHW in a warm plasma becomes

$$\omega^2 = \omega_{LH}^2(1 + \frac{m_e}{m_e}\cos^2(\theta) + 3(\frac{T_i}{T_e} + \frac{1}{4})\frac{k^2V_{te}^2}{\Omega_e^2}). \qquad (1.21)$$

To include the electromagnetic effects, in the limit that ω_{pe}^2/k^2c^2 and $(m_i/m_e)\cos^2(\theta)$ are both small, the dispersion relation for the electromagnetic LHW in a warm plasma is found to be

$$\omega^2 = \omega_{LH}^2(1 + \frac{m_e}{m_e}\cos^2(\theta) - \frac{\omega_{pe}^2}{2k^2c^2} + 3(\frac{T_i}{T_e} + \frac{1}{4})\frac{k^2V_{te}^2}{\Omega_e^2}). \qquad (1.22)$$

There are several more expressions of the approximate dispersion relation of the LHW. If the plasma is treated as being cold and EM effects are included, the resulting dispersion relation is[28]

$$\frac{\omega^2}{\omega_{LH}^2} = \frac{1}{1 + \omega_{pe}^2/k^2c^2}(1 + \frac{m_i}{m_e})\frac{\cos^2(\theta)}{1 + \omega_{pe}^2/k^2c^2}. \qquad (1.23)$$

This expression makes no assumption on the size of ω_{pe}^2/k^2c^2.

Another LHW dispersion relation, adopted by Bingham et al.[29], includes both warm plasma and EM effects, but assumes that ω_{pe}^2/k^2c^2 is small and includes terms only to first order in $(m_i/m_e)\cos^2(\theta)$, ω_{pe}^2/k^2c^2 and $k^2V_{te}^2/\Omega_e^2$.

$$\frac{\omega}{\omega_{LH}} = 1 + \frac{m_i}{2m_e}\cos^2(\theta) - \frac{\omega_{pe}^2}{k^2c^2} + (\frac{3T_i}{2T_e} + 1)\frac{k^2V_{te}^2}{\Omega_e^2}. \qquad (1.24)$$

Note that the last term in the above dispersion relation is not equal to half of the last term of Eq. 1.21 (or Eq. 1.22), although in the limit of $\omega_{pe}^2/k^2c^2 \to 0$ they should be equal.

1.2 Landau damping

Landau damping is a fundamental plasma process in which small perturbations in a uniform, Maxwellian, electrostatic plasma are exponentially damped, even when no dissipative terms are present. Landau damping process can be categorized as linear Landau damping and nonlinear Landau damping according to different time scales, which will be discussed in details later. The nonlinear Landau damping has distinctive characteristics that are quite different from the linear Landau damping. The linear Landau damping of Langmuir waves was extensively investigated in 50's and 60's and well understood. The nonlinear Landau damping, however, was not well understood. Recent Landau damping experiments[7] and plasma simulations[5, 6] revealed new important physics of Landau damping of Langmuir waves for long time evolution.

1.2.1 Liner Landau damping

The Landau damping process was found by Landau in 1946. Since then, linear Landau damping has been extensively confirmed in both experiments[8] and computer simulations[9]. The Landau damping, especially the linear Landau damping is a standard topic in most plasma physics textbooks (e.g., [10, 11]), mainly for Langmuir wave. The linear Landau theory leads to the damping coefficient [1, 2] for the collisionless damping of longitudinal electron plasma oscillations

$$\frac{\gamma_L}{\omega} = \frac{\pi}{2}\frac{\omega_{pe}^2}{k^2}\frac{\partial f}{\partial v}\Big|_{v=\omega/k}, \tag{1.25}$$

where ω is real frequency of the electron plasma wave, ω_{pe} is the electron plasma frequency, k is the wave number, and f is the velocity distribution function of electrons. The physical interpretation of this collisionless damping is that the electron plasma wave resonates with the electrons, which possess phase velocity $v = \omega/k$, and loses energy to the electrons. However, Landau's treatment of the problem is rigorous, but strictly linear.

The linear theory will break down after a time $\tau = \sqrt{m_e/eEk}$, where m_e is the electron mass, e is electron charge, and E is the amplitude of the electric field. In other words, if the linear damping rate γ_L is comparable to $2\pi/\tau$, the initial decay of the electron plasma wave will soon turn into nonlinear Landau damping, characterized as a nonlinear oscillation due to particle trapping with the oscillation amplitude somewhat lower than the initial value[12, 13].

1.2.2 Nonlinear Landau damping

The linear Landau damping was researched thoroughly in theory, experiments and kinetic simulations. Nevertheless, the nonlinear Landau damping is still poorly understood. There are no exact analytical solutions of the nonlinear Landau damping, but only some approximate ones[2]. The early theory, presented by O'Neil, predicted phase mixing and amplitude oscillations for the electric field, which have indeed been demonstrated in simulations and experiments[14] of Langmuir waves. However, O'neil's treatment becomes invalid for a long wave time evolution. It is now found[10] that nonlinear plasma waves undergo a few amplitude oscillations and eventually approach a Bernstein-Greene-Kruskal (BGK) steady state[4] instead of decaying away. This conclusion could also be drawn from the recent Landau damping experiments[7] and plasma simulations for a long wave time evolution[5, 6] of Langmuir waves.

O'Neil's theory[2] provided an exact solution of the Vlasov equation for the resonant electrons using Jacobi elliptic functions, and the damping coefficient as a function

of time is given by

$$\gamma(t) = \gamma_L \sum_{n=0}^{\infty} \frac{64}{\pi} \int_0^1 d\kappa \{ \frac{2n\pi^2 \sin(\frac{\pi n t}{\kappa F \tau})}{\kappa^5 F^2 (1+q^{2n})(1+q^{-2n})} + \frac{(2n+1)\pi^2 \kappa \sin(\frac{(2n+1)\pi t}{2F\tau})}{F^2(1+q^{2n+1})(1+q^{-2n-1})} \}, \tag{1.26}$$

$$\int_0^t \gamma(t')d(t') = \gamma_L \tau \sum_{n=0}^{\infty} \frac{64}{\pi} \int_0^1 d\kappa \{ \frac{2\pi(1-\cos(\frac{\pi n t}{\kappa F \tau}))}{\kappa^4 F (1+q^{2n})(1+q^{-2n})} + \frac{2\pi\kappa(1-\cos(\frac{(2n+1)\pi t}{2F\tau}))}{F(1+q^{2n+1})(1+q^{-2n-1})} \}. \tag{1.27}$$

Where $\kappa^2 = 2eE/(kW + eE)$ with W being the conserved energy, $F = F(\kappa, \frac{1}{2}\pi)$, with κ taking the sign of $\frac{1}{2}\pi$, is the elliptic integral of the first kind , and $q = \exp(\pi F'/F)$.

By taking into account the κ dependence of F and κF, it can be shown that the integrals over $\sin[(2n+1)\pi t/2F\tau]$, $\sin[\pi n t/\kappa F\tau]$, $\cos[(2n+1)\pi t/2F\tau]$, $\cos[\pi n t/\kappa F\tau]$, phase mix to zero as t/τ approaches infinity. Thus, Eqs. (1.26) and (1.27) become

$$\gamma(t = \infty) = 0, \tag{1.28}$$

$$\int_0^{\infty} \gamma(t)dt = \gamma_L \tau \sum_{n=1}^{\infty} \frac{64}{\pi} \int_0^1 d\kappa \{ \frac{2\pi}{\kappa^4 F (1+q^{2n})(1+q^{-2n})} + \frac{2\pi\kappa}{F(1+q^{2n-1})(1+q^{-2n+1})} \}. \tag{1.29}$$

After the series in Eq. 1.29 are summed

$$\int_0^{\infty} \gamma(t)dt = \gamma_L \tau \frac{64}{\pi} \int_0^1 d\kappa \{ \frac{1}{\kappa^4} [\frac{E}{\pi} - \frac{\pi}{4F}] + \frac{\kappa}{\pi} [E + (\kappa^2 - 1)F] \} = O(\gamma_L \tau). \tag{1.30}$$

O'Neil's treatment, as presented above, is valid only if the nonlinear effects prevent the amplitude from decaying by a significant amount. From Eq. 1.30, the above condition is satisfied when $\gamma_L \tau \ll 1$. Meanwhile, Eq. 1.29 shows that as t/τ approaches infinity, $\gamma(t)$ phase mixes to zero. The wave evolves into a BGK[4] equilibrium, in which the wave amplitude oscillates with a finite constant value.

Note that $\gamma(t)$ is the damping rate, thus the value of $\gamma_L \tau$ is also the critical value of the linear Landau damping and the nonlinear Landau damping. In general,

$\gamma_L \tau \ll 1$, we consider the damping process mainly as nonlinear Landau damping, otherwise, the process is treated as linear Landau damping.

The physical interpretation of the nonlinear Landau damping process lies basically on the particles trapping mechanism. As the Langmuir wave propagates in the plasma, some electrons can be trapped in the potential well of the wave's electric field. As the trapped electrons bounce back and forth in the potential well with a period of order τ, the trapped electrons keep exchanging energy with the the wave. The phase mixing of the trapped electrons causes the wave amplitude to reach an asymptotic constant, forming a stable equilibrium with an undamped nonlinear plasma wave, i.e., the BGK equilibrium. Fig 1.2 shows the physical picture of the electron distribution function f in the phase space (x, v). There is a vortex structure in the phase space of the distribution, where is dominated by the trapped electrons with cyclic trajectory.

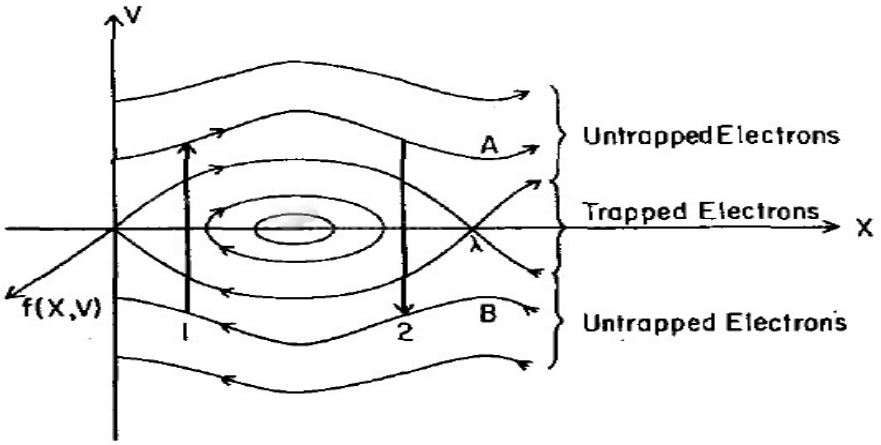

Figure 1.2: Phase trajectories of the resonant electrons

Recently, Giovanni Manfredi[5] presented the complete behavior of nonlinear Landau damping of Langmuir waves in a particle simulation. The simulation work showed explicitly the characteristics of the nonlinear Landau damping in the electron plasma wave. Fig 1.3 shows the evolution of the amplitude of the electric field in Manfredi's 3 runs. It is seen from the figure, as discussed in O'Neil's theory, the wave

amplitude decreases within the first few oscillations, but eventually settles down to a steady oscillation with an undamped constant amplitude. According to O'Neil's theory, some electrons can be trapped and there will be a vortex structure in the phase space of the distribution function at the resonance region, as shown by Manfredi (Fig. 1.4).

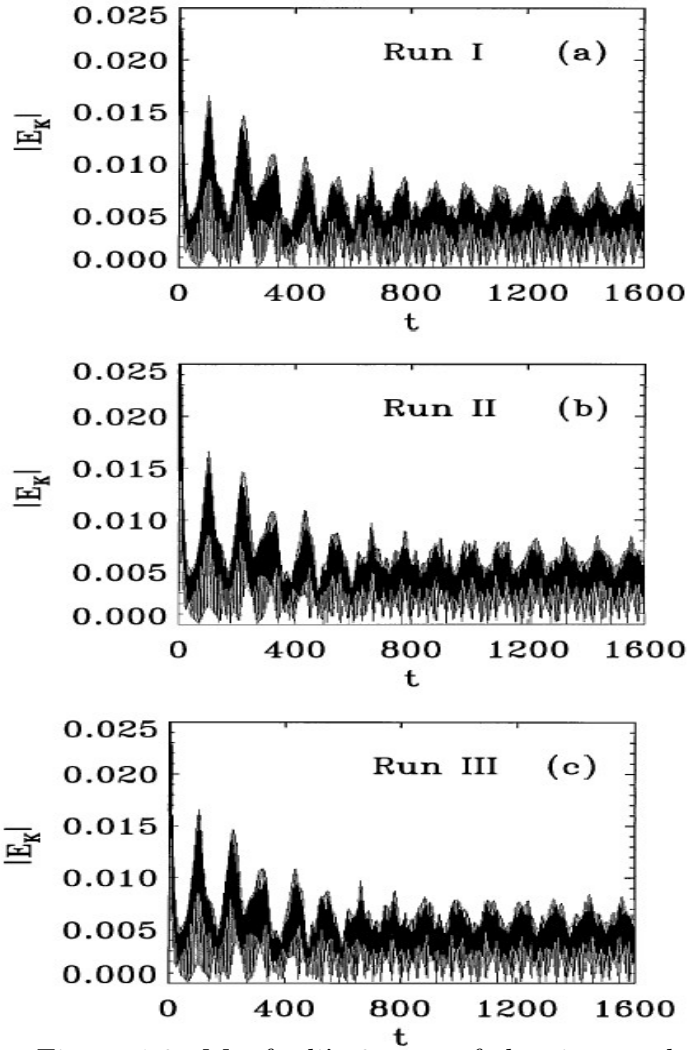

Figure 1.3: Manfredi's 3 runs of the time evolution of the amplitude of the electric field

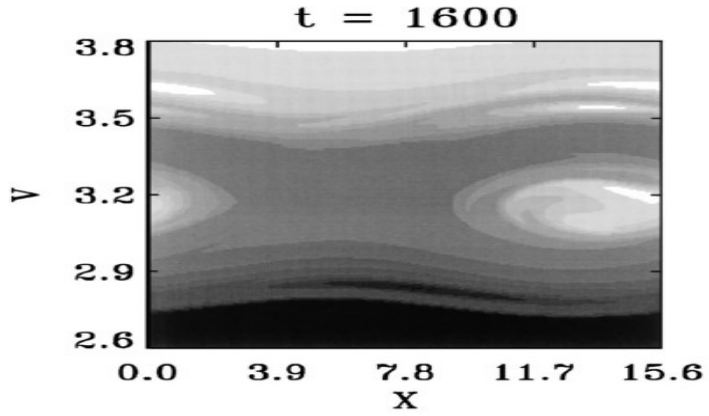

Figure 1.4: Manfredi's shaded plot of the distribution function in the resonant region

1.3 Landau damping of electrostatic LHWs

In this section the theory of Landau damping in an electrostatic LHW in the cold plasma is introduced. The coefficient of the electron Landau damping (ELD) of the electrostatic LHWs will be derived. Different mechanisms between the electron Landau damping and the ion Landau damping of electrostatic LHWs will be discussed as well as the ion Landau damping rate.

1.3.1 Coefficient of the linear electron Landau damping

In Eq. 1.15, consider that the wave vector $\mathbf{k}$ is fixed, if $D_0(\mathbf{x}, \mathbf{k}, \omega)$ has an imaginary part due to some damping mechanism, then ω must become complex

$$\omega = \omega_r + i\gamma. \tag{1.31}$$

If the damping is weak, then $\gamma/\omega_r \ll 1$ and the dispersion relation may be written as

$$D_0(\mathbf{x}, \mathbf{k}, \omega) \simeq D_{0r}(\mathbf{x}, \mathbf{k}, \omega_r + i\gamma) + iD_{0i}(\mathbf{x}, \mathbf{k}, \omega_r) = 0. \tag{1.32}$$

Taking real and imaginary parts of Eq. 1.32, one can obtain the general formula to calculate the coefficient of the linear ELD of LHWs

$$\begin{aligned} D_{0r}(\mathbf{x},\mathbf{k},\omega_r) &\simeq 0 \\ \gamma &\simeq \frac{-D_{0i}(\mathbf{x},\mathbf{k},\omega_r)}{\partial D_{0r}/\partial\omega_r}. \end{aligned} \tag{1.33}$$

In the presence of the linear electron Landau damping, the dispersion relation of the LHWs can be written as[16]

$$D_0 = \frac{k_\perp^2}{k^2}\epsilon_\perp + \frac{k_\parallel^2}{k^2}\epsilon_\parallel + \frac{i\sqrt{\pi}}{k^2\lambda_D^2}\frac{\omega}{\sqrt{2}k_\parallel V_{te}}\exp(-\frac{\omega^2}{2k_\parallel^2 V_{te}^2}) = 0, \tag{1.34}$$

where $\lambda_D = V_{te}/\omega_{pe}$ is the electron Debye length. It can be seen from Eqs. 1.15 and 1.34 that the linear ELD only contributes to the imaginary part of the dispersion relation

$$D_{0i} = \frac{\sqrt{\pi}}{k^2\lambda_D^2}\frac{\omega}{\sqrt{2}k_\parallel V_{te}}\exp(-\frac{\omega^2}{2k_\parallel^2 V_{te}^2}). \tag{1.35}$$

Let us rewrite Eq. 1.15 as

$$D_{0r} = \frac{k_\perp^2}{k^2}\epsilon_\perp + \frac{k_\parallel^2}{k^2}\epsilon_\parallel. \tag{1.36}$$

Plug the D_{0r} and D_{0i} into Eq. 1.33. The expression of the coefficient of the electrostatic LHWs' electron Landau damping is found to be

$$\begin{aligned} \gamma/\omega_r &\simeq \frac{-D_{0i}}{\omega_r\partial D_{0r}/\partial\omega_r} \\ &= \frac{-\frac{\sqrt{\pi}}{k^2\lambda_D^2}\frac{\omega_r}{\sqrt{2}k_\parallel V_{te}}\exp(-\frac{\omega_r^2}{2k_\parallel^2 V_{te}^2})}{2[\frac{k_\perp^2}{k^2}\frac{\omega_{pi}^2}{\omega_r^2} + \frac{k_\parallel^2}{k^2}\frac{\omega_{pe}^2}{\omega_r^2}]}. \end{aligned} \tag{1.37}$$

Since lots of different approximations are made in the derivation of the damping rate, there are few other expressions that were adopted by others[21]. From Eq. 1.33,

the following expression can be acquired

$$\gamma \simeq \frac{-D_{0i}(\mathbf{x},\mathbf{k},\omega_r)}{(\partial D_{0r}/\partial k)(\partial k/\omega_r)} = \frac{-D_{0i}(\mathbf{x},\mathbf{k},\omega_r)}{\partial D_{0r}/\partial k}(\partial\omega_r/\partial k), \tag{1.38}$$

where, ω_r takes the form of Eq. 1.16. From this respect, one can obtain the following expression of the damping rate

$$\gamma = \frac{\sqrt{\pi}}{2\sqrt{2}}\frac{\omega_{LH}^2}{k^2c_s^2}\omega_r^2\frac{1}{k_\parallel V_{te}}\exp(-\frac{\omega^2}{2k_\parallel^2V_{te}^2}), \tag{1.39}$$

with $c_s = \sqrt{\kappa T_e/m_i}$. Although the two expressions of the ELD rate of electrostatic LHW (Eqs. 1.37 and 1.39) are different, the numerical results from them are pretty close to each other.

1.3.2 Physical mechanisms of the Landau damping of LHWs

Unlike most other wave modes, lower hybrid waves (LHWs) that interact resonantly with electrons can also undergo resonant interactions with ions. This allows LHWs to mediate the transfer of energy between the two species and possibly lead to plasma heating or particle acceleration, making them of considerable interest in many different laboratory[26, 30, 31] and space[32, 33, 34] plasma environments. As $\Omega_i \ll \omega_{LH} \ll \Omega_e$, when considering interactions with LHWs, the electrons must be treated as being magnetized, their gyro-motions cannot be neglected, and they interact resonantly with the waves when the condition

$$\omega = k_\parallel v_{e\parallel} \tag{1.40}$$

is satisfied. However, the ions are often treated as unmagnetized, so their gyro-motions may be neglected and they interact resonantly with the waves when the

condition

$$\omega = \mathbf{k} \cdot \mathbf{v_i} \tag{1.41}$$

is satisfied. Here $\mathbf{v_e}$ and $\mathbf{v_i}$ are the velocities of an electron and ion, respectively.

Since $k_\parallel \ll k_\perp$ and $v_e \gg v_i$ for typical particles if the ion and electron temperatures are similar, LHWs with the same $\mathbf{k}$ can satisfy both Eqs. 1.40 and 1.41 provided that $\mathbf{v_i}$ has a significant component perpendicular to $\mathbf{B}$. Hence, LHWs can interact resonantly with both ions and electrons and transfer energy between the parallel motions of electrons and the perpendicular motions of ions. Thus, if the ion effects are included, the linear Landau damping rate of LHWs can be obtained as

$$\frac{\gamma}{\omega_r} = \frac{\sqrt{\pi}}{2}\frac{\omega_{LH}^2}{k^2 c_s^2}\{\frac{\omega_r}{\sqrt{2}k_\parallel V_{te}}\exp(-\frac{\omega_r^2}{2k_\parallel^2 V_{te}^2}) + \frac{T_e}{T_i}\frac{\omega_r}{\sqrt{2}kV_{ti}}\exp(-\frac{\omega_r^2}{2k^2 V_{ti}^2})\}, \tag{1.42}$$

where $V_{ti} = \sqrt{\kappa T_i/m_i}$ is the ion thermal speed.

1.4 Parametric instability

In this section, general theories of PI of LHWs are introduced[63, 21]. The dispersion relation equation near lower hybrid wave frequency is reviewed in detailed algebras. By including the effects of ion nonlinearity, the various channels of parametric decay of LHWs are discussed.

1.4.1 The PI dispersion relation near lower hybrid frequency

Consider the system with a static magnetic field in z direction and a lower hybrid wave (pump wave) with frequency and wave number $(\omega_0, \mathbf{k_0})$ to propagate in x-z plane. A low frequency wave mode $(\omega, \mathbf{k})$ and two sidebands $(\omega \pm \omega_0, \mathbf{k} \pm \mathbf{k_0})$ are considered to be the decay waves.

Equations of ions response

For the ions, with the presence of the electrostatic potentials of the pump and decay waves, the distribution can be decomposed to be a unperturbed part (f_{0i}^0), a response part at the pump (f_{0i}), responses at sidebands ($f_{1,2i}$) and a response at low frequency (f_i).

$$F_i = f_{0i}^0 + f_{0i} + f_{1,2i} + f_i, \tag{1.43}$$

where f_{0i}^0 is Maxwellian distributed. For the high frequency response, ions can be assumed to be unmagnetized, and thus one can obtain

$$\begin{aligned}
f_{0i} &= \frac{e\phi_0}{k_B T_i}\frac{\mathbf{k_0}\cdot\mathbf{v}}{\omega_0}(1+\frac{\mathbf{k_0}\cdot\mathbf{v}}{\omega_0})f_{0i}^0\exp[-i(\omega_0 t-\mathbf{k_0}\cdot\mathbf{x})], && (1.44)\\
f_{1i} &= f_{1i}^l + f_{1i}^{nl}, && (1.45)\\
f_{1i}^l &= \frac{e\phi_1}{k_B T_i}\frac{\mathbf{k_1}\cdot\mathbf{v}}{\omega_1}(1+\frac{\mathbf{k_1}\cdot\mathbf{v}}{\omega_1})f_{0i}^0\exp[-i(\omega_1 t-\mathbf{k_1}\cdot\mathbf{x})], && (1.46)\\
f_{1i}^{nl} &= \frac{e}{2m_i\omega_1}(1+\frac{\mathbf{k_1}\cdot\mathbf{v}}{\omega_1})[\mathbf{k_0}\cdot\frac{\partial f_i}{\partial\mathbf{v}}\Phi_0^* - \mathbf{k}\cdot\frac{\partial f_{0i}^*}{\partial\mathbf{v}}\Phi]. && (1.47)
\end{aligned}$$

Here $\mathbf{k_1}=\mathbf{k}-\mathbf{k_0}$, $\omega_1=\omega-\omega_0$, $k_1v_i<\omega_1$, $k_0v_i<\omega_0$. $\Phi_0=\phi_0\exp[-i(\omega_0 t-\mathbf{k_0}\cdot\mathbf{x})]$ is the electrostatic potential of the pump wave. In the same wave, Φ and $\Phi_{1,2}$ denote the electrostatic potentials of the decay waves. From the distributions, one can obtain the ion density fluctuations

$$\begin{aligned}
n_{1i} &= n_{1i}^l + n_{1i}^{nl}, && (1.48)\\
n_{1i}^l &= \frac{ek_1^2\Phi_1}{m_i\omega_1^2}n_0^0, && (1.49)\\
n_{1i}^{nl} &= \frac{e}{2m_i\omega_1}[-\frac{\mathbf{k_0}\cdot\mathbf{k_1}}{\omega_1}\Phi_0^* n_i + \frac{\mathbf{k}\cdot\mathbf{k_1}}{\omega_1}\Phi n_{0i}^*], && (1.50)
\end{aligned}$$

where n_i is the response at the low frequency and n_{0i} at the frequency of the pump,

$$n_{0i} = ek_0^2\Phi_0 n_0^0/m_i\omega_0^2. \tag{1.51}$$

The evolution of F_i is governed by the Vlasov equation in terms of guiding-center coordinates $\mathbf{X_g}$, magnetic momentum μ, polar angle θ of the perpendicular velocity, and the parallel momentum $p_\parallel$.

$$\frac{\partial F_i}{\partial t} + \dot{\mu}\frac{\partial F_i}{\partial \mu} + \dot{\theta}\frac{\partial F_i}{\partial \theta} - e\frac{\partial}{\partial z}\Phi\frac{\partial F_i}{\partial p_\parallel} + \dot{\mathbf{X}}_\mathbf{g}\cdot\frac{\partial F_i}{\partial \mathbf{X_g}} = 0, \tag{1.52}$$

where $\mathbf{X_g} = (x+\rho\sin\theta)\mathbf{e_x} + (y-\rho\cos\theta)\mathbf{e_y} + z\mathbf{e_z} = (x_g, y_g, z_g)$, $\rho = v_\perp/\Omega_i$, $\Omega_i = eB/m_ic$ is the ion gyro-frequency, $\mu = m_iv_\perp^2/2\Omega_i$, and the over-dots denote the time derivatives. All the over-dots components can be easily derived by using the equations of motions

$$\begin{aligned}
\dot{\mu} &= -\frac{e}{\Omega_i}\nabla_\perp\Phi'\cdot\mathbf{v}_\perp = \frac{\partial H}{\partial\theta}, & (1.53)\\
\dot{\theta} &= -(\Omega_i + \frac{\partial}{\partial\mu}e\Phi') = -\frac{\partial H}{\partial\mu}, & (1.54)\\
\dot{\mathbf{X}}_\mathbf{g} &= -\frac{e}{m_i\Omega_i}\frac{\partial\Phi'}{\partial y_g}\mathbf{e_x} + \frac{e}{m_i\Omega_i}\frac{\partial\Phi'}{\partial x_g}\mathbf{e_y} + \frac{p_\parallel}{m_i}\mathbf{e_z}. & (1.55)
\end{aligned}$$

The Hamiltonian $H = \mu_i\Omega_i + e\Phi' + p_\parallel^2/2m_i$ and $\Phi' = \Phi_0 + \Phi_{1,2} + \Phi$ is the total electrostatic potential of the system. As we can see, (μ,θ), (x_g, y_g), and (z, p_z) are canonical variables. Eq. 1.52 follows directly from the continuity equation of ion density in these six dimensional space.

To linearize Eq. 1.52, one can obtain the low frequency response

$$f_i^l = -\exp[-i(\omega t - \mathbf{k}\cdot\mathbf{X_g})]\sum_i\frac{e\phi\exp[-il(\theta-\delta)]J_l(k_\perp\rho)}{\omega - k_\parallel v_\parallel - l\Omega_i}(l\frac{\partial f_{0i}^0}{\partial\mu} + k_\parallel\frac{\partial f_{0i}^0}{\partial p_\parallel}). \tag{1.56}$$

Here, the identity $\exp[-i(\omega t - \mathbf{k}\cdot\mathbf{x})] \equiv \exp[-i(\omega t - \mathbf{k}\cdot\mathbf{X_g})]\sum_i\exp[-il(\theta-\delta)J_l(k_\perp\rho)]$ is used. δ is the angle between $\mathbf{k}_\perp$ and $\mathbf{k_{0\perp}}$ (similarly δ_1 is the angle between $\mathbf{k_{1\perp}}$ and $\mathbf{k_{0\perp}}$), and $v_\parallel = p_\parallel/m_i$ is the parallel velocity of ion. For the nonlinear part of the

distribution associated with the low frequency response, one can obtain

$$-i(\omega - k_{\parallel}v_{\parallel})f_i^{nl} - \Omega_i(\frac{\partial f_i^{nl}}{\partial \theta}) = \psi_1 + \psi_2, \tag{1.57}$$

where ψ_1 and ψ_2 are from the contributions of lower sideband and upper sideband, respectively.

$$\begin{aligned}
\psi_1 &= \frac{1}{2}iek_{0\perp}\Phi_0\rho\cos\theta\frac{\partial f_{1i}}{\partial \mu} + \frac{1}{2}iek_{1\perp}\Phi_1\rho\cos(\theta-\delta_1)\frac{\partial f_{0i}}{\partial \mu} \\
&- \frac{1}{2}\frac{iek_{0\perp}\sin\theta}{m_i v_\perp}\Phi_0\frac{\partial f_{1i}}{\partial \theta} - \frac{1}{2}\frac{iek_{1\perp}\sin(\theta-\delta_1)}{m_i v_\perp}\Phi_1\frac{\partial f_{0i}}{\partial \theta} \\
&+ \frac{1}{2}ik_{0\parallel}e\Phi_0\frac{\partial f_{1i}}{\partial p_\parallel} + \frac{1}{2}ik_{1\parallel}e\Phi_1\frac{\partial f_{0i}}{\partial p_\parallel} \\
&+ \frac{eik_{1y}}{2m_i\Omega_i}\Phi_1(ik_{0\perp}f_{0i}) - \frac{iek_{0\perp}}{2m_i\Omega_i}\Phi_0(ik_{1y}f_{1i}).
\end{aligned} \tag{1.58}$$

ψ_2 can be obtained by replacing Φ_0, f_{0i}, ω_0, and k_0 by Φ_0^*, f_{0i}^*, $-\omega_0$ and $-\mathbf{k_0}$, respectively. Taking the approximation $k_{1\parallel} \ll k_1$ and $\mathbf{k_1}\cdot\mathbf{v} < \omega_1$, Eq. 1.58 can be simplified

$$\begin{aligned}
\psi_1 &= \frac{ie^2\phi_0\phi_1 f_0^0}{2k_B T_i m_i}[-\frac{\omega}{\omega_0^2}\mathbf{k_0}\cdot\mathbf{k_1} + \frac{\mathbf{k_0}\cdot\mathbf{k_1}}{\omega_0^2}(\mathbf{k}\cdot\mathbf{v} - \frac{2\omega}{\omega_0}\mathbf{k_0}\cdot\mathbf{v}) \\
&- \frac{m_i}{k_B T_i}\mathbf{k_0}\cdot\mathbf{v}\mathbf{k_1}\cdot\mathbf{v}(-\frac{\omega}{\omega_0^2} + \frac{\mathbf{k}\cdot\mathbf{v}}{\omega_0^2} - \frac{2\omega}{\omega_0^3}\mathbf{k_0}\cdot\mathbf{v})]\exp[-i(\omega t - \mathbf{k}\cdot\mathbf{x})].
\end{aligned} \tag{1.59}$$

By solving Eq. 1.57, the following expression for the low frequency component of the ion density can be obtain by reusing the identity.

$$n_i = n_i^l + n_i^{nl}, \tag{1.60}$$

$$\begin{aligned}
n_i^l &= -\frac{k^2}{4\pi e}\chi_i\phi\exp[-i\omega t - \mathbf{k}\cdot\mathbf{x}] \\
&= -\frac{\omega_{pi}^2\phi}{2\pi e v_i^2}[1 + \sum_l \frac{\omega}{k_\parallel v_i}Z(\frac{\omega - l\Omega_i}{k_\parallel v_i})I_l(b_i)\exp(-b_i)]\exp[-i(\omega t - \mathbf{k}\cdot\mathbf{x})],
\end{aligned} \tag{1.61}$$

and

$$n_i^{nl} = (\beta_1\phi_0\phi_1 + \beta_2\phi_0^*\phi_2)\exp[-i(\omega t - \mathbf{k}\cdot\mathbf{x})], \tag{1.62}$$

where $b_i = k_\perp^2\rho_i^2/2$, $I_l(b_i)$ is the Bessel function of the second kind, Z is the plasma dispersion function. β_1 can be obtained to be the following expression

$$\begin{aligned}
\beta_1 &= \frac{n_0^0 e^2 k_{0\perp}k_{1\perp}}{2k_B T_i m_i\omega_0^2}\frac{\omega}{k_\parallel v_i}\sum_i Z(\frac{\omega - l\Omega_i}{k_\parallel v_i})((-1 + \frac{2l\Omega_i}{\omega} - \frac{4k_{0\perp}\omega}{k_\perp\omega_0}\cos\delta)\cos\delta_1 I_1\exp(-b_i) \\
&+ i\frac{2k_{0\perp}k_\perp v_i\rho_i}{\omega_0}\sin\delta\cos\delta_1\frac{d}{db_i}[I_l\exp(-b_i)] + \frac{2k_{0\perp}l\Omega_i}{k_\perp\omega_0}\frac{d}{db_i}[b_i I_l\exp(-b_i)][\cos(\delta-\delta_1) \\
&+ \frac{1}{2}\cos(\delta+\delta_1) - \frac{1}{2}\cos(3\delta-\delta_1)] + (1 - \frac{l\Omega_i}{\omega})\cos\delta_1\frac{d}{db_i}[I_l\exp(-b_i)] \\
&- i\frac{k_{0\perp}k_\perp v_i\rho_i}{\omega_0}\frac{d^2}{db_i^2}[b_i I_l\exp(-b_i)][\sin(\delta-\delta_1) + \frac{1}{2}\sin(\delta+\delta_1) - \frac{1}{2}\sin(3\delta-\delta_1)] \\
&+ \frac{1}{2}\{-\frac{2\Omega_i}{\omega}i\sin(2\delta-\delta_1) + (1-\frac{l\Omega_i}{\omega})\cos(2\delta-\delta_1) + \frac{2k_{0\perp}\Omega_i}{k_\perp\omega_0}[l\cos(3\delta-\delta_1) + 2i\sin(3\delta-\delta_1)]\} \\
&\times \{\frac{4l^2 I_l\exp(-b_i)}{k_\perp^2\rho_i^2} - 2I_l\exp(-b_i) - 2(1+b_i)\frac{d}{db_i}[I_l\exp(-b_i)]\} \\
&+ \frac{1}{2}\{-\frac{2\Omega_i}{\omega}\cos(2\delta-\delta_1) + (1-\frac{l\Omega_i}{\omega})i\sin(2\delta-\delta_1) + \frac{2k_{0\perp}\Omega_i}{k_\perp\omega_0}[2\cos(3\delta-\delta_1) + il\sin(3\delta-\delta_1)]\} \\
&\times \{-2l\frac{d}{db_i}[I_l\exp(-b_i)] + 4l\frac{I_l\exp(-b_i)}{k_\perp^2\rho_i^2}\}).
\end{aligned} \tag{1.63}$$

By replacing ω_0, k_0 by $-\omega_0$, $-k_0$, and the subscript 1 by 2, one can obtain β_2.

Response of electrons

Since the electron Larmor radius is much shorter than the wave lengths involved in the parametric process, drift kinetic theory can be used to describe the response of electrons. Referring to Tripathi *et al.*[63], the nonlinear electron density fluctuations at the decay wave frequencies can be written in the following expressions.

$$\begin{aligned}
n_e^{nl} &= (\alpha_1\phi_0\phi_1 + \alpha_2\phi_0^*\phi_2)\exp[-i(\omega t - \mathbf{k}\cdot\mathbf{x})], \\
n_{1e}^{nl} &= \alpha_3\phi_0^*\phi\exp -i[(\omega-\omega_0)t - (\mathbf{k}-\mathbf{k_0})\cdot\mathbf{x}], \\
n_{2e}^{nl} &= \alpha_4\phi_0\phi\exp -i[(\omega+\omega_0)t - (\mathbf{k}+\mathbf{k_0})\cdot\mathbf{x}],
\end{aligned} \tag{1.64}$$

where

$$\alpha_1 = \alpha_{1\mathbf{E}\times\mathbf{B}} + \Delta, \tag{1.65}$$

$$\alpha_{1\mathbf{E}\times\mathbf{B}} = -\frac{ie^2 n_0^0}{\Omega_e m_e^2 v_e^3} \frac{k_{0\perp} k_{1\perp} \sin\delta_1}{\omega k_{0\parallel} - \omega_0 k_\parallel} (\omega Z - \omega_0 Z_0 - \omega_1 Z_1), \tag{1.66}$$

$$\begin{aligned} \Delta &= \frac{e^2 n_0^0}{m_e^2 v_e^2 \Omega_e^2} [k_\perp^2 - \mathbf{k_0}_\perp \cdot \mathbf{k_1}_\perp \xi_1 Z_1 + \mathbf{k}_\perp \cdot \mathbf{k_1}_\perp \xi_0 Z_0] \\ &+ \frac{e^2 k_{0\parallel} k_{1\parallel} k_\parallel n_0^0}{m_e^2 v_e^3 (\omega k_{0\parallel} - \omega_0 k_\parallel)^2} (\omega Z - \omega_0 Z_0 - \omega_1 Z_1). \end{aligned} \tag{1.67}$$

Here $\xi = \omega/k_\parallel v_e$, $\xi_{0,1} = \omega_{0,1}/k_{0,1\parallel} v_e$, $v_e = \sqrt{2k_B T_e/m_e}$ the electron thermal speed, $\Omega_e = eB/m_e c$ the electron gyro frequency, $Z = Z(\xi)$ and $Z_{0,1} = Z(\xi_{0,1})$. α_2 can be obtained by replacing ω_0, $\mathbf{k_0}$ by $-\omega_0$, $-\mathbf{k_0}$ and the subscript 1 by 2, and

$$\alpha_3 = \frac{\chi_e - \epsilon(\omega)}{\chi_e(\omega)} \alpha_1(\Omega_e \to -\Omega_e), \tag{1.68}$$

$$\alpha_4 = \frac{\chi_e - \epsilon(\omega)}{\chi_e(\omega)} \alpha_2(\Omega_e \to -\Omega_e). \tag{1.69}$$

Δ denotes the contributions from the parallel motions and polarization drift, and $\alpha_{1\mathbf{E}\times\mathbf{B}}$ denotes the $\mathbf{E}\times\mathbf{B}$ nonlinearity arising through the parallel ponderomotive force $-m_e \mathbf{v}_{\mathbf{E}\times\mathbf{B}} \cdot \nabla v_\parallel$, $\alpha_{1\mathbf{E}\times\mathbf{B}} \sim \sqrt{m_i/m_e}\Delta$.

Now, one can obtain the nonlinear dispersion relation by combining Eqs. 1.62, 1.64 and the Poisson's equation

$$1 = \frac{\mu_1}{\epsilon\epsilon_1} + \frac{\mu_2}{\epsilon\epsilon_2}, \tag{1.70}$$

where

$$\mu_1 = \frac{\chi_e(\omega) - \epsilon(\omega)}{\chi_e(\omega)} \frac{\omega_{pi}^2}{\omega_0^2} \frac{\omega_{pi}^2}{4k^2 c_s^2} (1 + \frac{\omega}{k_\parallel v_e} Z)^2 \sin^2\delta_1 \frac{U^2}{c_s^2}, \tag{1.71}$$

for $\omega \leq k_\parallel v_e$, and

$$\mu_1 = \frac{\chi_e(\omega) - \epsilon(\omega)}{\chi_e(\omega)} \frac{\omega_{pi}^2}{\omega_0^2} \frac{\omega_{pi}^2}{k^2} \frac{(m_i/m_e)^2}{4(k_\parallel - \frac{\omega}{\omega_0} k_{0\parallel})^2} (\frac{k_\parallel^3}{\omega^2} - \frac{k_{0\parallel}^3}{\omega_0^2} - \frac{k_{1\parallel}^3}{\omega_1^2}) U^2, \tag{1.72}$$

for $\omega \gg k_\parallel v_e$. $\mu_2 = \mu_1(\delta_1 - \delta_2)$, $c_s = \sqrt{k_B T_e/m_i}$ the ion sound speed, and $U = ek_0\phi_0/m_e\Omega_e$ is the $\mathbf{E} \times \mathbf{B}$ drift velocity of electrons. ϵ and $\epsilon_{1,2}$ are the linear dielectric functions at ω and $\omega_{1,2}$, respectively.

1.4.2 Decay channels

We have reviewed the dispersion relation in the previous introduction, here the various decay channels of lower hybrid wave through parametric instability will be summarized. The pump LHW with $(\omega_0, \mathbf{k_0})$ decays into a low frequency wave mode $(\omega, \mathbf{k})$ and two high frequency sidebands $(\omega \pm \omega_0, \mathbf{k} \pm \mathbf{k_0})$.The sidebands can be lower hybrid wave modes or ion Bernstein wave mode ($\omega \sim n\Omega_i$). The various decay channels are classified into three regions according to the magnitude of $k_\parallel v_e/\omega$.

Case A: $k_\parallel v_e/\omega \leq 0.3$

In this case, the possible channels can be

Channel 1: pump wave decays into two lower hybrid waves. $\omega_0 > 2\omega_{LH}$.

Channel 2: pump wave decays into ion Bernstein and lower hybrid waves. $\omega \leq \Omega_i$ and $k_\perp \rho_i \ll 1$, or $\omega \geq 3\Omega_i$ with arbitrary $k_\perp \rho_i$.

Channel 3: pump LHW decays into ion Bernstein reactive quasi-mode and lower hybrid wave mode (four-wave decay).

Channel 4: the decay follows modulational instability.

The growth rates for all the channels in case A will be introduced in the following discussions.

Channel 1. *Decay into two lower hybrid waves.* In this channel, the requirement $\omega_0 > 2\omega_{LH}$ needs to be satisfied since both of the decay waves are lower hybrid waves, which have frequencies larger than ω_{LH}. The growth rate, dominated by the $\mathbf{E} \times \mathbf{B}$ electron nonlinearity, is given by

$$\gamma_0^2 = [\frac{\omega_{LH}^2}{4\omega_0} \frac{\omega^{1/2}(\omega_0 - \omega)^{1/2} m_i/m_e}{(k_\parallel - \omega k_{0\parallel}/\omega_0)k} (\frac{k_\parallel^3}{\omega^2} - \frac{k_{0\parallel}^3}{\omega_0^2} - \frac{k_{1\parallel}^3}{\omega_1^2})]^2 U^2 \sin^2 \delta_1. \tag{1.73}$$

Note that γ_0 is the growth rate without taking the damping effects into account.

Channel 2. *Ion Bernstein and lower hybrid waves.* There are two cases needed to be considered in this channel.

(1) $k_\perp \rho_i < 1$. For $\omega \leq \Omega_i$, the linear dielectric function simplifies to

$$\omega^2 = \Omega_i^2 \frac{k_\parallel^2 m_i}{k^2 m_e} (1 + \frac{k_\parallel^2 m_i}{k^2 m_e})^{-1}, \tag{1.74}$$

and thus one can obtain the growth rate

$$\gamma_0 \simeq (\omega_0 \Omega_i)^{1/2} (1 - \frac{\omega_{LH}^2}{\omega_0^2})^{1/4} (\frac{T_e}{2T_i})^{1/2} k\rho_i \frac{\omega_{LH}}{\omega_0} \frac{U}{4c_s} \sin \delta_1. \tag{1.75}$$

(2) $k_\perp \rho_i \gg 1$ ($\omega \simeq n\Omega_i$, $n \geq 3$). In this case, the dielectric function is

$$\epsilon \simeq 1 + \frac{\omega_{pe}^2}{\Omega_e^2} - \frac{\omega_{pi}^2}{\omega^2} \frac{k_\parallel^2 m_i}{k^2 m_e} + \frac{2\omega_{pi}^2}{k^2 v_i^2} (1 - \frac{\omega I_n(b_i) \exp(-b_i)}{\omega - n\Omega_i}). \tag{1.76}$$

The growth rate turns out to be in the following expression

$$\begin{aligned} \gamma_0 &= \frac{\omega_{LH}(k_\perp \rho_i)^{1/2}}{2\pi^{1/4}\omega_0} (\frac{T_e}{2T_i})^{1/2} \frac{U}{c_s} [\frac{(2\omega - \omega_0)\Omega_i^3}{\omega^2(\omega_0 - \omega)^2} (\frac{\omega_1^2}{\omega_{LH}^2} - 1) \sin \delta_1]^{1/2} \\ &\times [k_\perp^2 \rho_i^2 \omega_0^2 \frac{(2\omega - \omega_0)\Omega_i}{\omega^2(\omega_0 - \omega)^2} (\frac{\omega_1^2}{\omega_{LH}^2} - 1) \sin \delta_1 + i \cos \delta_1]^{1/2}. \end{aligned} \tag{1.77}$$

Note that $i\cos\delta_1$ term is due to the ion nonlinearity. This growth rate is comparable to that for the decay into ion cyclotron waves. The condition for Eq. 1.77 to be valid is $\gamma_0 < \omega - n\Omega_i$. The mode will become a reactive quasi-mode if $\gamma_0 > \omega - n\Omega_i$, however, as the growth rate and frequency mismatch increases the ion contribution is drastically reduced.

Channel 3. *Ion Bernstein Reactive quasi-mode and lower hybrid waves (four-wave decay).* It becomes a reactive quasi-mode if the low frequency mode has $\omega \gg k_\parallel v_e$ and $k_\perp \rho_i \ll 1$ for higher values of U/c_s, or if $\omega \ll \Omega_i$ can no longer satisfy $\omega \gg \gamma$, and the two sidebands are equally important. In this case, one have

$$\omega = \omega_r + i\gamma, \tag{1.78}$$

$$\omega_r = \gamma^2 + \Delta^2/2, \tag{1.79}$$

$$\gamma^2 = -\Delta^2/4 + 1/2(A\Delta)^{1/2}. \tag{1.80}$$

Here $\Delta = \omega_0 - \omega_{LH}[1 + (k_\parallel^2/k^2)(m_i/m_e)]^{1/2}$, $k > k_0$, and

$$A = \frac{\omega_{LH}^2}{4\omega_0^2}(\omega_0^2 - \omega_{LH}^2)\frac{k^2 c_s^2}{\omega_0}\frac{U^2}{c_s^2}. \tag{1.81}$$

Note that this growth rate is less than that for the oscillating two-stream instability.

Channel 4. *Modulational instability.* In this channel, both high frequency sidebands become equally important even for $\omega \gg \gamma$, whenever $\omega/k = \partial\omega_0/\partial k_0$ can be satisfied, and the pump wave's amplitude gets modulated.

$$\frac{\partial\omega_0}{\partial k_{0\parallel}} = \frac{\omega_0}{k_{0\parallel}}(1 - \frac{\omega_{LH}^2}{\omega_0^2}) \simeq \frac{\omega}{k}\frac{k_\parallel}{k}, \tag{1.82}$$

$$\frac{\partial\omega_0}{\partial k_{0\perp}} = -\frac{\omega_0}{k_{0\perp}^2}(1 - \frac{\omega_{LH}^2}{\omega_0^2}) \simeq \frac{\omega}{k}\frac{k_\perp}{k}. \tag{1.83}$$

Since $k_{0\parallel} \ll k_{0\perp}$, these conditions are satisfied for $k_\perp \ll k_\parallel$, that is the low frequency wave mode propagates mainly along the magnetic field direction. The growth rate can be obtained as

$$\gamma = \frac{k_\parallel v_e}{\omega_0}\omega(\frac{m_e}{m_i})^{3/2}(1-\frac{\omega_{LH}^2}{\omega_0^2})(4-\frac{3\omega_{LH}^2}{\omega_0^2})\sin\delta_1\frac{U}{c_s}. \tag{1.84}$$

It can been seen that the growth rate is extremely low. This channel evolves into case A, channel 3 for a larger value of U/c_s.

Case B. $0.5 < k_\parallel v_e/\omega < 2.0$

This case corresponds to the nonlinear Landau damping by electrons and has the following decay channels.

Channel 1: lower hybrid quasi-mode and lower hybrid wave.

Channel 2: ion cyclotron or ion Bernstein quasi-modes and lower hybrid wave. Ion cyclotron mode has parallel phase velocity smaller than v_e, while the ion Bernstein quasi-mode's parallel phase velocity is larger than v_e.

The growth rates for all the channels in this case are estimated as well.

Channel 1. *Lower hybrid quasi-mode and lower hybrid wave.* In this channel the pump wave and the lower sideband can interact resonantly with the electrons under the resonance condition $\omega = \pm k_\parallel v_e$. This condition can be satisfied only when $\Omega_i \ll \omega \ll \omega_0$ for $\omega_{0,1} \gg k_{0,1\parallel} v_e$. Thus, the growth rate in this Chan can be calculated as

$$\gamma \simeq -\gamma_{1l} + 0.6(\frac{\omega_{LH}^2}{8\omega_0})\sin^2\delta_1(\frac{U^2}{c_s^2}). \tag{1.85}$$

The growth rate is very high and is believed to dominate the region with high density.

Channel 2. *Ion cyclotron quasi-mode and lower hybrid wave.* This channel may occur when the low frequency quasi-mode $\omega \sim \Omega_i$ or $\omega \simeq n\Omega_i$. In this channel, the

growth rate for the resonance condition $\omega \simeq k_\parallel v_e$ takes the form

$$\gamma_0 = i\frac{\omega_0}{2}\frac{\omega_{pi}^4}{\omega_0^2}\frac{\sin^2\delta}{4k^2c_s^2}\frac{U^2}{c_s^2}[1+Z(-1)]^2\frac{(\chi_e-\epsilon)/\chi_e}{(1+\omega_{pe}^2/\Omega_e^2)\epsilon}. \tag{1.86}$$

To simplify this expression, one can obtain

$$\gamma_0 = \frac{\omega_{LH}^2}{\omega_0^2}\sin^2\delta_1\frac{0.6}{8}\frac{U^2}{c_s^2}. \tag{1.87}$$

The quasi-modes decay channel can occur with another possibility when $\omega-\Omega_i \sim k_\parallel v_i$, the nonlinear ion cyclotron damping condition. In this channel, the growth rate can be estimated by taking the limit $\gamma < \omega - \Omega_i \sim k_\parallel v_i \ll \omega < k_\parallel v_e$.

$$\gamma_0 = \frac{0.6}{8}\frac{\omega_{LH}^2}{\omega_0}\sin^2\delta_1\frac{U^2}{c_s^2}\frac{T_e}{T_i}\frac{\omega I_1\exp(-b_i)}{k_\parallel v_i}\eta, \tag{1.88}$$

where

$$\eta^{-1} = 1+\frac{T_e}{T_i}[1-I_0\exp(-b_i)+0.3\frac{\omega I_1\exp(-b_i)}{k_\parallel v_i}]^2+[0.6\frac{T_e}{T_i}\frac{\omega I_1\exp(-b_i)}{k_\parallel v_i}]^2. \tag{1.89}$$

Case C. $k_\parallel v_e/\omega > 0.3$

In this case, there exists mainly three channels.

Channel 1: ion acoustic and lower hybrid waves (only for $\omega_0 > 4\omega_{LH}$ and $T_e > 4T_i$)

Channel 2: ion cyclotron and lower hybrid waves for $k_\perp\rho_i > 1$

Channel 3: oscillating two-stream instability

For all the channels, the growth rates can be obtained.

Channel 1. *Ion acoustic wave and lower hybrid wave.* The condition for this channel to occur is that $k_\parallel v_e \gg \omega \simeq kc_s \gg kv_i$ and, hence, $\omega_0 > 4\omega_{LH}$ and $T_e > 4T_i$.

For this channel, one can obtain the growth rate to be

$$\gamma_0^2 = [\frac{\omega_{LH}}{4\omega_0}(\omega\omega_0)^{1/2}\sin\delta_1\frac{U}{c_s}]^2. \tag{1.90}$$

In this case, the low frequency mode is a resonant quasi-mode.

Channel 2. *Ion cyclotron and lower hybrid waves.* In this case, the growth rate is

$$\gamma = \frac{\omega_{LH}}{\omega_0}\frac{[I_1\exp(-b_i)\Omega_i\omega_0]^{1/2}}{2\sqrt{2}(1+T_i/T_e)}\sin\delta_1\frac{U}{c_s}. \tag{1.91}$$

The approximations $\omega \sim \Omega_i$, $\omega - \Omega_i \gg k_\parallel v_i$, $k_\parallel \gg \omega$ ($k_\perp\rho_i > 1$), $\omega = \omega + i\gamma$ and $\gamma \ll \omega - \Omega_i$ are adopted in deriving the growth rate.

Channel 3. *Oscillating two-stream instability.* There are two possibilities in this decay channel.

(a) $\omega \ll k_\parallel v_e$, $k_\parallel v_i$. In this case, the dielectric function is

$$\epsilon \simeq (\omega_{pi}^2/k^2c_s^2)(1+T_e/T_i). \tag{1.92}$$

To consider the both high frequency sidebands, one can obtain the nonlinear dispersion relation

$$\omega^2 = \Delta^2 + \frac{\omega_{LH}^2}{\omega_0^2}\frac{\omega_0\Delta}{4(1+T_i/T_e)}\frac{U^2}{c_s^2}, \tag{1.93}$$

where $k_{0\parallel} \ll k_\parallel$, $\Delta \ll \omega_0$ and

$$\Delta = \omega_0 - \omega_{LH}(1+\frac{k_\parallel^2}{k^2}\frac{m_i}{m_e})^{1/2}. \tag{1.94}$$

For the purely growing mode to occur, $\Delta < 0$ and

$$\frac{\omega_{LH}^2}{4\omega_0(1+T_i/T_e)}\frac{U^2}{c_s^2} > |\Delta|. \tag{1.95}$$

One can obtain the maximum growth rate to be

$$\gamma_{max} = \frac{\omega_{LH}^2/\omega_0}{8(1+T_i/T_e)}\frac{U^2}{c_s^2}. \tag{1.96}$$

(b) $k_\parallel v_i \ll \omega \ll k_\parallel v_e$, compatible with $\omega \ll k_\parallel v_e$, and $Im\omega \geq \Omega_i$, the dielectric function is

$$\epsilon \simeq \frac{\omega_{pi}^2}{k^2 c_s^2}(1 + \frac{T_e}{T_i} + i\frac{T_e}{T_i}\frac{\omega\pi/\Omega_i}{(2\pi b_i)^{1/2}}). \tag{1.97}$$

If

$$\frac{T_e}{T_i}\frac{\omega}{\Omega_i}\frac{\pi}{(2b_i\pi)^{1/2}} \ll 1, \tag{1.98}$$

then the dispersion relation becomes the same as Eq. 1.93 and the growth rate is given by Eq. 1.96.

1.5 Summary

In this chapter, the physics of Landau damping and parametric instability of lower hybrid waves are reviewed. The theory of Landau damping, including both the linear and nonlinear Landau damping rates of Langmuir waves, is introduced. The main characteristics of the nonlinear Landau damping, such as the particles trapping and long time evolution into a final BGK equilibrium, etc, are discussed by referring to the recent published literatures. For the lower hybrid wave, the electromagnetic dispersion relation as well as the electrostatic dispersion relation in both cold and warm plasmas is introduced in great details. The coefficient of the linear electron Landau damping of LHWs is derived given the condition that the damping rate is much smaller than the real frequency. The important property of the Landau damping of LHWs, that unlike most other wave modes the LHWs can interact with both electrons and ions directly, is finally discussed. In the last section, the theory of PI is reviewed including both the electron and ion nonlinear response effects. The nonlinear

dispersion relation equation of the PI of LHWs is given as Eq. 1.70. Based on the theory and dispersion equation, various decay channels are categorized according to the quantity $k_{\parallel}v_e/\omega$. For the various possible decay channels, the growth rates are also estimated.

Chapter 2

GeFi Simulation Scheme

Numerical simulation is an advanced technique to understand the kinetic physics of various fundamental plasma processes, especially in the investigation of the nonlinear plasma dynamics under realistic conditions, for which the analytical theory is unable to be acquired. Full-particle simulations have been utilized for decades[37, 38, 39, 40]. In the full-particle codes, both electrons and ions are treated as fully kinetic particles, and thus the kinetic physics of both electrons and ions can be included in it. However, an artificial, small ion-to-electron mass ratio is often assumed in the full-particle codes in order to accomodate the computation resources. Another kinetic simulation approach is the hybrid simulation[41, 42], in which the ions are treated as fully kinetic particles, while the electrons are treated as a massless resistive fluid. Thus, the electron kinetic effects are absent in the hybrid model. Neither full-particle code scheme nor hybrid code scheme is appropriate to solve the physics of LHWs, which must include the dynamics of both electrons and ions, and requires a realistic ion-to-electron mass ratio. Note that the frequency of LHWs is in the range $\omega \geq \omega_{LH} \gg \Omega_i$, well above the range of the hybrid models.

A novel new simulation code model, GeFi model, has been developed by Lin, et. al.[35], recently. In the GeFi code model, the electron dynamics is determined by the gyrokinetic theory[43, 44, 45, 46, 47], and the ions are treated as fully kinetic particles governed by the Vlasov equation. In the GeFi model, the rapid electron gyro-motion is removed while finite Larmor radius effects are retained. This treatment allows us to deal with realistic ion-to-electron mass ratio and finite Larmor radii. This new model requires that the electron gyrokinetic approximation is valid, and thus is particularly

suitable for the dynamics with wave frequency $\omega < \Omega_e$ and $k_\parallel < k_\perp$. It can be seen from the discussions in chapter 1 that the lower hybrid wave falls exactly in this range. It is therefore suitable to simulate the dynamic physics of the LHWs, such as its Landau damping, parametric instability, and the electron-ion hybrid instability, using the GeFi code model.

2.1 GeFi Scheme Algebras

The GeFi simulation scheme treats ions as fully kinetic (FK) particles and electrons as gyrokinetic (GK) particles.[35] For the FK ions, the dynamics is governed by Vlasov equation in the six-dimensional phase space ($\mathbf{x}$, $\mathbf{v}$).

$$\frac{\partial f_i}{\partial t} + \mathbf{v} \cdot \frac{\partial f_i}{\partial \mathbf{x}} + \frac{q_i}{m_i}(\mathbf{E} + \frac{1}{c}\mathbf{v} \times \mathbf{B}) \cdot \frac{\partial f_i}{\partial \mathbf{v}} = 0. \tag{2.1}$$

m_i is the ion mass, q_i is the ion charge, $\mathbf{E}$ is the electric field, $\mathbf{B}$ is the magnetic field, and f_i is ion distribution function. f_i is represented by a group of particles

$$f_i(\mathbf{x}, \mathbf{v}, t) = \sum_j \delta[\mathbf{x} - \mathbf{x}_j(t)]\delta[\mathbf{v} - \mathbf{v}_j(t)], \tag{2.2}$$

where the index j represents individual particles. The evolution of f_i is determined by ion motion under self-consistent electromagnetic fields, i.e.

$$\begin{aligned} \frac{d\mathbf{v}}{dt} &= \frac{q_i}{m_i}(\mathbf{E} + \mathbf{v} \times \mathbf{B}), \\ \frac{d\mathbf{x}}{dt} &= \mathbf{v}. \end{aligned} \tag{2.3}$$

The number density, n_i and current density, $\mathbf{J}_i$ can be obtained

$$
\begin{aligned}
n_i &= \int f_i d^3v = \sum_j \delta(\mathbf{x} - \mathbf{x_j}), \\
\mathbf{J}_i &= q_i \int f_i \mathbf{v} d^3v = q_i \sum_j \mathbf{v}_j \delta(\mathbf{x} - \mathbf{x}_j).
\end{aligned} \tag{2.4}
$$

The electrons are treated as gyrokinetic particles. The following GK ordering for electrons is adopted

$$
\begin{aligned}
\frac{\omega}{\Omega_e} &\sim \frac{\rho_e}{L} \sim k_\parallel \rho_e \sim \frac{\delta B}{B} \sim \epsilon, \\
k_\perp \rho_e &\sim 1.
\end{aligned} \tag{2.5}
$$

Here, $\rho_e = v_{te}/\Omega_e$ denotes the electron Larmor radius, L is the macroscopic background plasma scale length, δB represents the perturbed magnetic field, and ϵ is a smallness parameter. The coordinates $(\mathbf{x}, \mathbf{v})$ are transformed to the gyrocenter coordinates $(\mathbf{R}, p_\parallel, \mu, \zeta)$, where $\mathbf{R} = (\mathbf{x} - \rho)$ is the gyrocentre position with $\rho = (\mathbf{b} \times \mathbf{v}_{\perp e})/\Omega_e$ being the gyroradius vector, $p_\parallel = m_e v_{e\parallel} + q_e A_\parallel / c$ the parallel canonical momentum of electrons, $v_{e\parallel}$ and $v_{e\perp}$ the parallel and perpendicular velocities of electrons, respectively, q_e the electron charge, μ the magnetic moment, $\mathbf{b} = \mathbf{B}/B$, $\mathbf{B} = \bar{\mathbf{B}} + \delta\mathbf{B}$ with $\bar{\mathbf{B}}$ being the background magnetic field averaged over the spatial and temporal scales of wave perturbations, and $\delta\mathbf{B} = \nabla \times \mathbf{A}$ the perturbed magnetic field. The parallel direction is defined along the background magnetic field $\bar{\mathbf{B}}$. The following GK equation can be obtained by averaging the Vlasov equation over the gyrophase angle ζ

$$
\frac{\partial F_e}{\partial t} + \frac{d\mathbf{R}}{dt} \cdot \frac{\partial F_e}{\partial \mathbf{R}} + \frac{dp_\parallel}{dt} \frac{\partial F_e}{\partial p_\parallel} = 0, \tag{2.6}
$$

where $F_e(\mathbf{R}, p_\parallel, \mu)$ is the distribution function of electron in the five-dimensional gyrocenter phase space. The gyrocenter equations of motion for $p_\parallel$ and $\mathbf{R}$ are

$$\begin{aligned} \frac{dp_\parallel}{dt} &= -\mathbf{b}^* \cdot [q_e < \nabla\phi^* > +\mu\nabla\bar{B}], \\ \frac{\mathbf{R}}{dt} &= v_{e\parallel}\mathbf{b}^* + \frac{c}{q_e\bar{B}}\bar{\mathbf{b}} \times [q_e < \nabla\phi^* > +\mu\nabla\bar{B}], \end{aligned} \tag{2.7}$$

where $\mathbf{b}^* = \bar{\mathbf{b}} + (v_{e\parallel}/\Omega_e)\bar{\mathbf{b}} \times (\bar{\mathbf{b}} \cdot \nabla)\bar{\mathbf{b}}$, $\bar{\mathbf{b}} = \bar{\mathbf{B}}/\bar{B}$, $\phi^* = \phi - \mathbf{v} \cdot \mathbf{A}/c$, ϕ and $\mathbf{A}$ are perturbed scalar and vector potentials, respectively, and the operator $< \cdots >$ represents gyro-averaging. The electron gyro-averaged guiding centre charge density and $p_\parallel$ current are

$$\begin{aligned} < N_e > &= \int F_e d^3v, \\ < J_{e\parallel} > &= \frac{q_e}{m_e}\int p_\parallel F_e d^3v. \end{aligned} \tag{2.8}$$

In GK simulations, the gyro-averaging is carried out numerically on a discretized gyro-orbit in real space[48].

In order to advance F_e and f_i, we need to calculate the perturbed potentials and fields from the Maxwell equations. The Poisson's equation becomes

$$\nabla_\perp^2\phi = -4\pi(q_i n_i + q_e n_e), \tag{2.9}$$

where n_e is the electron number density, and for $w = v^2/2$,

$$n_e = \frac{q_e}{m_e}\int d^3v(\frac{\partial\bar{f}_e}{\partial w})[\phi - < \phi > + \frac{1}{c} < \mathbf{v}_\perp \cdot \mathbf{A} >] + < N_e > . \tag{2.10}$$

Assuming $|\nabla_\perp^2| \gg |\nabla_\parallel^2|$, we have replaced $\nabla^2\phi$ by $\nabla_\perp^2\phi$ in Eq. 2.9 to suppress the undesirable high-frequency Langmuir oscillation along $\mathbf{B}$. Eq. 2.9 along with 2.10

then become the following generalized GK Poisson's equation

$$(1+\frac{\bar{\omega}_{pe}^2}{\bar{\Omega}_e^2})\nabla_\perp^2\phi+4\pi\bar{n}_e q_e\frac{\delta B_\parallel}{\bar{B}}=-4\pi(q_i n_i+q_e<N_e>), \tag{2.11}$$

where $\bar{n}_e$ is the spatially averaged electron density, $\delta B_\parallel=\bar{\mathbf{b}}\cdot\delta\mathbf{B}$, and the second and third terms on the left-hand side correspond to the electron density due to its perpendicular guiding-centre polarization drift of the electrostatic electric field and $\mathbf{E}\times\mathbf{B}$ drift associated with inductive electric field $\partial\mathbf{A}_\perp/\partial t$, respectively.

Since $\omega\ll\Omega_e$, the electron force balance instead of the usual perpendicular Ampere's law is used to calculate $\delta B_\parallel$.

$$\nabla\cdot(n_e q_e\mathbf{E})=\nabla\cdot[\nabla\cdot\mathbf{P}_e-\frac{1}{c}\mathbf{J}_e\times\mathbf{B}], \tag{2.12}$$

where

$$\begin{aligned}\mathbf{P}_e &= (\bar{n}_e q_e\rho_e^2\nabla_\perp^2\phi+2\bar{n}_e T_e\frac{\delta\bar{B}_\parallel}{\bar{B}})(\mathbf{I}-\frac{1}{2}\bar{\mathbf{B}}\bar{\mathbf{B}})+<\mathbf{P}_g>,\\ <\mathbf{P}_g> &= \int m_e\mathbf{v}\mathbf{v}F_e d^3v,\end{aligned} \tag{2.13}$$

and, analogous to the derivation of n_e, the first two terms in the expression for $\mathbf{P}_e$ are due to the electron perpendicular guiding-centre drifts. Assuming zero background electric field, $\mathbf{E}=\delta\mathbf{E}$. Noting that $\delta\mathbf{E}=-\nabla\phi-(1/c)\partial\mathbf{A}/\partial t$, $\nabla\cdot\mathbf{A}=0$, the electron current density $\mathbf{J}_e=(c/4\pi)\nabla\times\mathbf{B}-\mathbf{j}_i$ with $\mathbf{j}_i$ being the ion current density, $|\nabla_\perp^2|\gg|\nabla_\parallel^2|$, and ignoring corresponding higher-order terms, Eq. 2.12 can then be shown as

$$\nabla^2\Psi=-\nabla\cdot(\nabla\cdot\mathbf{P}_g+\frac{1}{c}\mathbf{J}_i\times\mathbf{B}), \tag{2.14}$$

where, noting $\bar{n}_e q_e=-\bar{n}_i q_i$,

$$\Psi=\frac{(1+\bar{\beta}_e)\bar{B}\delta B_\parallel}{4\pi}-\bar{n}_i q_i(1+\rho_e^2\nabla_\perp^2)\phi. \tag{2.15}$$

Expressing $\delta B_\parallel$ in terms of Ψ, given by Eq. 2.15, the GK Poisson's equation, Eq. 2.11, can finally be expressed as

$$[(1+\bar{\beta}_e+\frac{\bar{\omega}_{pe}^2}{\bar{\Omega}_e^2})\nabla_\perp^2-\frac{\bar{\omega}_{pi}^2}{\bar{V}_A^2}]\phi=-4\pi[(1+\bar{\beta}_e)(q_i n_i+q_e<N_e>)-\frac{4\pi\bar{n}_i q_i}{\bar{B}^2}\Psi], \quad (2.16)$$

where $\bar{\omega}_{pi}$ and $\bar{V}_A$ are the background ion plasma frequency and the Alfvén speed, respectively.

The perturbed potential $A_\parallel$, meanwhile, is given by the following parallel Ampere's law

$$(\nabla^2-\frac{\omega_{pe}^2}{c^2})A_\parallel=-\frac{4\pi}{c}(J_{i\parallel}+<J_{e\parallel}>). \quad (2.17)$$

Given $A_\parallel$ and $\delta B_\parallel$, the vector potential $\mathbf{A}$ can be calculated. Let us decompose $\mathbf{A}$ into three locally orthogonal components, i.e. $\mathbf{A}=\mathbf{A}_\perp+\mathbf{A}_\parallel\bar{\mathbf{b}}+\nabla_\perp\xi$. $\mathbf{A}_\perp$ is then determined by the perpendicular Ampere's law

$$\nabla^2\mathbf{A}_\perp=-\frac{4\pi}{c}\mathbf{J}_\perp, \quad (2.18)$$

where $\mathbf{J}_\perp=(c/4\pi)\nabla\times\delta\mathbf{B}_\parallel$. $\nabla_\perp\xi$, meanwhile, can be determined by the Coulomb gauge $\nabla\cdot\mathbf{A}=0$ or $\nabla_\perp^2\xi=-\nabla\cdot(A_\parallel\bar{\mathbf{b}})$.

With $\mathbf{A}$ being completely specified, the perturbed magnetic field $\delta\mathbf{B}$ is simply $\delta\mathbf{B}=\nabla\mathbf{A}$. Since $\omega\ll\Omega_e$, the electric field $\mathbf{E}$ that goes into the ion equation motion can be calculated from the following electron force balance equation,

$$n_e q_e\delta\mathbf{E}=-\nabla\cdot\mathbf{P}_e-\frac{1}{c}\mathbf{J}_e\times\mathbf{B}. \quad (2.19)$$

The calculated $\delta\mathbf{E}$ and $\mathbf{B}=\bar{\mathbf{B}}+\delta\mathbf{B}$ can then be used to advance ions.

2.2 GeFi model in the electrostatic limit

In this thesis, all work is done with electrostatic GeFi particle simulations, although the GeFi model is electromagnetic. When considering the GeFi model in the electrostatic limit, equations can be simplified in the following.

For ions, the dynamics is governed by the Vlasov equation in six-dimensional phase space. (Here, all symbols have the same meanings as that in the last section.)

$$\frac{\partial f_i}{\partial t} + \mathbf{v} \cdot \frac{\partial f_i}{\partial \mathbf{x}} + \frac{q_i}{m_i}(\mathbf{E} + \frac{1}{c}\mathbf{v} \times \bar{\mathbf{B}}) \cdot \frac{\partial f_i}{\partial \mathbf{v}} = 0. \tag{2.20}$$

The evolution of f_i is determined by ion motion under self-consistent electromagnetic fields, i.e.

$$\begin{aligned} \frac{d\mathbf{v}}{dt} &= \frac{q_i}{m_i}(\mathbf{E} + \mathbf{v} \times \bar{\mathbf{B}}), \\ \frac{d\mathbf{x}}{dt} &= \mathbf{v}. \end{aligned} \tag{2.21}$$

In the gyrokinetic approximations for electrostatic electrons, the gyrocenter equations of motion for parallel electron momentum $p_\parallel = m_e v_{e\parallel}$ and the electron gyrocenter position $\mathbf{R}$ are given by

$$\begin{aligned} \frac{dp_\parallel}{dt} &= -\mathbf{b}^* \cdot [q_e < \nabla\phi > +\mu\nabla\bar{B}], \\ \frac{\mathbf{R}}{dt} &= v_{e\parallel}\mathbf{b}^* + \frac{c}{q_e\bar{B}}\bar{\mathbf{b}} \times [q_e < \nabla\phi > +\mu\nabla\bar{B}], \end{aligned} \tag{2.22}$$

where $\mathbf{b}^* = \bar{\mathbf{b}} + (v_{e\parallel}/\Omega_e)\bar{\mathbf{b}} \times (\bar{\mathbf{b}} \cdot \nabla)\bar{\mathbf{b}}$, $\bar{\mathbf{b}} = \bar{\mathbf{B}}/\bar{B}$, ϕ is electrostatic potential, and the operator $< \cdots >$ represents gyro-averaging.

Assuming the gyrokinetic condition, $k_\parallel/k \ll 1$ and thus $\nabla_\perp^2 \gg \nabla_\parallel^2$, the electric field is solved by the generalized gyrokinetic Poisson equation for the perturbed scalar potential in electrostatic limit

$$(1+\frac{\bar{\omega}_{pe}^2}{\bar{\Omega}_e^2})\nabla_\perp^2\phi = -4\pi(q_i n_i + q_e < N_e >), \tag{2.23}$$

2.3 Benchmark of the GeFi Scheme

The above GeFi scheme has been benchmarked for a one-dimensional uniform system. The background magnetic field is in the xz plane and the wave vector $\mathbf{k}$ is assumed to be along x direction.

The top plot of Fig. 2.1 shows a comparison between the dispersion relations of δB_z for the fast magnetosonic/whistler branch obtained from the kinetic GeFi simulation (open dots), and the corresponding analytical linear dispersion relations (solid lines). The parameters in this benchmark are $\beta_e = \beta_i = 0.04$, $m_i/m_e = 1836$, and $k_\parallel/k_\perp = 0.2$, 0.06 and 0 are plotted. In the case with $k_\parallel = 0$ the electromagnetic mode approaches the quasi-electrostatic lower hybrid mode, and the frequency $\omega/\Omega_i = \sqrt{m_i/m_e} = 42.8$. The bottom plot of Fig. 2.1 is the comparison between the dispersion relations of δB_y for the shear Alfvén/kinetic Alfvén mode branch obtain from GeFi simulation and the analytical theory for $k_\parallel/k_\perp = 0.06$. The analytical solution of the MHD shear Alfvén mode, $\omega/\Omega_i = k_\parallel V_A/\Omega_i = 0.42$, is also shown as the dashed line. It can be seen from the figure, the GeFi simulation results are in excellent agreement with the theoretical analysis for $k_\parallel \ll k_\perp$.

2.4 Summary

In this chapter, the original new GeFi kinetic simulation scheme is introduced. This new scheme, in which the electrons are treated as GK particles and ions are treated as FK particles, is particularly applicable to problems in which the wave modes ranging from magnetosonic and Alfvén waves to lower-hybrid/whistler waves need to be handled on an equal footing. To utilize this code, the simulated physical processes should be dominated by wave frequencies $\omega < \Omega_e$, and wave numbers $k_\parallel < k_\perp$. With

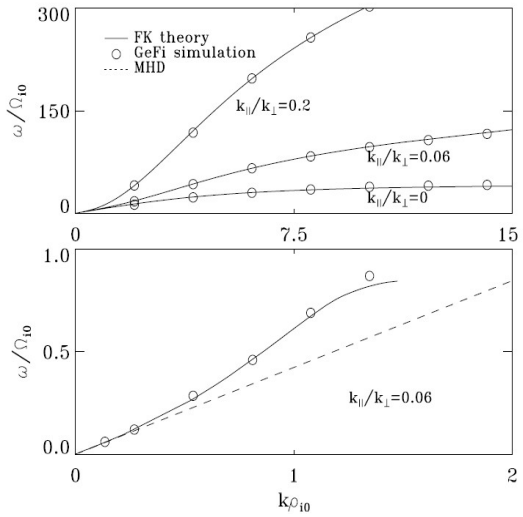

Figure 2.1: Comparison between the dispersion relations obtained from the kinetic GeFi simulation and the corresponding analytical linear dispersion relations for various $k_{\parallel}/k_{\perp}$. Top plot is δB_z in the fast magnetosonic/whistler branch. Bottom plot is δB_y in the shear Alfvén/kinetic Alfvén mode branch. The dashed line shows the analytical dispersion relation of the MHD shear Alfvén mode.

fast electron gyro-motion and Langmuir oscillations removed from the dynamics, the GeFi model can readily employ realistic m_i/m_e mass ratio. As discussed above, the GeFi model has been improved and modified to allow the existence of modes with wavelengths on the same scale of the background nonuniformity. The novel GeFi scheme has already been benchmarked for uniform plasmas to resolve the physics of wave modes ranging from Alfvén waves to lower hybrid/whistler waves, and for the tearing mode instability in the magnetic reconnection in a Harris current sheet.

Chapter 3

GeFi Simulation of Landau Damping of Lower Hybrid Waves

3.1 Introduction

In this chapter, the GeFi model is used to simulate the Landau damping of LHWs. Both linear and nonlinear Landau damping of LHWs in the electrostatic limit will be studied. The results, based on an initial value problem, will provide a basic understanding of the Landau damping of LHWs from the lower-hybrid to the ion cyclotron time scales. The real frequency and linear damping rates from the linear Landau damping simulations will be compared with the theoretical predications from the dispersion relation. The nonlinear Landau damping characteristics, including the long time evolution, nonlinear Landau damping rates and the motions of both resonant electrons and ions will be studied in great details. In either linear or nonlinear Landau damping of LHWs, electric current can be driven through the process that waves and particles exchange energy and momentum. Although our investigations of Landau damping of LHWs are based on an initial value problem, it is of interest for us to calculate the current driven in the Landau damping. For various parameters, the driven currents will be presented in the last section of this chapter.

3.2 Simulation Model

Here, it is time to introduce the normalizations and some main parameters in the simulation of LHWs. In the calculation, the time is normalized to the inverse of the electron cyclotron frequency Ω_e, lengths are normalized to the electron Larmor radius ρ_e, velocities are normalized to the electron thermal speed V_{te}, electric field

is normalized to $E_n = V_{te}B_0/c$ (with B_0 being the background magnetic field and c the light speed), temperatures are normalized to the electron temperature T_e, and densities are normalized to the equilibrium electron particle density n_0. The particle initial distribution is assumed to be Maxwellian. The simulation is carried out as an initial value problem in a one-dimensional uniform domain in the x direction (i.e., the wave vector $\mathbf{k} = k_x\widehat{e_x}$). Periodic boundary conditions are used for both boundaries.

The main parameters are set as the following. The ion-to-electron mass ratio is $m_i/m_e = 1836$. The grid number N_x varies from 256 to 2048 for different cases, and the particle number per cell varies from 1000 to 10,000 for both electrons and ions. The time increment is $\Omega_e\Delta t = 0.5$. The ratio $c/V_A = 42.8$, and V_A is the Alfvén speed. The electron plasma frequency is thus $\omega_{pe} = \Omega_e(c/V_A)\sqrt{m_e/m_i} = 1.0$, and the ion plasma frequency $\omega_{pi} = \omega_{pe}/\sqrt{1836} = 0.023$. The ion-to-electron temperature ratio T_i/T_e varies from 0.33 to 4.0. The background magnetic field, which has a fixed magnitude $|\mathbf{B_0}| = 1.0$, is assumed to be in the xy plane, with the ratio B_{0x}/B_{0y} varying from 0.001 to 0.1. Accordingly, the ratio $k_\parallel/k$ varies from 0.001 to 0.1.

3.3 Simulation of linear ELD of LHWs

The linear electrostatic LHWs in a uniform plasma have been simulated using the GeFi scheme, under a small perturbed electric amplitude $E_0 = 0.001$ (E_0 is the initial amplitude). As discussed in Chapter 1.1, $\gamma_L\tau \ll 1$, we consider the process mainly as nonlinear Landau damping, otherwise, we consider the damping as linear Landau damping. Here, $\tau = \sqrt{m_e/eE_\parallel k_\parallel}$ is the electron trapping frequency in LHWs. Thus, in order to satisfy the linear Landau damping condition, we need to set up a small electric amplitude. In our case, $E_0 = 0.001$ is small enough to go through a linear ELD. Moreover, since the electric field is small, it is necessary for us to lower down the noise level to observe obvious decay. About 10,000 particles are used in each grid in order to simulate the LHWs in the small amplitude, at low noise levels.

In each run, only a mode with a single **k** is kept in the domain, while all other modes are filtered in order to single out the damping source in the electron wave-particle interaction.

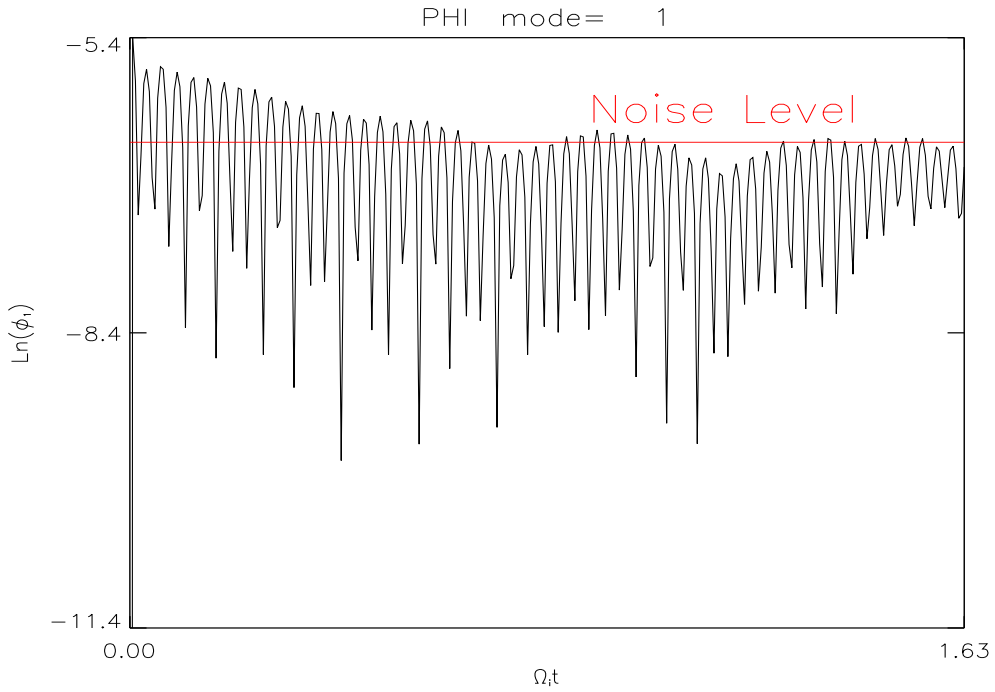

Figure 3.1: Perturbed electrostatic potential ϕ_1 (in logarithm scale) vs. $\Omega_i t$ for a case of linear electron Landa damping of LHWs

Fig. 3.1 is a plot of perturbed electrostatic potential ϕ_1, in a logarithm scale, as a function of time $\Omega_i t$ for a typical case of linear ELD of LHWs. In this case $k_\parallel/k = 0.066$, an electron Landau damping case. The red line shows approximately the noise level. In order to obtain a clear linear damping in logarithm, the grid number $N_x = 2048$ and the particle number in cell 10,000 are used. It is seen from Fig. 3.1, the amplitude of the potential decays into the noise level directly, and never bounce back. Since the time for the amplitude to decay into noise level is very short, the nonlinear effects can not be involved, thus the purely linear ELD happens.

Here, it is necessary to clarify that our simulations are performed only 1D in x direction, although the LHWs propagate nearly perpendicular to the external static

magnetic field. In order to simulate the LHWs, we put the magnetic field at x and y directions, and put the wave vector k in only x direction. Thus the important ratio, $k_\parallel/k$ in the real frequency calculation, is just B_{0x}/B_0. The LHWs are embedded into our simulation system by perturbing the ion density, $n_{i0} = a_0 \cos(k_x x)$ with a_0 being the initial amplitude of the perturbed ion density. Note that the perturbation is not depending on time, thus this is an initial value problem.

In order to compare our simulation results of the linear ELD of LHWs with the corresponding linear theories, the real frequency and the linear ELD rate as a function of the wave number, $k\rho_e$ are plotted as Fig. 3.2 for magnetic field $B_{0x} = 0.0659$ and $B_{0y} = 0.999$, which corresponds to a fixed $k_\parallel/k = 0.066$, while $k\rho_e$ varies from 0.15 to 0.30. The temperature ratio $T_i/T_e = 1.0$, and the initial wave amplitude $E_0 = 0.001$. In Fig. 3.2, the top plot is the real frequency and the bottom one is the linear ELD rate, and the error bars are estimated based on the uncertainties in FFT introduced to the frequency space due to discrete data points in the finite time sequence. It is seen from Fig. 3.2 that the real frequency has a good match with the theoretical predictions from Eq. 1.21, which is shown by the solid curve in the figure. The linear ELD rate, γ_L/Ω_i as a function of $k\rho_e$ also agrees very well with the theoretical predications given as Eq. 1.37. For $k\rho_e < 0.19$, we expect very low linear electron Landau damping rate, i.e., $\gamma_L/\Omega_i \sim 0$. The damping rate grows nearly exponentially with respect to $k\rho_e$. The results of Fig. 3.2 show that the GeFi model is really good for the simulation of LHWs.

3.4 Nonlinear Landau Damping of Lower Hybrid Waves

As discussed above, we can increase the perturbed electric field, E_0, to obtain the nonlinear ELD of LHWs. The nonlinear ELD of LHWs is discussed in this section with lots of interesting properties. In Section 1.3.2, we have discussed that both electrons and ions can interact with the LHWs. The electrons are usually treated

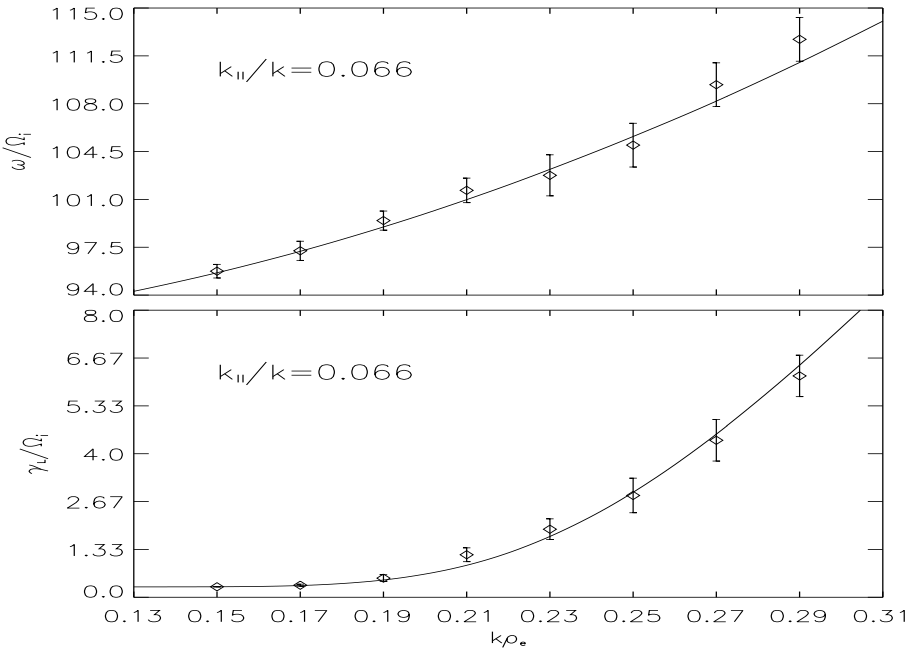

Figure 3.2: Diamonds show the real frequency and the linear ELD rate as a function of the wave number for LHWs with $B_{0x} = 0.0659$ and $B_{0y} = 0.999$, which corresponds to a fixed $k_\parallel/k = 0.066$, and $T_i/T_e = 1.0$. The solid lines are based on the analytical theory.

as magnetized, their gyro-motions cannot be neglected, and they interact resonantly with the waves when the condition, $\omega = k_\parallel v_{e\parallel}$, is satisfied. However, the ions are always treated as unmagnetized, so their gyromotions may be neglected and they interact resonantly with the waves when the condition, $\omega = \mathbf{k} \cdot \mathbf{v}_i$, is satisfied. Here, $\mathbf{v}_e$ and $\mathbf{v}_i$ are the velocities of an electron and ion, respectively. Here, in this section, both electron and ion Landau damping of LHWs will be studied. The long time evolution of the propagation of LHWs and the particles trapping in the nonlinear Landau damping will be presented in details. Among other runs, three cases are discussed in details. In case 1, only electrons are resonant with LHWs. Only ions are resonant with the wave in case 2. Both electrons and ions are resonant in case 3.

3.4.1 Case 1, Electron Landau Damping of LHWs

Wave profile in case 1

In case 1, $k_\parallel/k = 0.066$, the ion-to-electron temperature ratio $T_i/T_e = 1.0$, and the initial perturbed wave amplitude $E_0 = 0.1$, the wave number $k\rho_e = 0.2255$, the real frequency is thus calculated, $\omega = 103.41\Omega_i = 3.03\omega_{LH}$. The resonant condition for electrons are calculated, $\omega/(k_\parallel V_{te}) = 3.78$, thus the electrons at the tail part of the velocity distribution can satisfy the electron resonant condition, $\omega = k_\parallel v_{e\parallel}$. On the other hand, the ion resonant condition is calculated, $\omega/(kV_{ti}) = 10.69 \gg 1$ (with $V_{ti} = \sqrt{\kappa T_i/m_i}$ being the ion thermal speed), which results in that almost none of the ions can satisfy the resonant condition, $\omega = \mathbf{k} \cdot \mathbf{v}_i$.

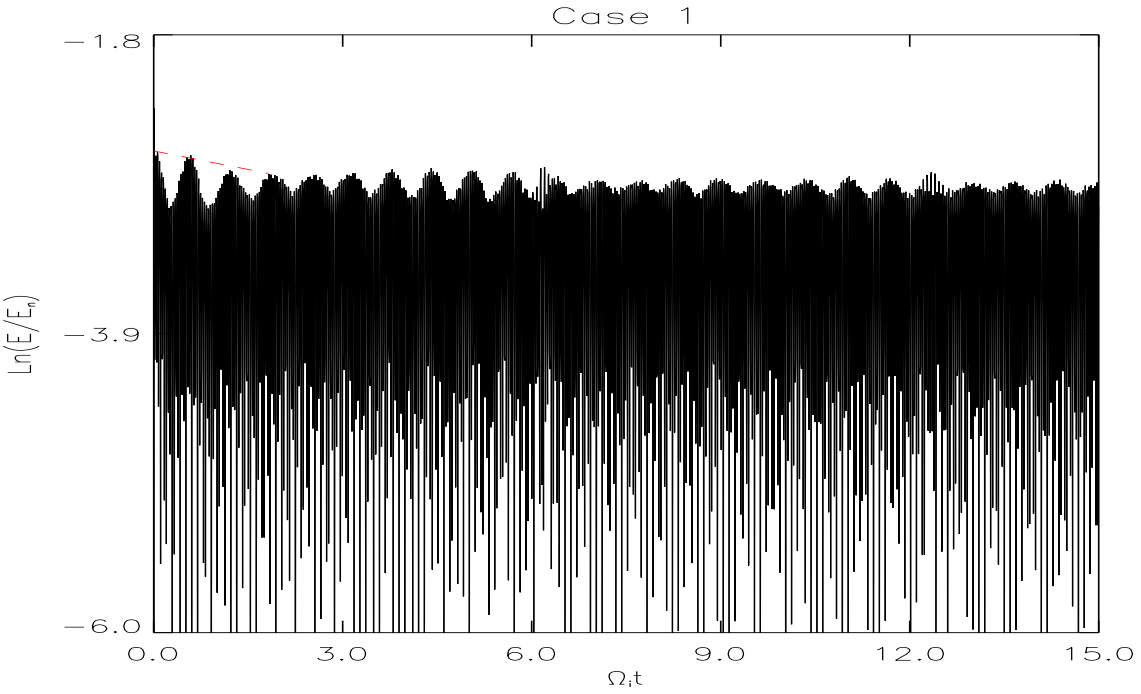

Figure 3.3: Time evolution of the spatial Fourier mode of the electric field (in the natural logarithm scale) for case 1 with $k_\parallel/k = 0.066$ and $T_i/T_e = 1.0$, and $k\rho_e = 0.2255$, $E_0 = 0.1$.

Fig. 3.3 shows the time evolution of the spatial Fourier modes of the electric field (in the natural logarithm scale) in case 1. Compared with Fig. 3.1, which is purely

linear ELD, the LHW profile of case 1 is seen to go through an electron nonlinear Landau damping, in which the wave amplitude oscillates and slowly decreases. After a few oscillations, the amplitude settles down to a steady oscillation, which is very above the noise level. In essence, As discussed in section 1.1.2, O'Neil's[2] theory has already indicated that large amplitude waves trap the resonant electron population, and thus the Landau damping is dominated by the nonlinear effects. The nonlinear damping rate can be measured as $\gamma/\Omega_i = 0.07$ based on the red dash line in the figure. As the electrons bounce back and forth inside the potential well of the wave, the wave amplitude oscillates with nearly the particle trapping time scale. The phase mixing of the trapped electrons causes the wave amplitude to reach an asymptotic constant, forming a stable equilibrium with an undamped nonlinear plasma wave, i.e., the BGK equilibrium.[4]

Particle motion, electron trapping in case 1

The particles' trapping in the wave electric field potential plays an important role in the nonlinear ELD of LHWs. In order to see the evolution of the electrons trapped in the electron Landau damping of LHWs, it is shown in Fig. 3.4 the contour plots of the electron distributions in the $(x, v_{e\|})$ phase space and the corresponding average parallel velocity distribution functions at times $\Omega_i t$ = 0,0.22,2.41 and 8.78 obtained in case 1, in which only electrons are resonant with the waves. The electron distribution functions are plotted with the black solid curves, and the ion distribution functions are shown with the red curves. Note that for the purpose of presentation, here, the ion velocities are normalized to the ion thermal speed V_{ti}. It can be seen from Fig. 3.4a that the electron distribution gradually forms a vortex structure in the phase space at $\Omega_i t = 0.22$, roughly around the parallel (to the magnetic field) phase velocity $v_{er}/V_{te} = \omega/(k_\| V_{te}) = 3.785$ of the LHW. Note that a similar structure can be found at the corresponding negative velocities since the wave propagates in both

the positive and negative directions, although only the $v_{e\|} > 0$ space is shown in the contour plots. Correspondingly, in Fig. 3.4b for $\Omega_i t = 0.22$, the black solid line at $v_{e\|} > 0$ side shows that the electron parallel velocity distribution function deviates strongly from the initial Maxwellian distribution in the region around the resonance speed $v_{er}/V_{te} = 3.785$, as marked by the black vertical dashed line. On the other hand, nothing happens to the ion velocity distribution function, as shown by the red solid line in the same plot, confirming that no ions resonate with the LHW.

As time increases, more electrons are trapped, and the vortex structure as well as the pair of "plateaus" in the distribution function finally reach a steady state, corresponding to the final BGK equilibrium. The steady structures are propagating with the wave along the x direction. Therefore, the number of electrons that can be trapped in the waves is finite for any arbitrarily long time.

3.4.2 Case 2, Ion Landau Damping of LHWs

Wave profile in case 2

In case 2, $k_\|/k = 0.001$, the ion-to-electron temperature ratio $T_i/T_e = 1.0$, the initial perturbed wave amplitude $E_0 = 0.1$, and the wave number $k\rho_e = 0.2255$. The real frequency is then calculated, $\omega = 37.24\Omega_i = 1.09\omega_{LH}$. The resonance condition for electrons yields to be $\omega/(k_\| V_{te}) = 90 \gg 1$, and for ions, the condition becomes $\omega/(kV_{ti}) = 3.85$. Thus none of the electrons can satisfy the resonant condition, $\omega = k_\| v_{e\|}$, but ion at the tail part of the distribution can satisfy the resonant condition $\omega = \mathbf{k} \cdot \mathbf{v}_i$. Therefore, only ions can be resonant with the LHWs in this case.

Fig. 3.5 shows the time evolution of the spatial Fourier modes of the electric field, in a natural logarithm scale, in case 2, in which only the ion Landau damping is present. It is seen from the figure, the wave amplitude decreases linearly with time on the logarithm to a level that is much smaller than the saturation level for case 1 that is dominated by the electron nonlinear Landau damping, as seen in Fig.3.3. The

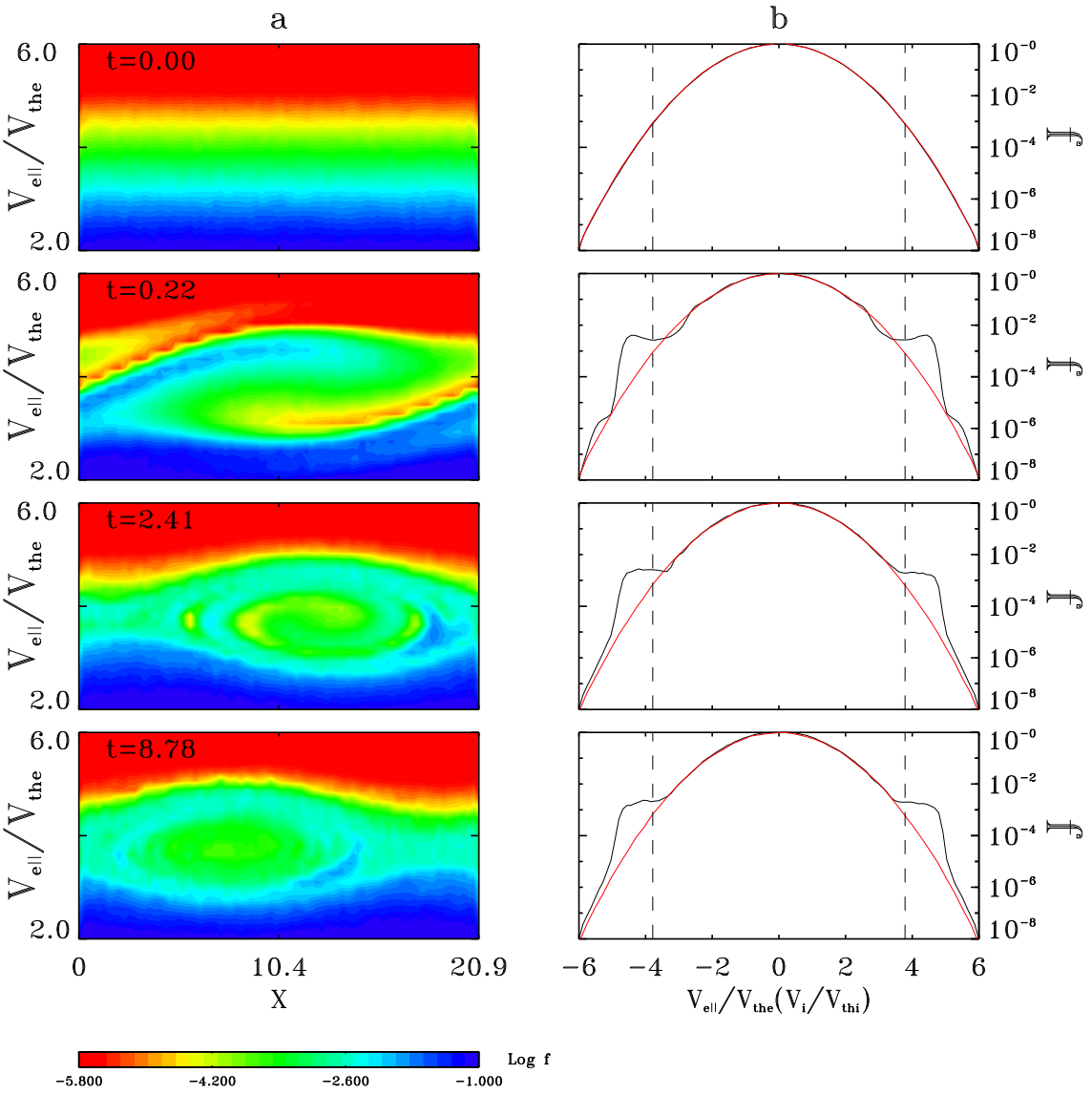

Figure 3.4: (a) Contour plots of the electron distributions in the particle phase space $(x, v_{e\|})$ and (b) the corresponding parallel velocity distribution functions averaged over x, shown with the black solid curves, at times $\Omega_i t$ = 0,0.22,2.41 and 8.78 obtained from Case 1. All the distribution functions are plotted in the logarithm scales The red solid lines show the ion distribution functions, and the black dashed lines show the electron resonant phase velocity $v_{er} = 3.785 V_{te}$ based on the theoretical prediction. The ion velocities are normalized to the ion thermal speed.

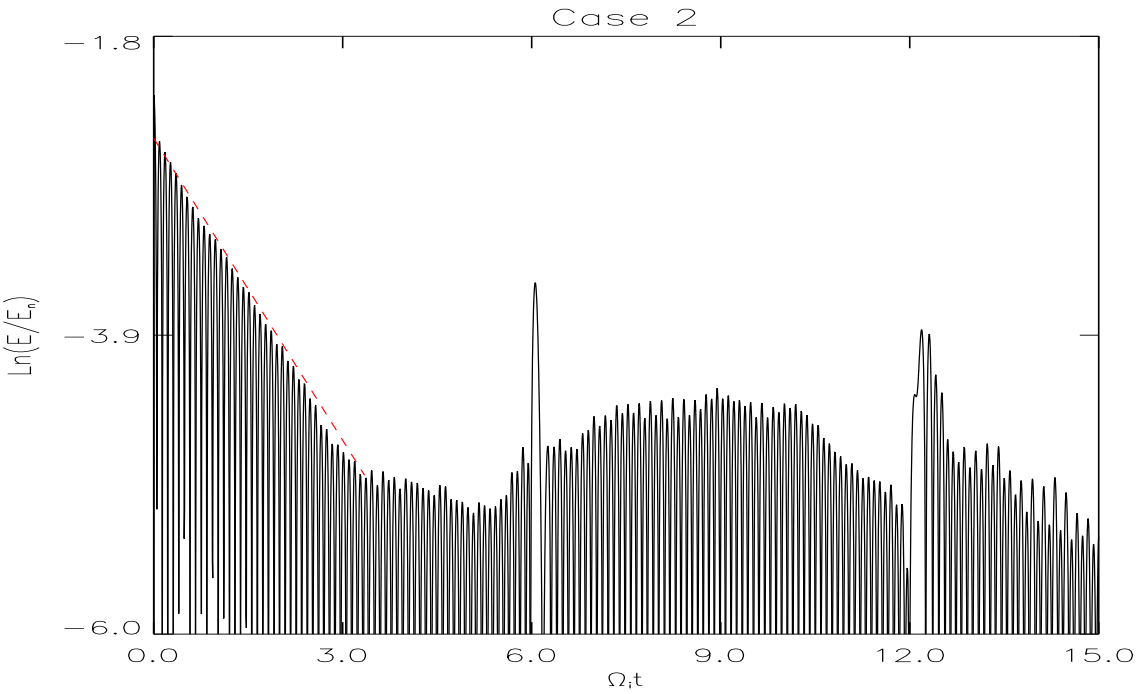

Figure 3.5: Time evolution of the spatial Fourier mode of the electric field (in the natural logarithm scale) for case 2 with $k_\parallel/k = 0.001$, $T_i/T_e = 1.0$, $k\rho_e = 0.2255$, and $E_0 = 0.1$.

simulation thus indicates that ions interact with LHWs mainly through the linear Landau damping. After the wave has reached a weak (but still above the noise) level, the wave amplitude is seen to oscillate on a long time scale with period $\sim 2\pi/\Omega_i$. Such long-period pattern is due to that on the time scale much longer than the LHW period, ions are still magnetized, trapped, and gyrating with frequency $\omega \simeq \Omega_i$. Therefore, the Landau damping dynamics is of a broad/hybrid frequency range of both ω_{LH} and Ω_i. In addition, the wave amplitude shows a sudden jump, followed by a sudden damp, at time intervals of $\Delta t \simeq 2\pi/\Omega_i$. This sudden jump and damp phenomenon is due to the phase bunching of ions, and will be investigated in section 3.6.

Particle motion in case 2

Here, we present the particle dynamics in case 2, in which only ions interact directly with the LHW through the Landau damping. Fig. 3.6 shows the resulting contour plots of the electron phase-space distribution in case 2. The ion phase space evolution is shown in Fig. 3.6b, and the corresponding electron (black solid lines) and ion (red solid lines) distribution functions are depicted in Fig. 3.6c. Again, the ion velocities are normalized to the ion thermal speed.

Since electrons do not resonantly interact with the LHW, their velocity distribution is nearly unchanged. The phase-space structure of ion distribution, however, is significantly different from that of the electrons in the ELD. The vortex structure does not form in the ion phase space, as seen for $\Omega_i t = 0.11$ and 1.21, in Fig. 3.6b. The ions are weakly trapped (i.e., trapped in the ion gyro-period time scale, much longer than that of the LHWs), and the nonlinear effects are absent in their interactions with the LHW. As a result, the ions are continuously heated, as seen at $\Omega_i t = 4.40$. In Fig. 3.6c, the tail of the ion velocity distribution function expands due to the increase of the ion thermal speed.

3.4.3 case 3, Electron And Ion Landau Damping of LHWs

Wave profile in case 3

In case 3, $k_\parallel/k = 0.0404$, ion-to-electron temperature ratio $T_i/T_e = 4.0$, the initial perturbed electric field $E_0 = 0.1$, and the wave number $k\rho_e = 0.2255$. The real frequency in this case $\omega = 68.24\Omega_i = 2.05\omega_{LH}$. Thus, the electron resonance condition $\omega/(k_\parallel V_{te}) = 4.08$, and the ion resonance condition $\omega/(kV_{ti}) = 3.53$. Therefore, both electrons and ions can resonate with LHWs.

The time evolution of the spatial Fourier mode of the electric field in this case is plotted in Fig. 3.7. In case 3 with both the electron and ion Landau damping,

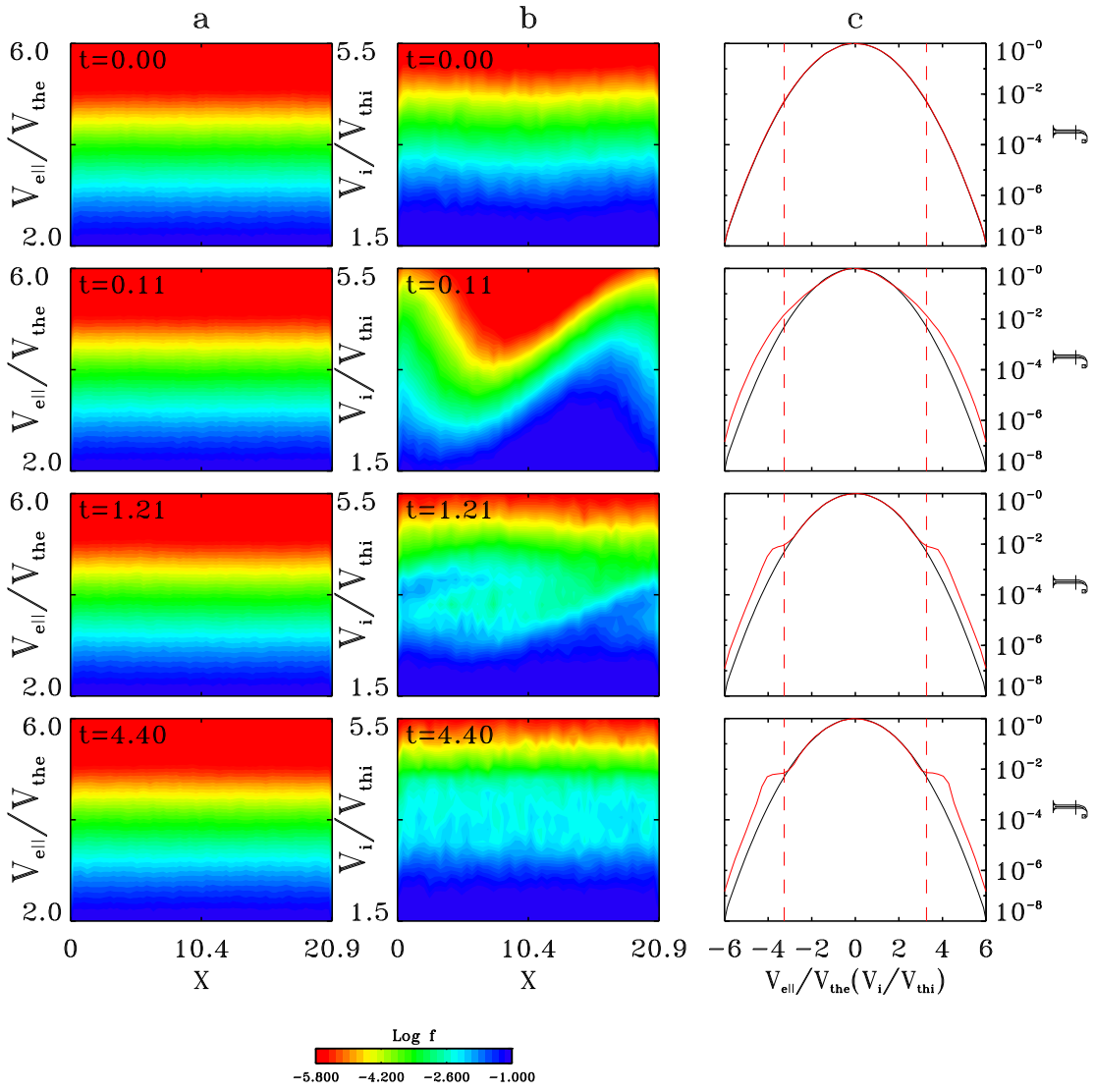

Figure 3.6: Time (normalized to $1/\Omega_i$) evolution of the electron phase-space distribution in case 2: contour plots of the (a) electron and (b) ion phase-space distributions and (c) the corresponding electron (black solid lines) and ion (red solid lines) distribution functions. The ion velocities are normalized to the ion thermal speed. The black (red) dash line shows the theoretical electron (ion) resonant phase-velocity $v_{ir} = 3.264V_{ti}$.

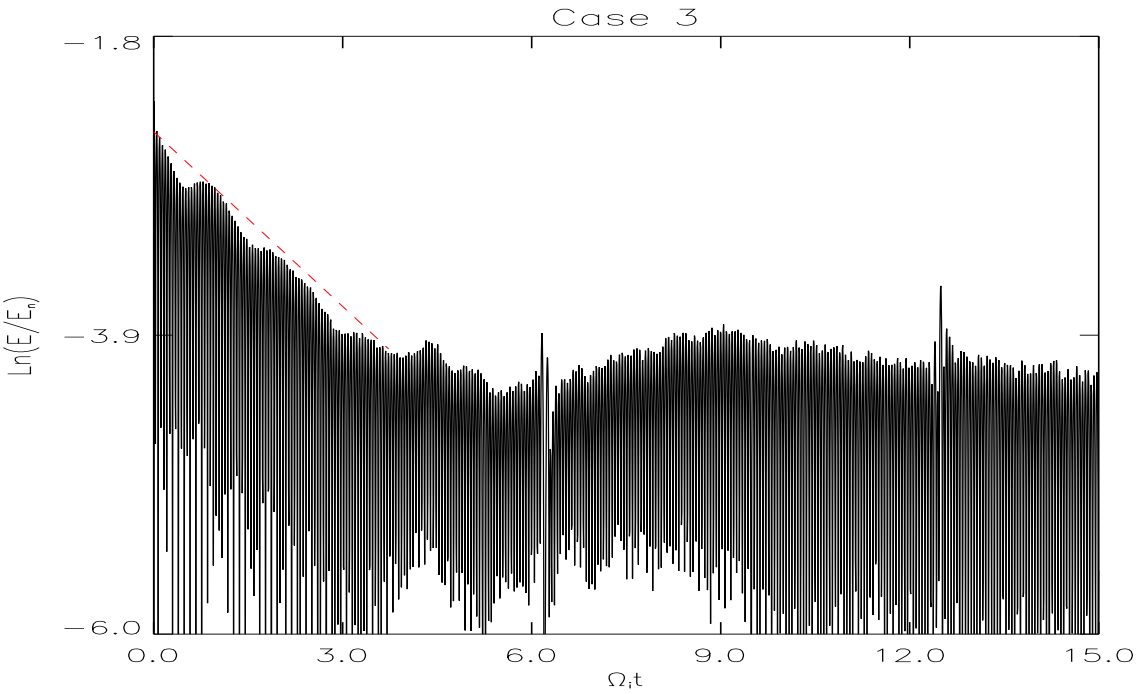

Figure 3.7: Time evolution of the spatial Fourier mode of the electric field (in the natural logarithm scale) for case 3 with $k_\parallel/k = 0.0404$, $T_i/T_e = 4.0$, $k\rho_e = 0.2255$, and $E_0 = 0.1$.

the overall reduction of the wave amplitude is dominated by the linear ion Landau damping, whereas the electron Landau effects are also seen in the envelop of the nonlinear oscillations from times $\Omega_i t = 0.0$ to 5.2, as seen in the figure. The wave saturation level is small, similar to that in case 2 shown in Fig. 3.5.

Particle motions in case 3

Fig. 3.8 shows the resulting electron and ion phase-space distributions in case 3 with the same format as Fig. 3.6. Indeed, in such case with both the electron and ion Landau damping, wave-particle resonance is found for both electrons and ions around the predicated phase velocities $v_{er} = 4.08V_{te}$ and $v_{ir} = 3.53V_{ti}$, respectively, as indicated by the vertical dashed lines in Fig. 3.8c. Correspondingly, plateaus are present in both electron and ion velocity distribution functions around the corresponding resonant phase velocities.

Although the phase-space structure of ions is similar to that of electrons at the early $\Omega_i t = 0.22$, the vortex structure does not form. The overall ion phase space contour plots (column b) show structures very similar to those in Fig. 3.6 for case 2. Again, the ion velocity distribution function curve expands tailward of the resonant velocity ($v_{ir}/V_{ti} = 3.53$), and ion heating is observed. For the electrons, the resulting structures are similar to those in Fig. 3.4 for case 1, except that the phase-space vortex structure becomes more ambiguous in the later time. The reason for this difference is that as the ions keep absorbing energy from the waves, the wave amplitude becomes smaller and smaller, and thus the trapping of electrons becomes weaker. The plateaus in the particle distributions, however, do not disappear eventually.

3.5 Nonlinear Damping Rates and Saturation of LHWs

According to the discussions above, when the initial perturbed electric field E_0 is small enough, the nonlinear effects of the ELD of LHWs are absent, and the waves will decay into the noise level linearly in logarithm. As E_0 gets larger, the nonlinear ELD effects will be involved. The wave will saturate in a BGK equilibrium, and the damping of the wave is weak, in the nonlinear ELD. Moreover, the ion Landau damping mainly goes through a linear damping in the resonance with LHWs. Because of these different characteristics of the electron or/and ion Landau damping for different initial perturbed electric field, it is interesting for us to research in the damping rate as a function of E_0 for different cases. Meanwhile, for different cases, the saturation levels of the electric field are quite different. Thus, the saturated electric field, E_s, is also of interest.

3.5.1 Landau damping rate of LHWs

By fixing $k\rho_e = 0.2255$ and $T_i/T_e = 1$, the damping rate, γ, as a function of the initial wave amplitude E_0 for various $k_\parallel/k$ is shown in Fig. 3.9. For $k_\parallel/k = 0.0904$,

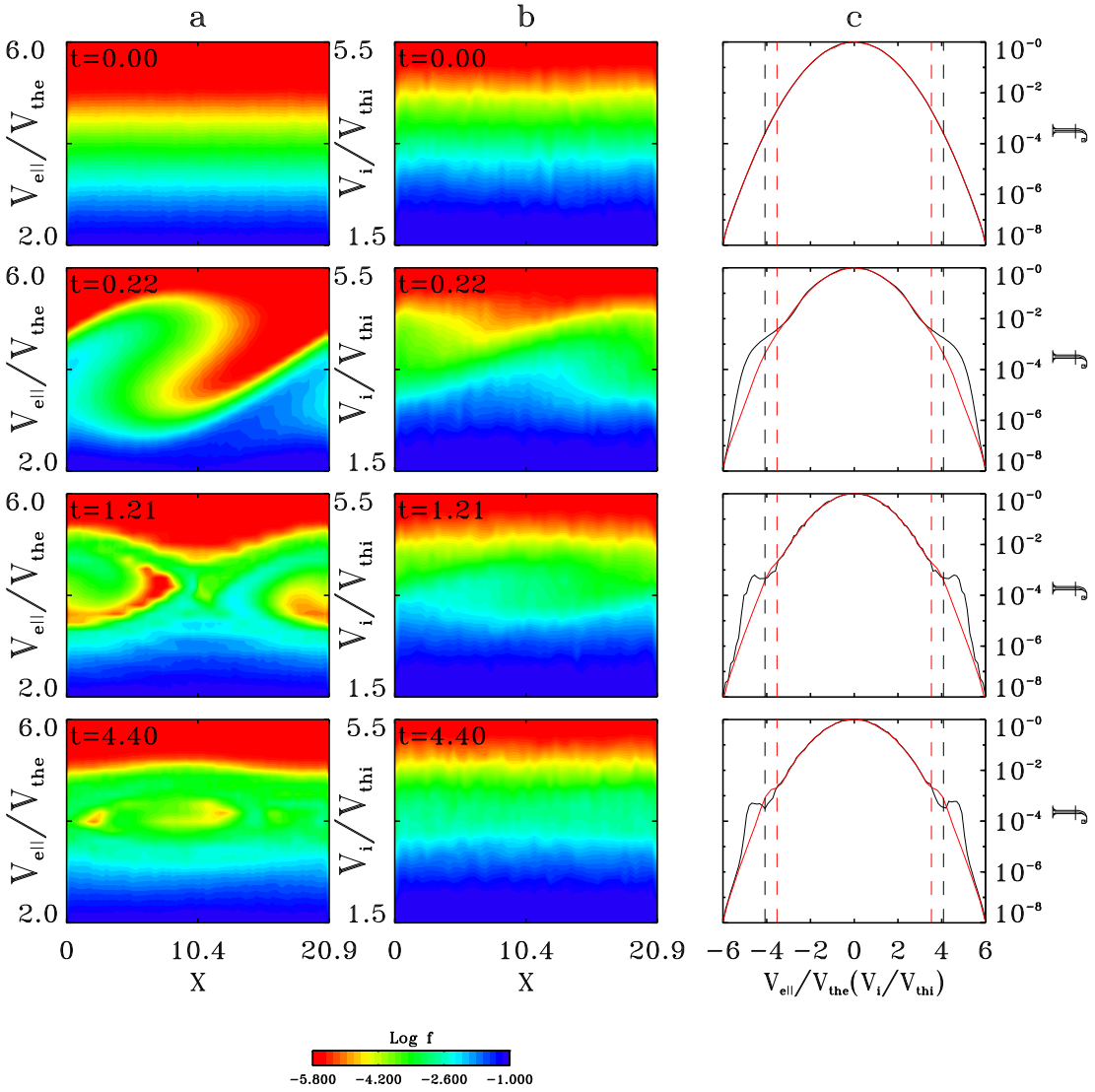

Figure 3.8: Resulting particle distributions obtained from case 3 in the same format as Fig. 3.6.

0.066, and 0.0404, all of which are similar to case 1 that only electrons are resonant with the LHW, there exists a transition from a strong decay at smaller amplitudes to a weak decay at larger amplitudes. In such cases, three distinct regimes are observed: (i) a small amplitude, fast damping regime, where only the linear Landau damping occurs; (ii) a nonlinear damping regime, in which the damping rate decreases as the amplitude increases, and (iii) a large amplitude, weak decay regime, where the damping rate saturates to be close to zero. The above results can be understood as the following. As the electric field becomes larger, the nonlinear effects of electron Landau damping becomes strong, which prevent the wave energy from decaying into the particles kinetic energy. The damping of the wave is therefore weaker.

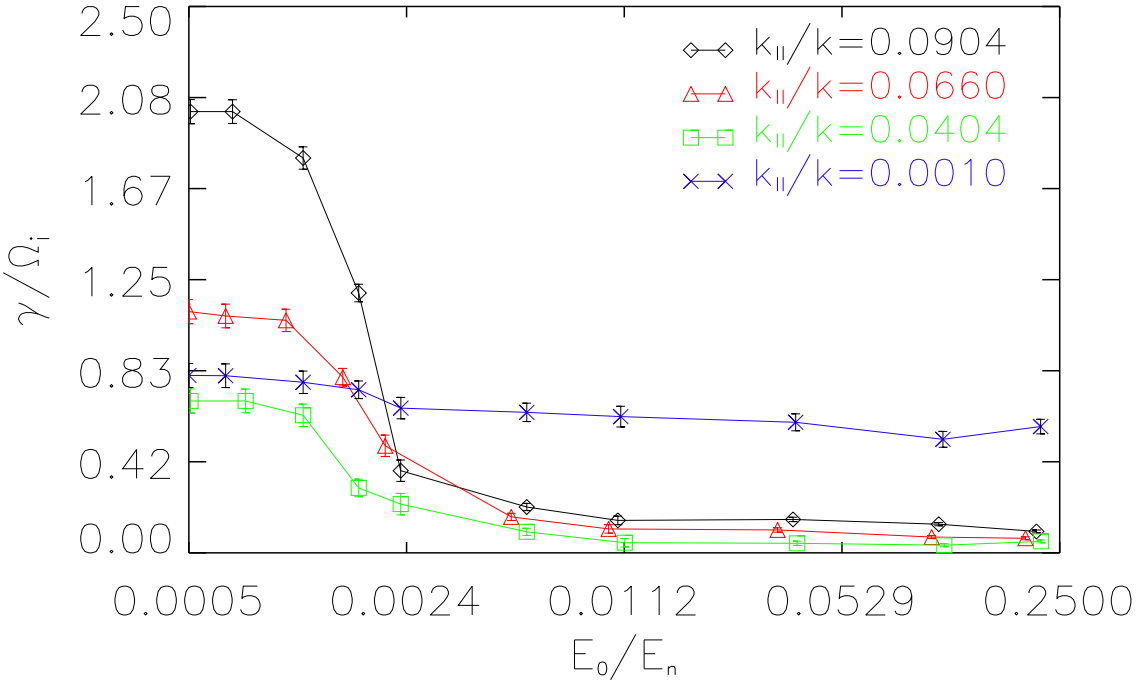

Figure 3.9: Damping rate, γ/Ω_i, as a function of the initial wave amplitude E_0 in the cases with $k\rho_e = 0.2255$ and $T_i/T_e = 1$, for $k_{||}/k = 0.0904$, 0.066, 0.0404, and 0.001.

On the other hand, for $k_{\|}/k = 0.001$, similar to case 2 with only ion Landau damping, the damping rate is found to change only slightly with the initial wave amplitude. The three distinct regimes are not clearly identified, and little nonlinear

Landau damping effects are observed. Note that the black dot for $E_0 = 0.1$ in Figure 3 corresponds to case 2.

Fig. 3.10 shows the damping rate vs. E_0 for $k\rho_e = 0.2255$ and $k_\parallel/k = 0.0404$, with $T_i/T_e = 4.0$, 1.0, and 0.33. The electron temperature (and thus the electron thermal speed) is fixed in all these cases, while the ion temperature varies with T_i/T_e. In the case with $T_i/T_e = 1.0$, most of the particles that are resonant with the LHWs are electrons, while few ions are involved in the resonant interaction. The resulting curve, therefore, shows a trend with the three distinct regimes. For $T_i/T_e = 0.33$, the ions are colder and thus possess a smaller thermal speed. As a result, there are almost no ions involved in the interaction. The damping rate γ in this case is nearly identical to that for $T_i/T_e = 1.0$.

For $T_i/T_e = 4.0$, similar to case 3 in which both the electrons and ions are resonant with the LHW, the damping rate decreases a bit as the initial amplitude E_0 increases, but never reaches a level near zero. These results, again, indicate that the nonlinear Landau damping effects are dominant in the ELD, whereas the ion Landau damping is of the linear characteristics. As T_i/T_e increases, the reduction of the wave amplitude becomes stronger due to the linear nature of the Landau damping as more ions participate in the wave-particle resonance.

3.5.2 Saturated Electric Field, E_s

Fig. 3.11 shows the saturation level of electric field, E_s/E_0, as a function of T_i/T_e for cases with an initial $E_0 = 0.1$ and $k_\parallel/k = 0.066$, 0.0404, and 0.001. The electron temperature is again fixed. In the cases with $k_\parallel/k = 0.066$, only electrons are resonant with the LHWs, with $\omega/(k_\parallel V_{te}) = 3.78$. The wave decay is dominated by the nonlinear ELD, and the wave saturation level is found to be nearly constant, at $E_s/E_0 \simeq 60\%$ within the plotted temperature range. In the cases with a decreased $k_\parallel/k = 0.0404$, the LHW frequency is also reduced, but the ratio $\omega/(k_\parallel V_{te})$ is increased to 4.08. When

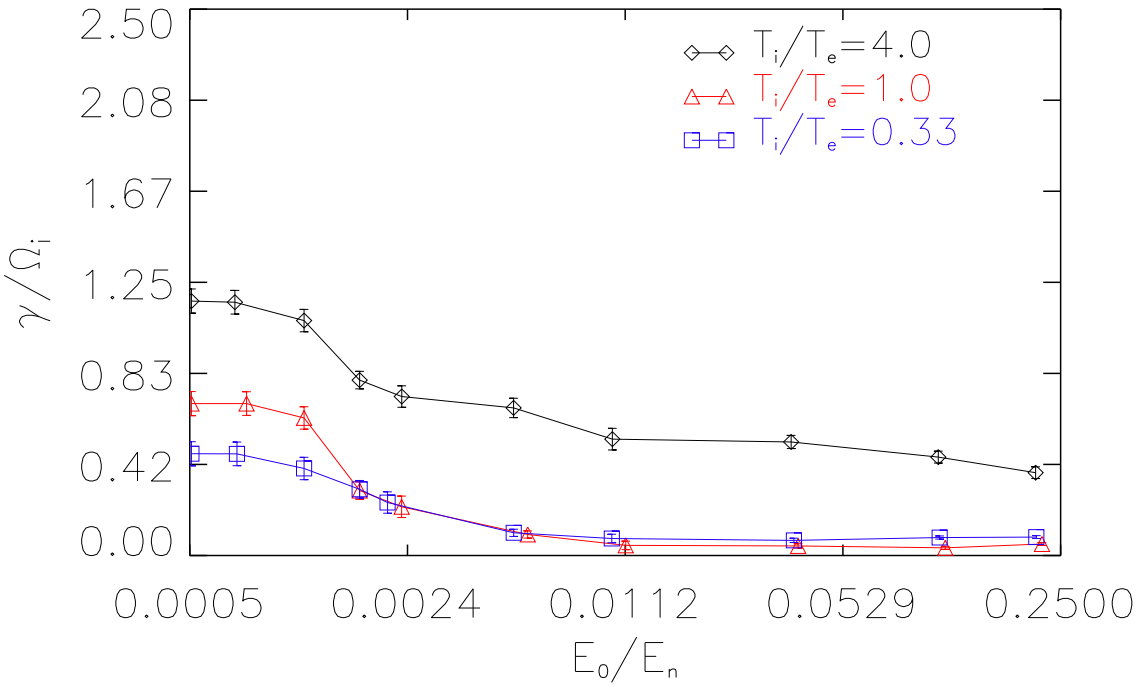

Figure 3.10: Damping rate vs. E_0 in the cases with $k\rho_e = 0.2255$ and $k_\parallel/k = 0.0404$, for $T_i/T_e = 4.0$, 1.0 and 0.33.

$T_i/T_e \leq 2.0$, only electrons are resonant with the waves. The saturation level E_s is again constant, but at a higher number of 75% due to the larger $\omega/(k_\parallel V_{te})$ and thus smaller portion of resonant particles. When $T_i/T_e > 2.0$, ions are also resonant with the waves, which leads to a decreased E_s because of the linear effects of the ion Landau damping. The saturation level E_s/E_0, however, is finite ($\simeq$ 15%), because of the contribution from the nonlinear Landau damping associated with electrons and trapped ions in the long time scales. In the cases with $k_\parallel/k = 0.001$, $\omega/(k_\parallel V_{te}) = 90$, and thus electrons cannot be resonant with the waves. When $T_i/T_e = 0.25$, $\omega/(kV_{ti}) = 7.7$, ions also cannot be resonant with the waves. The level E_s/E_0 is thus nearly 100% in the absence of both the electron and ion Landau damping. When $T_i/T_e > 0.25$, the ions resonance condition is satisfied. The saturation level E_s/E_0 decreases sharply to a very small number, near the noise level, due to the purely linear ion Landau damping effects.

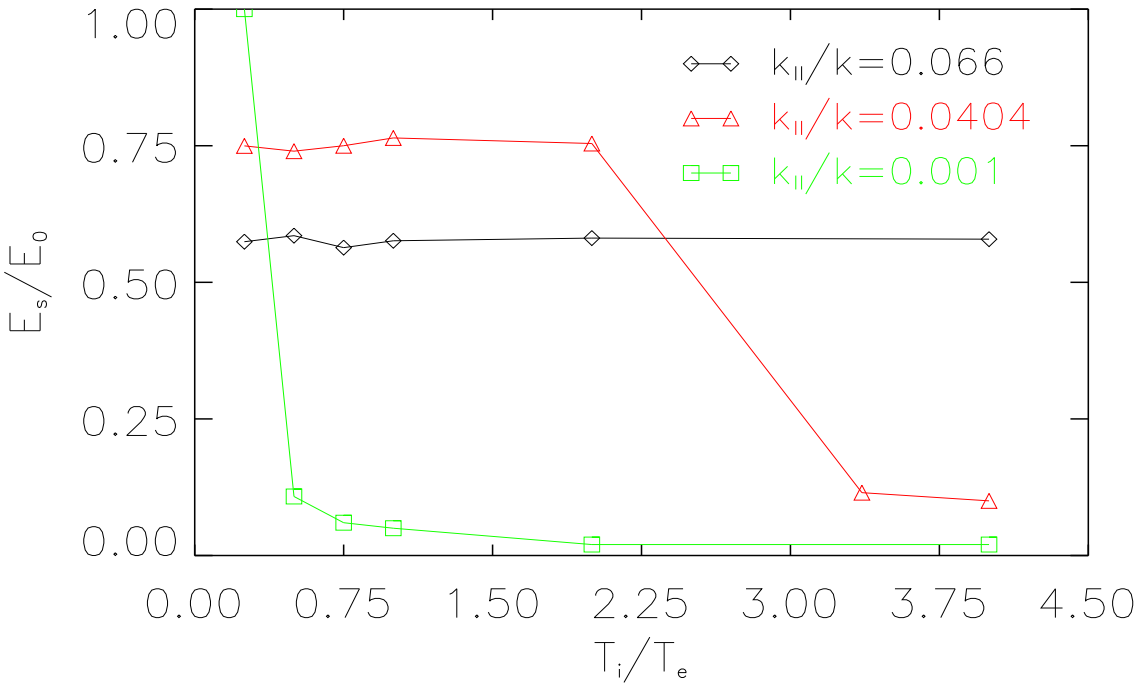

Figure 3.11: Saturated electric field E_s/E_0 vs. T_i/T_e in the cases with $k\rho_e = 0.2255$ and $k_\parallel/k = 0.066$, 0.0404,0.001

3.6 Calculation of Driven Current by LHWs

The lower hybrid waves can resonate with both electrons and ions through Landau damping mechanism, and thus are able to heat the particles and to generate electric currents in the plasmas. Momentum and energy can be exchanged between waves and particles obeying the resonance condition, $\omega - \mathbf{k}\cdot\mathbf{v}$, with ω being the frequency, $\mathbf{k}$ the wave vector and $\mathbf{v}$ the velocity of the particles. We will only consider the driven currents in the parallel direction to the magnetic field, thus the resonance condition is $\omega = k_\parallel v_\parallel$. In this section, we will first review the theory of current drive in collision plasmas[53, 50, 51, 52]. Then, the results of the driven currents from the Landau damping of LHWs from our GeFi simulations will be given. However, in our simulations, the problems are treated as initial value problems and the plasma is collisionless. Our results are the driven currents from the Landau damping of LHWs in the collisionless plasmas.

3.6.1 Fast Electrons Drive

The theory of driving fast electrons at the tail part of the velocity distribution function (fast electrons) will be discussed. Although it may be easier to push slow electrons, it may actually be more effective to push fast electrons. In practice, injecting waves with faster parallel phase velocities would be used to deposit momentum in faster resonant electrons. Although our simulations are in the collisionless plasmas, our discussions on the current drive here are in the plasmas with collisions in order to provide a complete concept of current drive.

The Coulomb collision cross section becomes smaller as relative speed between the colliding particles increases. Thus fast, superthermal electrons collide less often than slower, thermal electrons. This is because that the average relative speed between superthermal electrons and most other electrons and ions is much greater than the relative speed between thermal electrons and most other electrons and ions. In fact, the ratio of these speeds is roughly v/V_{te}, where v is the superthermal electron velocity. Although it may be energetically expensive to accelerate fast electrons in the first place, this energy deposition need to occur less often. But, the advantage is that currents lasts longer when carried by relatively less collisional electrons. The power requirements to sustain a given current against collisions can be small. Assume that the velocity $\mathbf{v}$ of an electron is randomized by collisions in a momentum destruction time of $1/\nu(v)$. An increment energy input $\Delta\varepsilon$ then produces an incremental current Δj that persists for time $1/\nu$. The parallel momentum absorbed by this electron is $m\Delta v_{\parallel}$; the incremental current carried by this electron is $\Delta j = q\Delta v_{\parallel}$; and the incremental increase in the electron kinetic energy is $\Delta\varepsilon = mv_{\parallel}\Delta v_{\parallel}$. Thus, we could find the following relationship

$$\Delta j = \Delta\varepsilon \frac{q}{mv_{\parallel}}. \tag{3.1}$$

The power requirement to refresh this current at time intervals of $1/\nu$ is

$$P_d = \nu \Delta\varepsilon. \tag{3.2}$$

Combining Eqs. 4.1 and 4.2 and assuming that the only current is the drive current, $J = \Delta j$, we have the steady-state efficiency

$$\frac{J}{P_d} = \frac{q}{m v_\parallel \nu(v)}. \tag{3.3}$$

Apparently, the efficiency (current per power dissipated) is maximized when the expression $v_\parallel \nu(v)$ is minimized. It is usually identified by Fisch for the utilization of lower hybrid wave in the limit, $v_\parallel \gg V_{te}$. In this limit, a high efficiency can be acquired, since $J/P_d \sim v_\parallel^2$, with $v_\parallel$ being large.

To illustrate the effect on the electron distribution function f caused by the injection of high phase velocity waves, we present the results of a numerical calculation of our electron Landau damping study of LHWs in Fig. 4.1, which is the plot of parallel velocity distribution as a function of the parallel velocity (v_par is $v_\parallel/V_{te}$). It is seen in the figure that the plateau (solid line) deviates from the initial distribution (dashed line). In the current drive problems, the injected waves propagate in only one direction, thus this plateau will exist in only one side of the velocity distribution function. This deviation in the distribution forms in the resonant region. Due to the plateau, the distribution function is asymmetric, indicating the presence of current. The asymmetry, it turns out, is large enough to signify very large currents.

3.6.2 Electric Currents obtained from GeFi Simulation of LHWs

Lower hybrid wave is a preferable source to generate currents in lots of plasma devices, i.e., Tokamak. As it can be seen in the GeFi simulation results discussed in Chapter 3, the parallel velocity distribution function is deviated from the initial

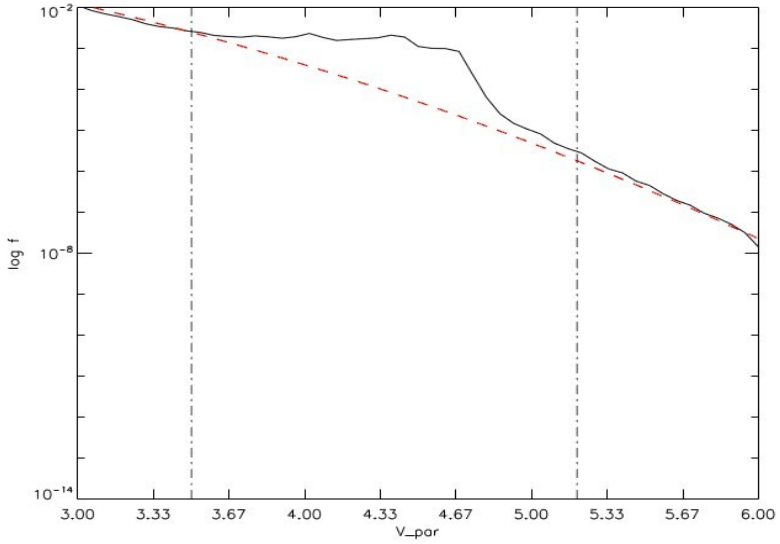

Figure 3.12: The plateau in the parallel velocity distribution function in the electron Landau damping of LHWs (V_par is the parallel velocity, $v_{\parallel}$, normalized in V_{te})

Maxwellian distribution in the electron Landau damping of LHWs. Although our studies are in the collisionless plasmas, we can still calculate the generated current due to the deviation of the distribution. However, there is not the dissipation or current drive efficiency concepts in our study.

In our simulation, the waves are allowed to propagate in both the positive and negative directions symmetrically, and thus the wave-particle interaction occurs in both directions. The deviated distribution function, therefore, is nearly symmetric. In the lower-hybrid drive in fusion plasmas, however, the waves will propagate only in one direction. The plateau will only exist in one side of the distribution, which is thus asymmetric. And the asymmetric deviation in the distribution $f(v_{e\parallel})$ can generate net parallel current. Here, we estimate the electron parallel current $J_{\parallel}$ generated in the $v_{e\parallel}$ direction.

Let $f = f_m + \widetilde{f}$, where $f_m = 1/(\sqrt{2\pi}V_{te})\exp[-v_\parallel^2/(2V_{te}^2)]$ is the background parallel Maxwellian distribution function and $\widetilde{f}$ is the deviation of the distribution function from the Maxwellian one. Fig. 4.1 shows us one of the typical deviated distribution functions in our simulations. The current can be calculated as

$$J_\parallel = -\int ev_\parallel \widetilde{f}(v_\parallel)dv_\parallel. \tag{3.4}$$

Since only the plateau (resonance region) of the deviated distribution function contributes to the current, our calculation of $J_\parallel$ is only for the plateau region.

We perform again a simulation using the parameters in case 1, which is introduced in the last chapter. In this new run we obtain the electrons' velocities and parallel velocity distribution information to calculate the parallel current by Eq. 4.18. Fig. 4.2 shows the time evolution of $J_\parallel$ obtained in case 1, in which only electrons are resonant with the wave. Here, the current is normalized to en_0V_{te}, and the time is expressed in units of $1/\Omega_i$. It is seen that the current reaches a maximum value within a few wave periods and then keeps oscillating, due to the oscillating wave-particle energies in the nonlinear ELD.

In order to examine the effects of the wave amplitude on the generation of the currents, Fig. 4.3 presents the resulting $J_\parallel$ in the logarithmic scale as a function of the initial wave amplitude E_0. The three curves correspond to $k_\parallel/k = 0.066$ and $T_i/T_e = 1.0$, $k_\parallel/k = 0.0404$ and $T_i/T_e = 4.0$, and $k_\parallel/k = 0.0404$ and $T_i/T_e = 1.0$, respectively. In all these cases, $k\rho_e = 0.2255$. And all the other parameters remain the same as that given in last chapter, section 3.1. The currents are calculated at later times when the final BGK state is reached. For $k_\parallel/k = 0.0404$ and $T_i/T_e = 4.0$, although the linear ion Landau damping is dominant on top of the ELD, the driven currents show a trend that is similar to that for $k_\parallel/k = 0.066$ and $T_i/T_e = 1.0$ with ELD only. For all three curves in Fig. 10, the current grows very fast at smaller

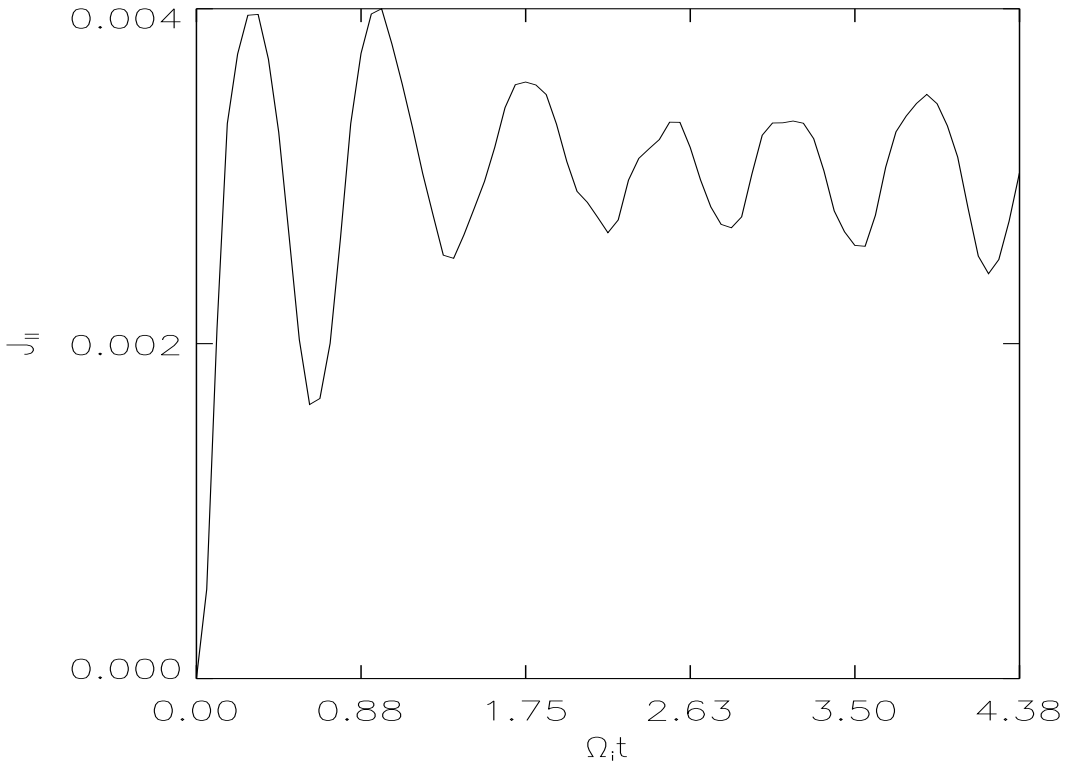

Figure 3.13: Time evolution of $J_\parallel$ (normalized to en_0V_{te}) obtained from case 1.

E_0. The growth then slows down as E_0 increases. The reason is that when the wave amplitude is small enough, the linear ELD is dominant, and most of the wave energy is converted to the particle energy. When E_0 is large, the nonlinear ELD effects limit the decay of the wave energy into the particles kinetic energy, and Thus the growth of the current slows down. For $k_\parallel/k = 0.066$ and $T_i/T_e = 1.0$, and $k_\parallel/k = 0.0404$ and $T_i/T_e = 1.0$, both dominant with ELD, larger amplitudes of currents are generated by larger ratio of $k_\parallel/k$ (or a larger ω). For the two curves corresponding to the same ratio of $k_\parallel/k$, the one with a larger temperature ratio T_i/T_e possesses ion Landau damping. The ion Landau damping leads to smaller saturated wave amplitudes, and thus generates smaller steady-state currents in the electron-wave particle interaction.

Note that the plasmas here are collisionless, and we are unable to calculate the energy dissipation and the current drive efficiency. It is aimed to research the electron Landau damping of LHWs in collisionless plasmas in this thesis. It is seen that there

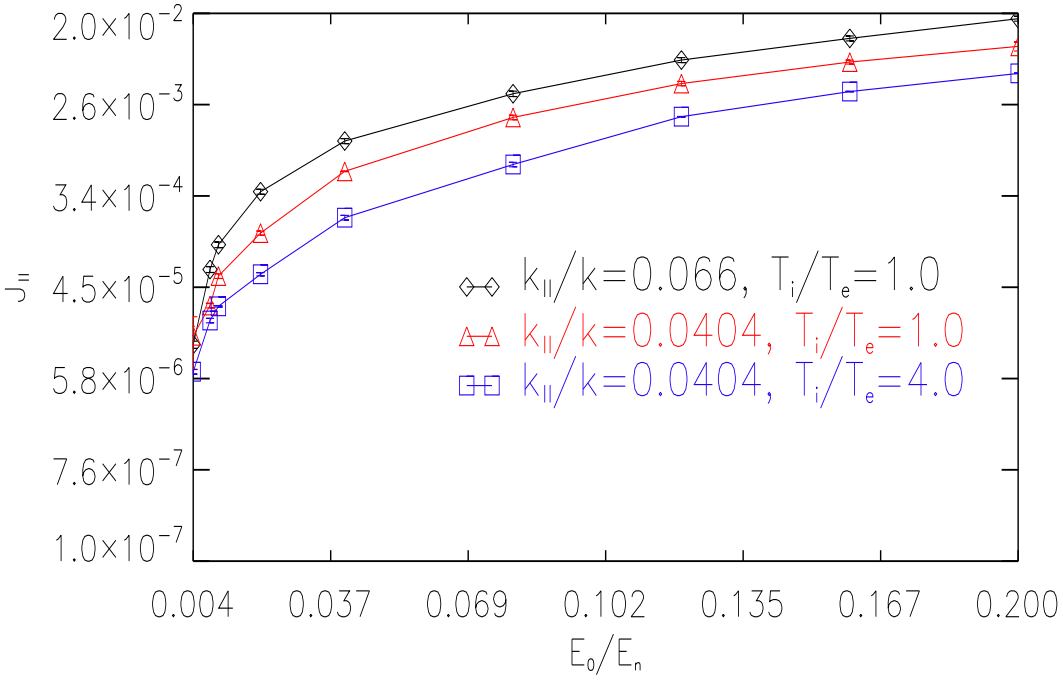

Figure 3.14: Resulting parallel currents as a function of the initial LHW amplitude E_0.

is very close relations between the nonlinear electron Landau damping effects with the current generations. Moreover, the ions' Landau damping can play important role in the Landau damping of LHWs and thus affect the current drive mechanisms. Further work can about the current drive issue by LHWs be done if we can put the collisions in the plasmas and do current drive problems with consistent perturbing LHWs.

3.7 Ions Phase Bunching

In either fig. 3.6 or fig. 3.7, it can be seen that the wave amplitude shows a sudden jump, followed by a sudden damping, at time intervals of $\Delta t \simeq 2\pi/\Omega_i$, which is equal to the ion gyromotion period. The sudden jump and damp is relevant to ions gyromotion, ions phase bunching in the velocity phase space and ions distribution at low velocities.

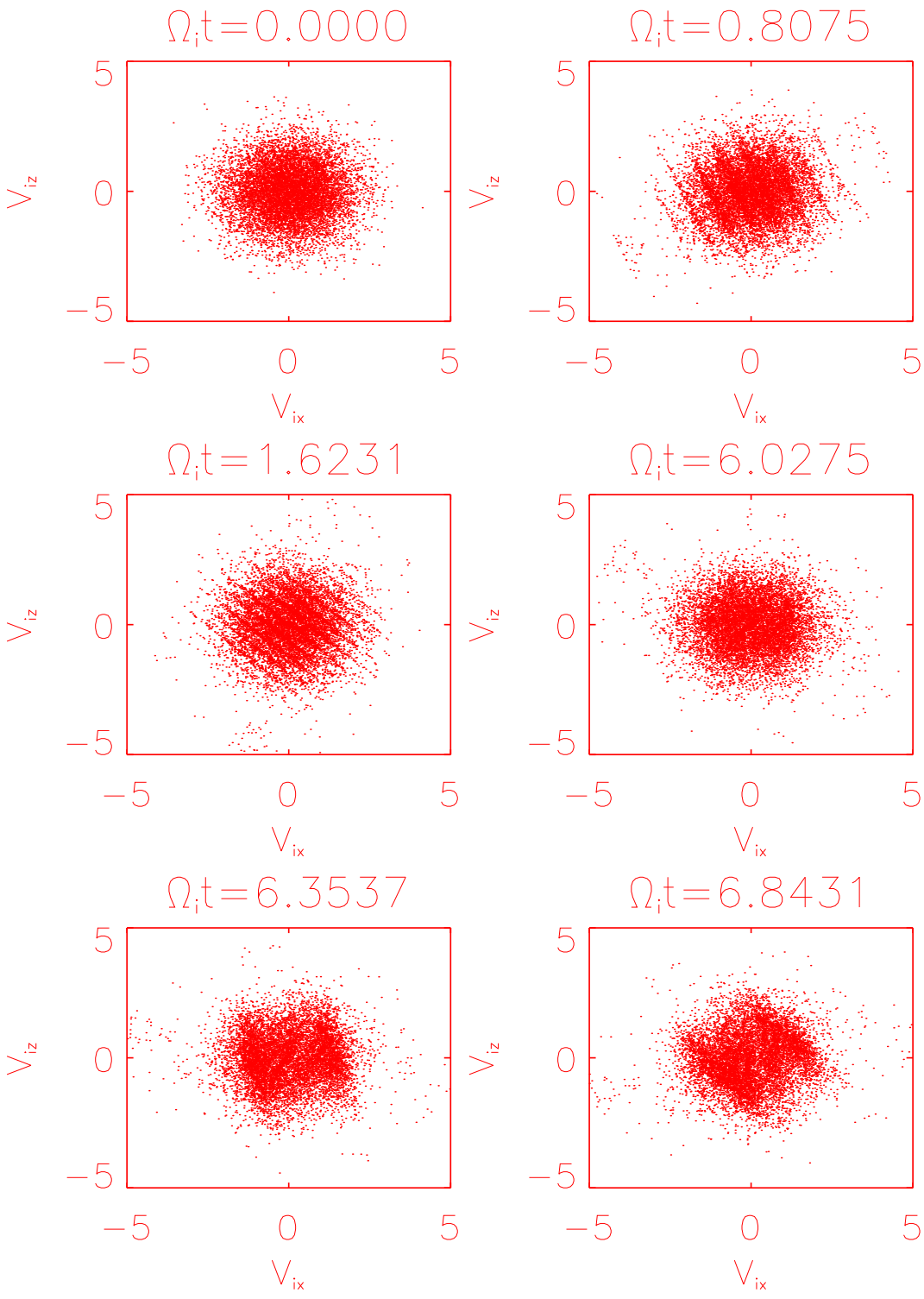

Figure 3.15: Scatter plots of ions distribution for selected particles in velocity phase space (V_{ix}, V_{iz}) at $\Omega_i t = 0.0$, 0.8075, 1.6231, 6.0275, 6.3537, 6.8431.

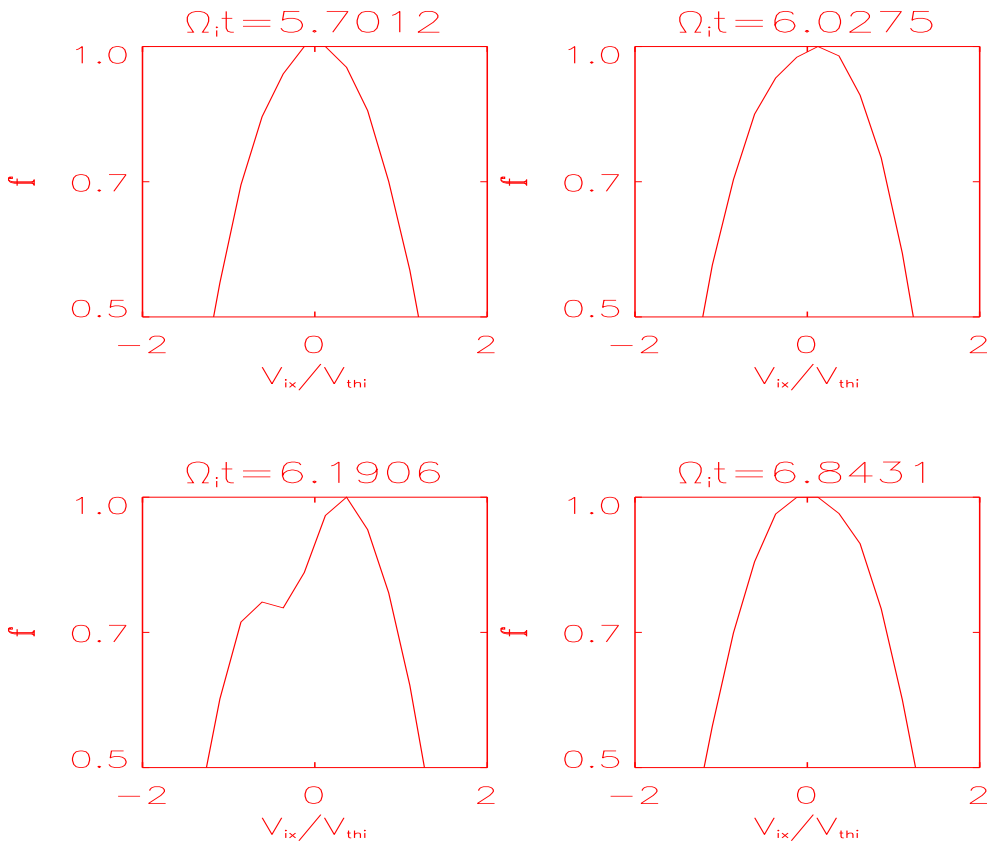

Figure 3.16: Ions velocity distribution function in terms of V_{ix} at $\Omega_i t = 5.7012$, 6.0275, 6.1906, 6.8431.

Figure 3.15 is scatter plots of ions distribution for a group of ions randomly selected at the beginning of simulation in velocity phase space (V_{ix}, V_{iz}) at $\Omega_i t = 0.0$, 0.8075, 1.6231, 6.0275, 6.3537, 6.8431. It can be seen from the figure that the ions are uniformly distributed in the phase space at $\Omega_i t = 0.0$. At $\Omega_i t = 0.8075$ and $\Omega_i t = 1.6231$, when the wave is damping, ions are highly bunched at a few regions in the phase space. At $\Omega_i t = 6.0275$, when the amplitude of the wave is small and just before the sudden jump, ions become uniformly distributed again. During the sudden jump $\Omega_i t = 6.3537$ and after the judden jump $\Omega_i t = 6.8431$, ions are highly bunched again at two major regions. Some small bunching structures can also be observed in those two plots.

Figure 3.16 shows plots of the ion velocity distribution function in terms of V_{ix} at $\Omega_i t = 5.7012$, 6.0275, 6.1906, 6.8431. From the figure, evolution of the ion velocity distribution function from a time before the sudden jump to a time after the sudden jump can be seen. Initialy at $\Omega_i t = 5.7012$, which is before the sudden jump, the distribution function is Maxwellian. From plots at $\Omega_i t = 6.0275$ and $\Omega_i t = 6.1906$, both of which are during the sudden jump, it is seen that the distribution function gradually changes. The number of ions at low positive velocities increases, while the number of ions at low negative velocities decreases. At $\Omega_i t = 6.8431$, which is after the sudden jump, the distribution recovers to Maxwellian.

3.8 Summary

In this chapter, Simulation results of Landau damping of LHWs from the novel Gyrokinetic electron and Fully kinetic ion (GeFi) code model are presented, including linear and nonlinear propagations of LHWs and calculations of driven electric current in the process. The main conclusions are summarized in the following.

(1) From the simulations of the linear electron Landau damping of LHWs, it is seen the waves decay into the noise level linearly in logarithm. Both the real frequency and the linear electron Landau damping rate from the simulations show excellent agreement with that from the analytical theory of electron Landau damping of LHWs.

(2) Both electrons and ions can resonantly interact with the LHWs. The electrons are magnetized, and their resonance condition follows $\omega = k_{\|} v_{e\|}$. On the other hand, the ions are highly unmagnetized in the magnetic field of LHWs, and their resonance condition is determined by $\omega = \mathbf{k} \cdot \mathbf{v_i}$.

(3) Trapped electrons are observed correspondingly in the nonlinear electron Landau damping, as predicated by the nonlinear theory. In the long time nonlinear

evolution of the LHWs associated with the electron Landau damping, the amplitude of the wave becomes oscillatory asymptotically, reaching a final BGK equilibrium.

(4) The ion Landau damping, on the other hand, is dominated by the linear physics in the LHW time scales, with nearly no trapped ions in the wave-particle interaction. In the case with solely ion resonance or the case in which there exist both the ion and the electron resonance, the wave amplitude is significantly reduced by the ion Landau damping. On the long time scales, however, the ions are still weakly trapped. Behaviors of magnetized ions appear, with a frequency $\sim \Omega_i$.

(5) As the initial wave amplitude increases, a transition occurs in the electron Landau damping from a strong linear decay of LHWs to a weak decay, which is dominated by the nonlinear physics.

(6) Generation of the parallel currents through the ELD from our GeFi simulations is discussed. While the presence of the ion Landau damping results in a smaller $J_{\|}$ than that with solely electron Landau damping, similar trends are observed in the dependence of the currents on the initial wave amplitudes for cases with or without the ion Landau damping. The current increases quickly with the initial wave amplitude when the amplitude is small, but slows down when the initial wave amplitude is large.

Chapter 4

GeFi Simulation of Electron-ion Hybrid instability

Kinetic simulation investigation of an instability in a magnetized plasma with a localized electron cross-field flow is performed by utilizing GeFi model.

4.1 Introduction

Study of the dynamics that governs the release of free energy associated with sheared flows was given considerable attention in both hydrodynamics[56, 57] and plasma physics[58, 59], since macroscopic flows are commonly encountered in various plasmas, such as plasmas in tokamak devices, Earth's magnetotail, plasma sheet boundary layer, laser-produced plasmas, and Earth's magnetopause. The shear-driven instabilities have significant effects on particles, momentum, and energy transport. For instance, in tokamak devices, the transition from a low (L) mode to a high (H) mode of energy and particle confinement is thought to be excited by the sheared poloidal flows[60, 61]. In the Earth's magnetopause and plasma sheet boundary layer, variety of wave activities, that are responsible for the broadband electrostatic noise observed by satellites, are associated with the induced sheared electron cross-field flow due to the presence of steep density gradients[62, 68]. In a word, the instabilities excited by the sheared flow play important roles in the wealth of physics activities.

The sheared flows can excite different instabilities given different conditions, such as the low frequency and long wavelength Kelvin-Helmholtz (KH) modes[69]. KH mode can be sustained by a transverse velocity shear for $L > \rho_i$, where L is the velocity shear scale length and ρ_i is the ion gyroradius. Electron-ion Hybrid (EIH) instability[70, 71] is another shear-driven instability that can be sustained by

the velocity shear $\rho_e < L \ll \rho_i$ with ρ_e being the electron gyroradius. Different from Kelvin_Helmholtz mode, EIH instability is a short wavelength ($k_y\rho_i \gg 1$ but $k_y\rho_e \ll 1$) and high frequency ($\omega_r \sim \omega_{LH}$, where ω_{LH} is the lower hybrid frequency) mode.

The linear theory of EIH instability is reviewed in the first place in slab geometry in uniform plasmas and nonuniform plasmas with $k_zL = 0$, and uniform plasmas with a finite $k_z \neq 0$. Here in the slab geometry, static magnetic field is at z axis, and electron shear flow as a function of x is put at y axis. GeFi kinetic simulations are then performed in slab geometry and cylindrical geometry with either uniform plasmas or nonuniform plasmas, with $k_zL = 0$ and $k_zL \neq 0$. In the cylindrical geometry, static magnetic field is also at z direction, while electron shear flow as a function of radial position r is in θ (poloidal) direction. Results are compared with the linear theory in a slab geometry. Realistic experimental parameters in Auburn Linear EXperiment for Instability Studies (ALEXIS) device are adopted in the linear GeFi kinetic simulations, and the results are compared with the experiments as well. Nonlinear GeFi kinetic simulations in a slab geometry and uniform plasmas are also studied, and show that the EIH instability mode finally evolves from a short wave length ($k_x\rho_i \sim 12$) mode to a long wave length ($k_x\rho_i \sim 3$) mode with frequency $\sim \omega_{LH}$ in the nonlinear stage.

4.2 Linear theory of EIH instability

Linear theories of EIH instability in magnetized plasmas in slab geometry with a sheared electron flow channel are reviewed in this section, including general physical model, dispersion equations in uniform plasmas and nonuniform plasmas with $k_zL = 0$, and unifrom plasmas with $k_zL \neq 0$, and numerical methods for solving the dispersion equations (shooting code method).

4.2.1 General physical model

Consider a schematic configuration, which consists a magnetized plasma slab in which a localized electric field is present.[70] The external static magnetic field is chosen to be directed along z axis and the electric field is in x direction, that is,

$$\begin{aligned} \mathbf{B}_0 &= B_0(x)\mathbf{e}_z, \\ \mathbf{E}_0 &= E_0(x)\mathbf{e}_x, \end{aligned} \tag{4.1}$$

where $\mathbf{e}_x$ and $\mathbf{e}_z$ are the unit vectors in x and z directions, respectively. The amplitude of the electric field $E_0(x)$ is assumed to be localized over a region with a width L, which satisfies $\rho_e < L \ll \rho_i$. This configuration would result in a $\mathbf{E}_0 \times \mathbf{B}_0$ flow velocity in the y direction, whose spatial extent is smaller than ρ_i. As it is seen, all the physical quantities vary only along the x axis. Electron and ion densities can vary spatially in the whole region of interest, with their scales of variation to be chosen of the same order of magnitude as that of the electron $\mathbf{E}_0 \times \mathbf{B}_0$ flow.

In the case of perpendicular (to static magnetic field) flows, an unstable mode develops whose frequency and growth rate are on the order of lower hybrid wave frequency, ω_{LH} when $k_\parallel = 0$. The perpendicular wave length of the instability mode is assumed to be much larger than electron Larmor radius, i.e., $k_\perp \rho_e \ll 1$. In this limit, the fluid description consisting of mass conservation and momentum balance equations can be adopted. Ions can be assumed to be unmagnetized, since the frequency and growth rate of the instability mode are larger than ion cyclotron frequency, Ω_i. To consider an instability mode with frequency on the order of ω_{LH}, cold fluid plasma approximation can also be used to determine ion responses. Perpendicular wave number is also assumed $k_\perp \rho_i \gg 1$.

The fluid equations are linearized according to the following normal mode representation for the plasma density N_α and flow velocity $\mathbf{U}_\alpha$:

$$\begin{aligned} N_\alpha &= n_\alpha(x) + \widehat{n}_\alpha(x)\exp[-i(\omega t - k_y y - k_\parallel z)], \\ \mathbf{U}_\alpha &= \mathbf{V}_\alpha(x) + \mathbf{v}_\alpha(x)\exp[-i(\omega t - k_y y - k_\parallel z)], \end{aligned} \tag{4.2}$$

where k_y is the wave number along the y axis, and ω is the complex angular frequency of the instability mode. $n_\alpha(x)$ is the equilibrium plasma density, and $\mathbf{V}_\alpha(x)$ denote the equilibrium sheared flow velocity. $\alpha = i,\ e$ denotes the species of the particles. $\widehat{n}_\alpha(x)$ and $\mathbf{v}_\alpha(x)$ are the density and velocity modifications due to the perturbation in the system. To be specific, the equilibrium flow velocity is chosen as follows:

$$\mathbf{V}_\alpha(x) = V_E(x)\mathbf{e}_y + V_{d\alpha}(x)\mathbf{e}_z. \tag{4.3}$$

Where $\mathbf{e}_y$ is the unit vector in the y direction; $V_{d\alpha}(x)$ represents the flow velocity parallel to the equilibrium magnetic field for species α; and $V_E(x)$ denotes the amplitude of the $\mathbf{E}_0 \times \mathbf{B}_0$ flow velocity:

$$V_E(x) = -\frac{cE_0(x)}{B_0(x)}. \tag{4.4}$$

Assuming the mode is electrostatic, we can obtain the electric field

$$\mathbf{E} = E_0(x)\mathbf{e}_x - \nabla\{\phi(x,\omega)\exp[-i(\omega t - k_y y - k_\parallel z)]\}, \tag{4.5}$$

where $\phi(x,\omega)$ is the complex electrostatic potential.

From the Poisson's equation, one can obtain the equilibrium electron density n_e in terms of the equilibrium ion density n_i and the equilibrium electric field:

$$en_e(x) = \sum_i Z_i e n_i(x) - \frac{1}{4\pi}\frac{dE_0(x)}{dx}. \tag{4.6}$$

Here, Z_i is the charge number of ions.

The perturbed flow velocity $\mathbf{v}_\alpha(x)$ in terms of the electrostatic potential $\phi(x,\omega)$ can be expressed in the following.

$$\begin{aligned}
v_{\alpha x} &= -(\frac{iq_\alpha}{m_\alpha D_\alpha})(\Delta_\alpha \frac{d\phi(x,\omega)}{dx} - k_y \Omega_\alpha(x)\phi(x,\omega)), &(4.7)\\
v_{\alpha y} &= -(\frac{q_\alpha}{m_\alpha D_\alpha})(\eta_\alpha(x)\Omega_\alpha(x)\frac{d\phi(x,\omega)}{dx} - k_y \Delta_\alpha \phi(x,\omega)), &(4.8)\\
v_{\alpha z} &= (\frac{q_\alpha}{m_\alpha \Delta_\alpha})k_\parallel \phi(x,\omega) - (\frac{iV'_{d\alpha}}{\Delta_\alpha})v_{\alpha x}, &(4.9)
\end{aligned}$$

where $\Omega_\alpha(x)$ denotes the cyclotron frequency of species $\alpha = i,\ e$. The quantities Δ_α, D_α, and $\eta_\alpha(x)$ are obtained by the following expressions.

$$\begin{aligned}
\Delta_\alpha(x,\omega) &= \omega - k_y V_E(x) - k_\parallel V_{d\alpha}(x),\\
D_\alpha(x,\omega) &= \Delta_\alpha^2(x,\omega) - \eta_\alpha(x)\Omega_\alpha^2(x),\\
\eta_\alpha(x) &= 1 + \frac{V'_E(x)}{\Omega_\alpha(x)}. &(4.10)
\end{aligned}$$

The perturbed plasma density $\widehat{n}_\alpha(x)$ can be found from the mass conservation equation, in terms of the particle velocities:

$$i\Delta_\alpha \widehat{n}_\alpha(x) = \frac{d}{dx}[n_\alpha(x)v_{\alpha x}] + in_\alpha(x)(k_y v_{\alpha y} + k_\parallel v_{\alpha z}). \tag{4.11}$$

By linearizing the Poisson's equation there results in the differential dispersion equation for the instability mode.

$$\frac{d}{dx}(A(x,\omega)\frac{d\phi(x,\omega)}{dx}) - q(x,\omega)\phi(x,\omega) = 0, \tag{4.12}$$

where

$$\begin{aligned}
q(x,\omega) &= k_y^2 B(x,\omega) + k_\parallel^2 C(x,\omega) - k_y \frac{dE(x,\omega)}{dx}, \\
A(x,\omega) &= 1 - \sum_\alpha \frac{\omega_{p\alpha}^2(x)}{D_\alpha(x,\omega)}, \\
B(x,\omega) &= 1 - \sum_\alpha \frac{\omega_{p\alpha}^2(x)}{D_\alpha(x,\omega)}(1 - \frac{\Omega_\alpha(x)V_E'(x)}{\Delta_\alpha^2(x,\omega)}), \\
C(x,\omega) &= 1 - \sum_\alpha \frac{\omega_{p\alpha}^2(x)}{\Delta_\alpha^2(x,\omega)}, \\
E(x,\omega) &= \sum_\alpha \frac{\omega_{p\alpha}^2(x)\Omega_\alpha(x)}{D_\alpha(x,\omega)\Delta_\alpha(x,\omega)},
\end{aligned} \tag{4.13}$$

and $\omega_{p\alpha}(x)$ denotes the plasma frequency of species α. To assume that the ions are unmagnetized, we can take the limit that $\Omega_i = 0$ when evaluating Eq. 4.13.

Eq. 4.12 is the wave differential dispersion equation in a general form. We will simplify this equation in the uniform plasma assuming that the ions are stationary in all of our simplifications in the next sections.

Since there is a localized electric field with a shear scale length $L > \rho_e$, the electron velocity distribution needs to be modified. The electric field causes a cross-field electron flow in the y direction. And because the electric field is nonuniform in x direction, the distribution function deviates from being a simple drifting Maxwellian[71]. Expand the distribution function in terms of the small parameter ρ_e/L leads to the following expression

$$F_e = \frac{n_e(X_g)}{\sqrt{\eta(x)}(\pi V_{te})^{3/2}} \exp\left(-\frac{w_\perp^2 + v_z^2}{V_{te}^2}\right), \tag{4.14}$$

where $w_\perp^2 = v_x^2 + w_y^2/\eta(x)$, $w_y = v_y - V_E(x)$, $V_E(x) = -E(x)/B_0$ is the sheared electron cross-flow, $X_g = x + v_y/\Omega_e$ is the guiding center, V_{te} is the electron thermal speed, and $\eta(x) = 1 + V_E'/\Omega_e$. This expression is valid up to the second order of ρ_e/L. The electron density is determined from the quasineutrality condition $n_e(x) = n_i(x) - (1/e)E'$, where e is the electron charge.

4.2.2 EIH instability dispersion equations

The governing wave equation Eq. 4.12 introduced in the last section can be simplified in a uniform density plasma, given that the ions are stationary, the parallel wave number $k_\parallel \sim 0$, and the electron flow is weakly sheared, i.e., that $V_E'/\Omega_e \ll 1$.

To consider the linear dispersion relation for electrostatic potential $\phi(x)$ of lower hybrid waves, and assuming a flutelike perturbation, Eq. 4.12 can be expressed approximately in the following:[71]

$$\frac{d}{dx}[A(x)\frac{d\phi(x)}{dx}] - k_y^2 A(x)\phi(x) = \delta^2(\frac{k_y\Omega_e}{\omega - k_y V_E})S_e\phi(x), \tag{4.15}$$

where ω is the complex angular frequency of the mode and k_y is the wave number in the y direction.

$$\begin{aligned} A(x) &= (1+\delta^2)(1-\omega_{LH}^2/\omega^2), \\ S_e &= (\ln n_e)' - V_E''/\Omega_e, \end{aligned} \tag{4.16}$$

with $\delta = \omega_{pe}/\Omega_e$ and $\omega_{LH}^2 = \omega_{pi}^2\Omega_e^2/(\omega_{pe}^2 + \Omega_e^2)$.

For the instability mode in the uniform plasmas, Eq. 4.15 can then be simplified:[69]

$$(\frac{d^2}{dx^2} - k_y^2 + F(\omega)\frac{k_y V_E''(x)}{\omega - k_y V_E(x)})\phi(x) = 0, \tag{4.17}$$

where $F(\omega) = \delta^2/\{(1+\delta^2)[1-(\omega_{LH}/\omega)^2]\}$. As it is seen from this equation, the second derivative of the dc electric field is essential for driving this instability.

For the instability mode in a nonuniform plasma with a density gradient sheared in the length L_n, one can obtain the dispersion relation equation from Eqs. 4.15 and 4.16.

$$(\frac{d^2}{dx^2} - k_y^2 + F(\omega)\frac{k_y(V_E'' - \Omega_e/L_n)}{\omega - k_y\Omega_e})\phi(x) = 0. \tag{4.18}$$

Ganguli *et al.*[73] derived the EIH instability dispersion relation for a uniform plasma with a finite $k_z L \neq 0$ in slab geometry,

$$[\frac{d^2}{dx^2} - k_y^2 - k_z^2 + F(\omega)(\frac{k_y V_E''(x)}{\omega - k_y V_E(x)} + \frac{k_z^2\Omega_e^2}{\omega - k_y V_E(x)})]\phi(x) = 0 \tag{4.19}$$

4.2.3 Numerical methods for solving the dispersion equation

We have so far discussed about the dispersion relation equation of EIH instability in both uniform and nonuniform plasmas. In this subsection, a numerical method[70, 72] will be introduced to solve the dispersion equation to obtain the electrostatic potential $\phi(x,\omega)$ in the region of the flow channel and the complex frequency of the instability mode. The frequency is decomposed into a real frequency and an imaginary frequency (growth rate):

$$\omega = \omega_R + i\gamma, \tag{4.20}$$

where ω_R denotes the real frequency of the EIH mode, and γ gives the growth rate (if positive) or damping rate (if negative).

The condition, that the electrostatic potential $\phi(x,\omega)$ is damped away from the region in which the electron flow is localized, is imposed to obtain an accurate numerical solution. The region of interest is divided into four intervals:

$$\phi(x,\omega) = \begin{cases} v_r(x,\omega), & x > x_r \\ \psi(x,\omega), & x_m < x < x_r \\ B\psi(x,\omega), & x_l < x < x_m \\ Bv_l(x,\omega), & x < x_l, \end{cases}$$

where v_r and v_l are the WKB solutions that are damped in the intervals $x > x_r$ and $x < x_l$, respectively; ψ_r and ψ_l are the numerically obtained solutions in the intervals $x_m < x < x_r$ and $x_l < x < x_m$, respectively; B is a constant. The function ψ_l is obtained by integrating from the point x_l toward the point x_m using the initial conditions that at the point $x = x_l$, ψ_l and its spatial derivative are equal to v_l and its spatial derivative, respectively. Similarly, the function ψ_r is obtained by integrating from the point x_r toward the point x_m using the initial conditions that at the point $x = x_r$, ψ_r and its spatial derivative are equal to v_r and its spatial derivative, respectively.

The electrostatic potential $\phi(x,\omega)$ and its spatial derivative should be continuous at the point x_m. This condition can be used to obtain the complex frequency ω and the constant B, both of which yield to the following results:

$$\begin{aligned} B &= \frac{\psi_r(x_m,\omega)}{\psi_l(x_m,\omega)}, \\ F(x_m,\omega) &= \frac{d}{dx}\ln\left(\frac{\psi_r(x_m,\omega)}{\psi_l(x_m,\omega)}\right) = 0. \end{aligned} \tag{4.21}$$

Note that for a randomly chosen ω, it doesn't follow that $F(x_m, \omega)$ vanishes unconditionally, since for a given ω, $\psi_r(x, \omega)$ and $\psi_l(x, \omega)$ satisfy specific initial conditions at the points x_r and x_l, respectively. Thus, their spatial derivatives are such that at the point x_m, Eq. 4.21 is not automatically satisfied.

The numerical procedure can be described as follows. Firstly, the density profile, magnetic field, and flow velocity are chosen along with values for the quantities x_l, x_m and x_r, and the initial guess of the frequency ω. The solution to Eq. 4.21 can be obtained by using the Muller's method[74]. This results in the desired value of the frequency and growth rate of the instability. The structure of the electrostatic potential can be obtained for the acquired ω. It is found that the electrostatic potential and the value of ω are nearly independent of x_m as long as it is chosen near the peak of the localized shear flow. In the same sense, the solution is nearly independently of x_r, and x_l as long as they lie further than a few skin depth layers away from the region of localization of the electrostatic potential $\phi(x, \omega)$.

4.3 Theoretical numerical solutions of the EIH instability

Based on the above numerical scheme, a shooting code is developed to solve the EIH dispersion equations to obtain the eigen functions and eigen values. Results in both uniform and nonuniform plasmas will be presented.

4.3.1 Numerical Investigation of EIH Instability in Uniform Plasmas

Based on the numerical method discussed above, a shooting code is developed to solve the dispersion equation in the uniform plasma Eq. 4.17. From the equation, it is seen that the eigenfunction ($\phi(x, \omega)$) and eigenvalue (ω) should depend on three quantities: $\delta = \omega_{pe}/\Omega_e$, $k_y L$ and $\alpha_1 = V_E^0/L\Omega_e$. V_E^0 is defined in the following way, $V_E(x) = V_E^0 f(x)$ and $f(x) = \mathrm{sech}^2(x)$.

Fig. 4.1 shows the plot of the typical eigenfunction electrostatic potential $\phi(x, \omega)$ of the EIH instability in the real space. The case used here has $\delta = 1.0$, $\alpha_1 = 0.3$ and $k_y L = 0.5$. The eigenvalue frequency can be obtained along with the eigenfunction as $\omega = (4.35 + 2.84i)\omega_{LH}$ for this case. Note that the black line represents the real part of $\phi(x, \omega)$, and the red line shows the imaginary part.

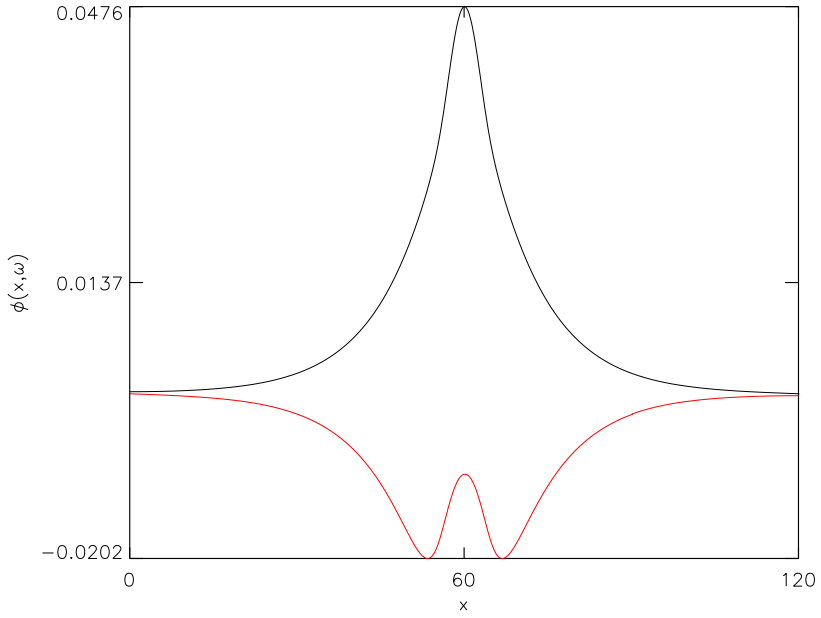

Figure 4.1: A typical eigenfunction electrostatic potential ($\phi(x, \omega)$) of EIH instability. Here $\delta = 1.0$, $\alpha_1 = 0.3$ and $k_y L = 0.5$. For this case, the frequency $\omega = (4.35 + 2.84i)\omega_{LH}$. The black line shows the real part of the eigenfunction, and the red line represents the imaginary part of the eigenfunction.

As it can be seen, the EIH instability in uniform plasmas depends on the three quantities δ, α_1 and $k_y L$, it is of interest to investigate how the eigenvalue frequency ω changes as one of the three quantities varies.

Fig. 4.2 shows the real frequency and growth rate (imaginary frequency) as a function of $k_y L$ for $\delta = 0.5$, 1.0 and 5.0 with $\alpha_1 = 0.3$ and $m_i/m_e = 1836$. It is seen from the figure that both real and imaginary frequency are on the order of ω_{LH}. The real frequency increases monotonously as the $k_y L$ increases, while the growth rate increases and decreases.

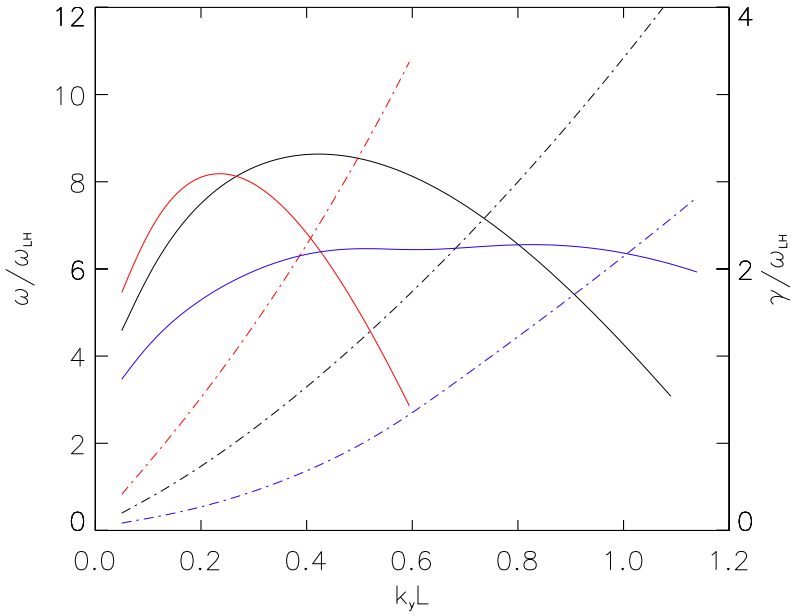

Figure 4.2: The real parts (dashed lines) and imaginary parts (solid lines) of the eigenvalues (ω) of Eq. 4.17 as a function of k_yL for $\delta = 0.5$ (red lines), 1.0 (black lines) and 5.0 (blue lines). Here $m_i/m_e = 1836$ and $\alpha_1 = 0.3$.

Fig. 4.3 is the plot of real frequency and growth rate versus the quantity $\alpha_1 = V_E^0/\Omega_e L$ for cases with $\delta = 0.5$ and 1.0. Here, $k_yL = 0.5$ and $m_i/m_e = 1836$. The figure shows that both the real frequency and growth rate increase monotonously and almost linearly as the quantity α_1 increases.

4.3.2 Numerical investigation of EIH instability in nonuniform plasma

The same numerical method is used to solve the dispersion equation (Eq. 4.18) of the EIH instability in the nonuniform plasma with a density gradient L_n. Here, in order to assist our further research with ALEXIS experimental device, the ion-electron mass ratio $m_i/m_e = 73440$ used in the device will be adopted in my current numerical investigations. The new parameter L_n introduced in the dispersion equation Eq. 4.18 will be evaluated together with L by the ratio L/L_n.

Fig. 4.4 shows the plot of the eigenvalue (the complex frequency ω) as a function of k_yL for the case with $\delta = 1.0$, $\alpha_1 = 0.1$ and $L/L_n = 0.5$. It is seen from the figure

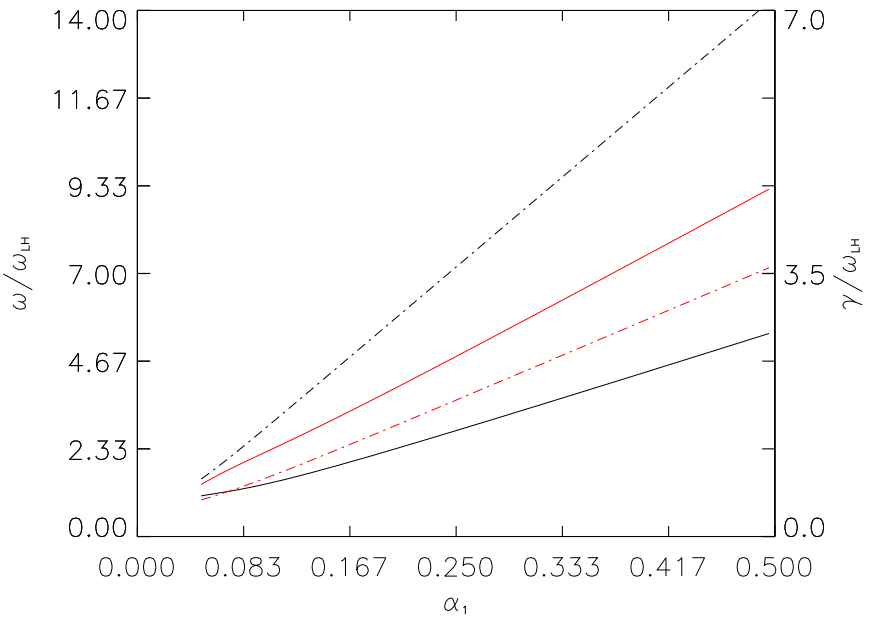

Figure 4.3: The real parts (dashed lines) and imaginary parts (solid lines) of the eigenvalues (ω) of Eq. 4.17 as a function of α_1 for $\delta = 0.5$ (red lines), 1.0 (black lines). Here $m_i/m_e = 1836$ and $k_y L = 0.5$.

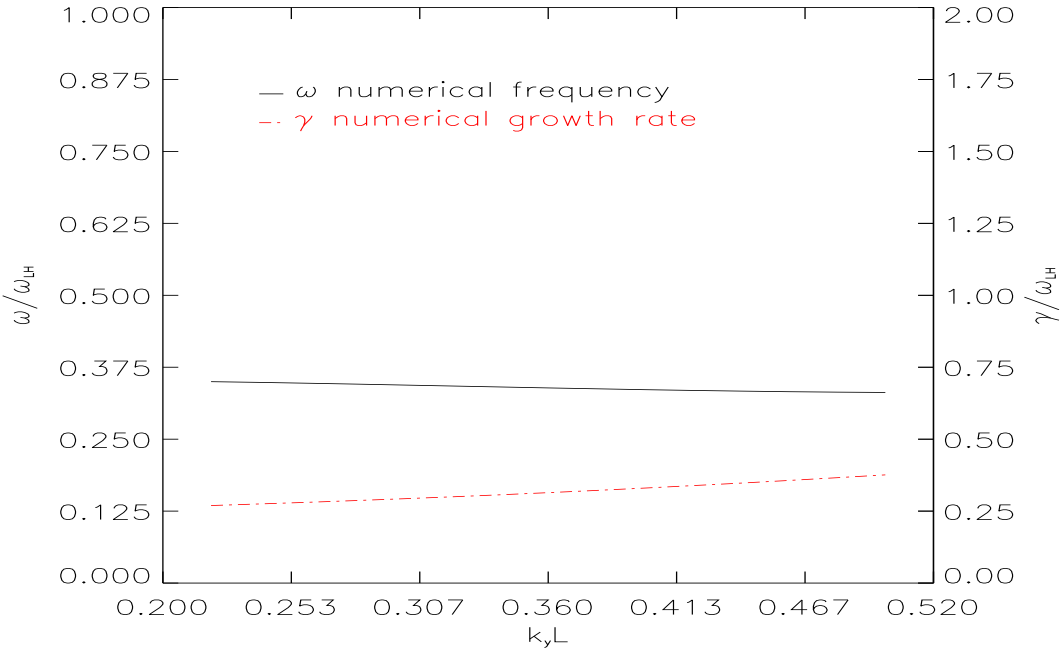

Figure 4.4: The real parts (black solid line) and imaginary parts (red dashed line) of the eigenvalue (ω, γ) of Eq. 4.18 as a function of $k_y L$ for $\delta = 1.0$, $\alpha_1 = 0.1$ and $L/L_n = 0.5$

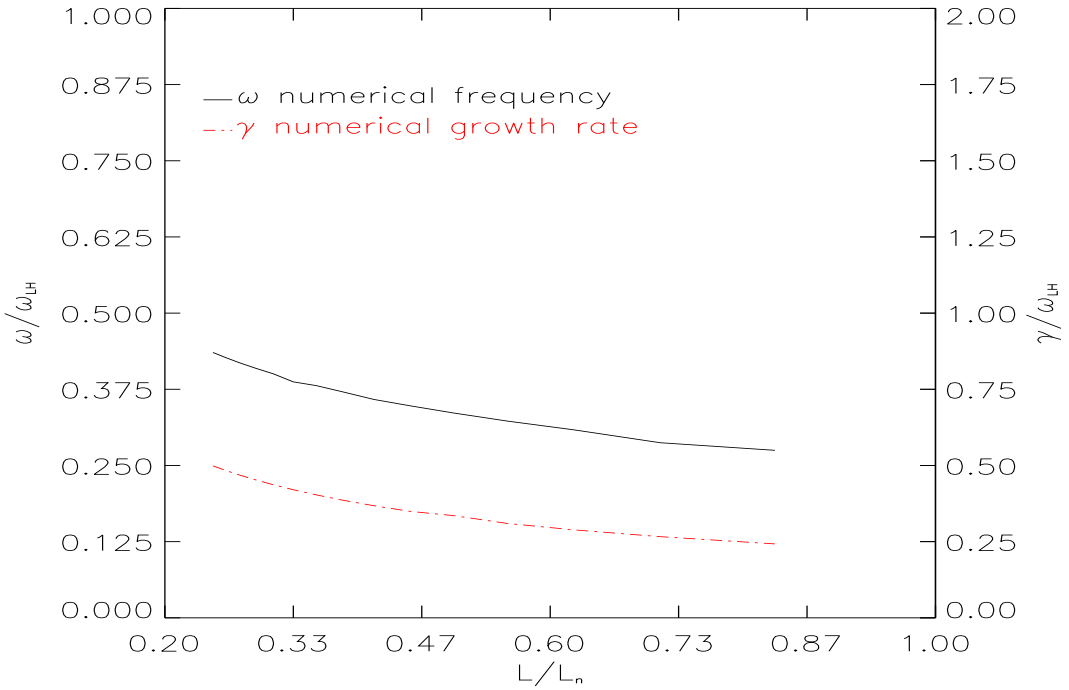

Figure 4.5: The real parts (black solid lines) and imaginary parts (red dashed line) of the eigenvalue (ω, γ) of Eq. 4.18 as a function of L/L_n for $\delta = 1.0$, $k_y L = 0.4$ and $\alpha_1 = 0.1$, L is fixed as $5.0\rho_e$.

that both the real frequency (black solid line) and the growth rate (red dashed line) vary slightly as $k_y L$ changes. In the nonuniform plasma, the frequency and growth rate of the EIH instability is not sensitive to the values of $k_y L$ in our selected cases.

The eigenvalue of Eq. 4.18 as a function of L/L_n is plotted in Fig. 4.5 for the case with $\delta = 1.0$, $\alpha_1 = 0.1$ and $k_y L = 0.5$. The black solid line is the real frequency and the red dashed line is the growth rate. It can be seen from the figure that as the ratio quantity L/L_n increases, both the real frequency and growth rate decreases. Since as L/L_n approaches zero, the nonuniform cases actually become uniform cases, we can expect both the frequency and growth rate approach the frequencies in the corresponding uniform cases.

4.4 Linear GeFi simulation of the EIH instability

Linear simulation results of EIH instabilities from linear GeFi model in the electrostatic limit are presented and compared with the results from the numerical solutions of the dispersion equations. The results include kinetic simulations in slab geometry with uniform plasmas and nonuniform plasmas ($k_z L = 0$), and kinetic simulations in cylindrical geometry with uniform plasmas and nonuniform plasmas ($k_z L = 0$), and kinetic simulations in slab geometry and uniform plasmas with $k_z L \neq 0$. Real experimental parameters in the ALEXIS device are adopted in the kinetic simulations, and results are compared with the experiments as well.

4.4.1 Simulation model

Initial setup of the GeFi particle simulation in both slab geometry and cylindrical geometry are introduced here along with the particle distribution function and boundary condition.

In the slab geometry GeFi particle simulation, an external static magnetic field $\mathbf{B_0}$ is in the z direction with unit magnitude, and an electric field as a function of x, $\mathbf{E}(x)$ is in the x direction. Thus the $\mathbf{E} \times \mathbf{B}$ drift flow will be in y direction and dependent on x. 2-D simulations are performed in $x - y$ plane, thus $k_{\|} = 0$. The boundary condition in y direction is set to be periodic, whereas the boundary condition in x direction is a conductor boundary. Assuming that the domain length in x direction is L_x, and the shear scale length is denoted as L, the electric field takes this form $E(x) = \alpha_1 L \Omega_e \mathrm{sech}^2((x - L_x/2)/L)$. Ion-electron mass ratio $m_i/m_e = 1836$ and light-Alfvèn speed ratio $c/V_A = 42.8$, thus the parameter $\delta = \omega_{pe}/\Omega_e = 1$. The quantity δ can be varied by changing c/V_A and m_i/m_e, since the relation $\delta = (c/V_A)/\sqrt{m_i/m_e}$ can be derived.

When the GeFi particle simulation of EIH instability is extended to a cylindrical geometry (r, θ, z) and uniform plasmas. An external static magnetic field $\mathbf{B_0}$ is in the

z direction with unit magnitude, and an electric field as a function of radial position r, $\mathbf{E}(r)$ is in the radial direction. Thus the $\mathbf{E} \times \mathbf{B}$ drift motion is in θ direction and dependent on r. 2-D simulations are performed in $r - \theta$ plane, thus $k_{\|} = 0$. The boundary condition in θ direction is set to be periodic, whereas the boundary condition in r direction is a conductor boundary. Assuming that the domain length in r direction is L_r, and the shear scale length is denoted as L, the electric field takes this form $E(r) = \alpha_1 L \Omega_e \mathrm{sech}^2((r - L_r/2)/L)$. Ion-electron mass ratio $m_i/m_e = 1836$ and light-Alfvèn speed ratio $c/V_A = 42.8$ yield $\delta = 1.0$.

Velocity distribution in the GeFi particle simulation for electrons takes the form of drift Maxwellian distribution,

$$f(\mathbf{v}) = (\frac{m_e}{2\pi\kappa T})^{3/2} \exp(-\frac{m_e|\mathbf{v} - \mathbf{v_d}|^2}{2\kappa T}), \tag{4.22}$$

where $\mathbf{v_d}$ is the $\mathbf{E} \times \mathbf{B}$ drift velocity. While for ions, the velocity distribution is normal Maxwellian.

4.4.2 EIH instability in a slab geometry and uniform plasma with $k_z = 0$

The case with $\delta = 1.0$, $k_y L = 0.5$ and $\alpha_1 = 0.3$ is performed in the GeFi particle simulation in slab geometry and uniform plasmas. In this case, we would like to compare the eigenfunction and eigenvalue from simulation with that from numerically solving the dispersion equation. Fig. 4.6 shows the plot of the eigenfunction from both the simulation and numerical solution. The solid black (red) line shows the real (imaginary) eigenfunction from the numerical solution, whereas the dashed lines are from the simulations. As it can be seen from the figure, both the real and imaginary eigenfunction from our GeFi simulation can match well with that from the numerically solving the dispersion relation. The eigenvalue (frequency) from the numerical solution is $\omega_t = (4.34, 2.84)\omega_{LH} = (131.54, 86.17)\Omega_i$, and the eigenvalue

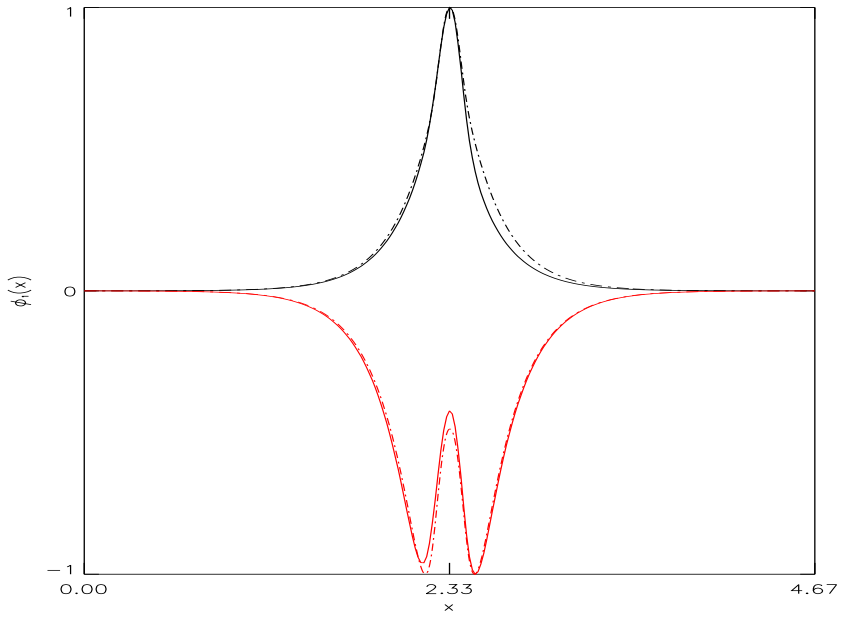

Figure 4.6: Plot of the eigenfunction of the perturbed electrostatic potential. Solid black (red) line is the real (imaginary) eigenfunction from numerically solving the dispersion equation. Dashed black (red) line is the real (imaginary) eigenfunction from the GeFi simulation.

from our simulation can be analyzed by FFT method to yield $\omega_s = (4.24, 2.69)\omega_{LH} = (128.30, 81.40)\Omega_i$. The eigenvalue from the GeFi simulation is close to that from the theory as well. Therefore, the conclusion, that our GeFi simulation of EIH instability can agree with the theory very well, can be drawn.

Fig. 4.7 is the contour plot of perturbed physical quantities n_i (ion density), n_e (electron density), ϕ (electrostatic potential), $\mathbf{E}$ (electric field), $\mathbf{U_i}$ (ion flow velocity) and $\mathbf{U_e}$ (electron flow velocity) in the (x, y) real space for a typical case in the linear GeFi kinetic simulation in the electrostatic limit. The contour structure of U_{ey} shows the sheared electron flow in y direction at the center of x domain. Structures of n_i, n_e, ϕ, E_x and E_y clearly demonstrate the EIH instability excited in the regime of the sheared electron flow.

Fig. 4.8 is the plot of real frequencies (ω) and the growth rates (γ) normalized by lower hybrid frequency (ω_{LH}), as a function of $k_y L$, which is the wave vector in

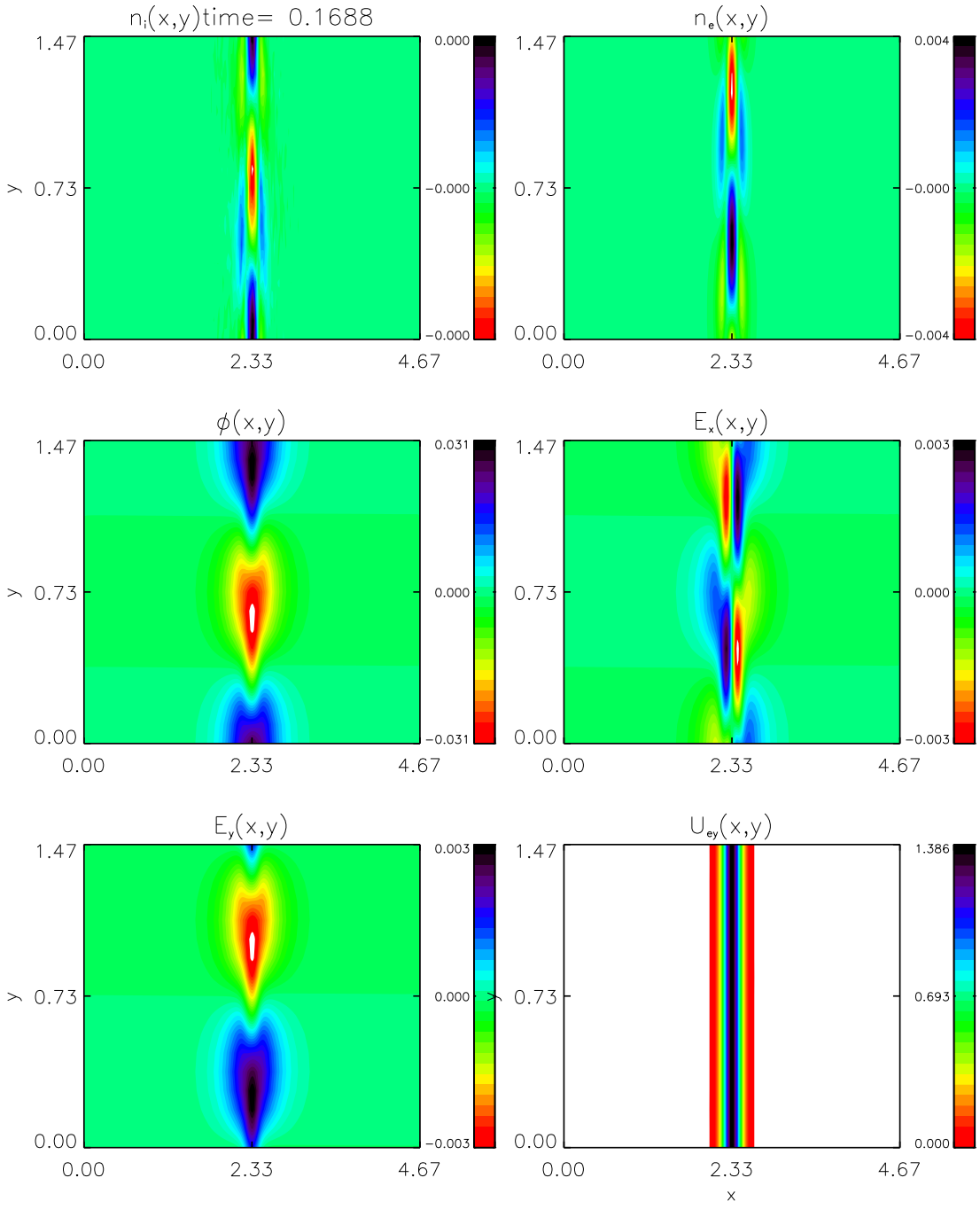

Figure 4.7: Contour plot of perturbed physical quantities in (x, y) real space.

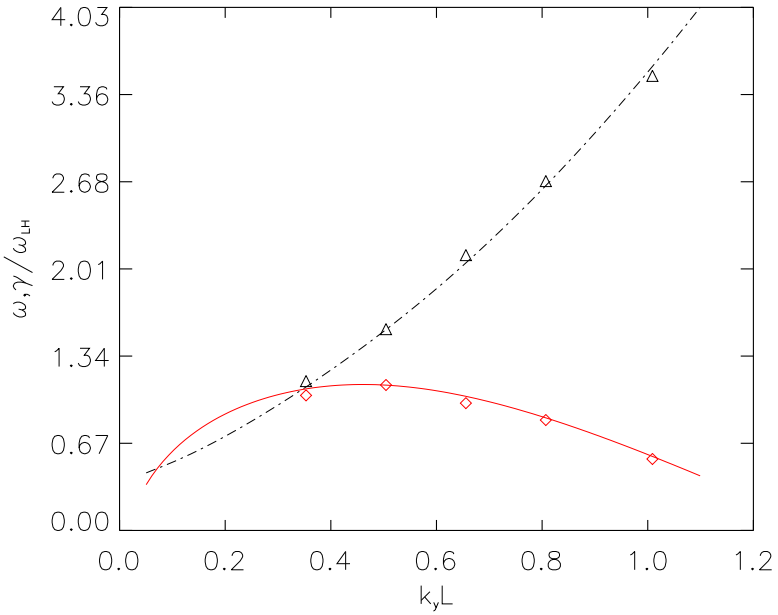

Figure 4.8: Plot of real frequency (ω) and growth rate (γ) normalized by lower hybrid frequency (ω_{LH}), as a function of k_yL. Dashed black line is the real frequency and solid red line is the growth rate, both of which are from the theory. The black dots (red dots) are real frequency (growth rate) from the GeFi simulation

y direction and normalized by the shear scale length L. Here, δ is hold to be 1, and $\alpha_1 = 0.1$. It can be seen from the figure that the dots from either the real frequencies or the growth rates are on the theoretical lines, indicating that the GeFi kinetic simulations have excellent agreement with the linear theoretical predications.

Fig. 4.9 is similar to Fig. 4.8. For the same purpose, here we hold $\delta = 1.0$ and $k_yL = 0.5$, but vary the values of α_1 to study the dependence of EIH instability on the shear flow strength. It can also be seen from this figure, the real frequencies (black dots) and growth rates (red dots) from GeFi kinetic simulations have excellent agreement with the eigenvalues of the dispersion equation.

It can be then summarized that in uniform plasmas, EIH instability can be excited perfectly in the linear GeFi kinetic simulations for a wealth of parameters. The example eigenfunction plot (Fig. 4.6) and the plot of real frequencies and growth rates as functions of k_yL (Fig. 4.8) and α_1 (Fig. 4.9) demonstrate very good agreement

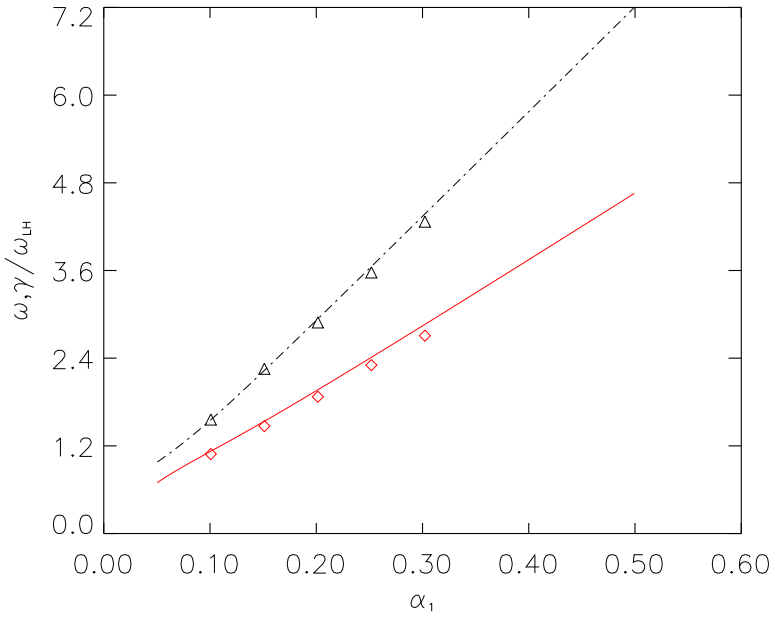

Figure 4.9: Plot of real frequency (ω) and growth rate (γ) normalized to lower hybrid frequency (ω_{LH}), as a function of α_1. Dashed black line is the real frequency and solid red line is the growth rate, both of which are from the theory. The black dots (red dots) are real frequency (growth rate) from the GeFi simulation

with the eigen functions and eigen values of the dispersion differential equation in slab geometry and uniform plasmas, Eq. 4.17.

4.4.3 EIH instability in a slab geometry and nonuniform plasma with $k_z = 0$

GeFi kinetic simulations of EIH instability in a slab geometry and nonuniform plasma with a density gradient L_n are presented and compared with the eigen values of the corresponding dispersion differential equation, Eq. 4.18.

Setup of the sheared electric field is the same as before, while the sheared density profile is embedded in the system as a function of x

$$n(x) = n_0 - \frac{\delta n}{2}[1 + \tanh(\frac{x - \frac{L_x}{2}}{L_n})]. \tag{4.23}$$

Here L_x is the domain length in x direction, n_0 is a constant as the lowest density, δn is the difference of the highest density and the lowest density.

For the purpose of further investigation in the experiments, the ALEXIS device parameters are adopted in the current simulations. External background magnetic field $b_0 = 127.5(Gauss)$, background density $n_0 = 3.86 \times 10^8(cm^{-3})$, peak value of external electric field $E_0 = 20.3(Volt/cm)$, shear length of electric field $L = 0.35(cm)$, shear length of density $L_n = 0.85(cm)$, electron temperature $T_e = 5.33(eV)$, ion to electron temperature ratio $T_i/T_e = 0.001$, ion to electron mass ratio $m_i/m_e =$ 73440 (Argon plasma), light speed to Alfvén speed ratio c/V_A=42.8, the beta value of electron $\beta_e = 0.004$.

Fig. 4.10 is the plot of real frequencies and growth rates as a function of k_yL from both simulations and numerical solutions of the dispersion equation. The figure shows that GeFi simulation results have very good agreement with the theoretical predications. In the same format, in Fig. 4.11 real frequencies and growth rates are plotted as a function of the ratio L/L_n with $L = 0.35cm$ and $k_yL = 0.22$ being fixed. From the figure, it can be seen that GeFi simulations have good agreement with the theory.

4.4.4 EIH instability in cylindrical geometry and uniform plasma with $k_z = 0$

The investigation of EIH instability is extended to a cylindrical geometry (r, θ, z) and uniform plasma by utilizing GeFi particle simulation. Results are presented in the following.

Fig. 4.12 is a contour plot of perturbed physical quantities for a typical EIH simulation in a similar format to Fig. 4.7. In the contour structure in U_{ey}, the sheared electron flow is seen to be in θ direction and dependent on r. From the contour plots of n_e, ϕ, E_x and E_y, It can be seen that the EIH instability structures

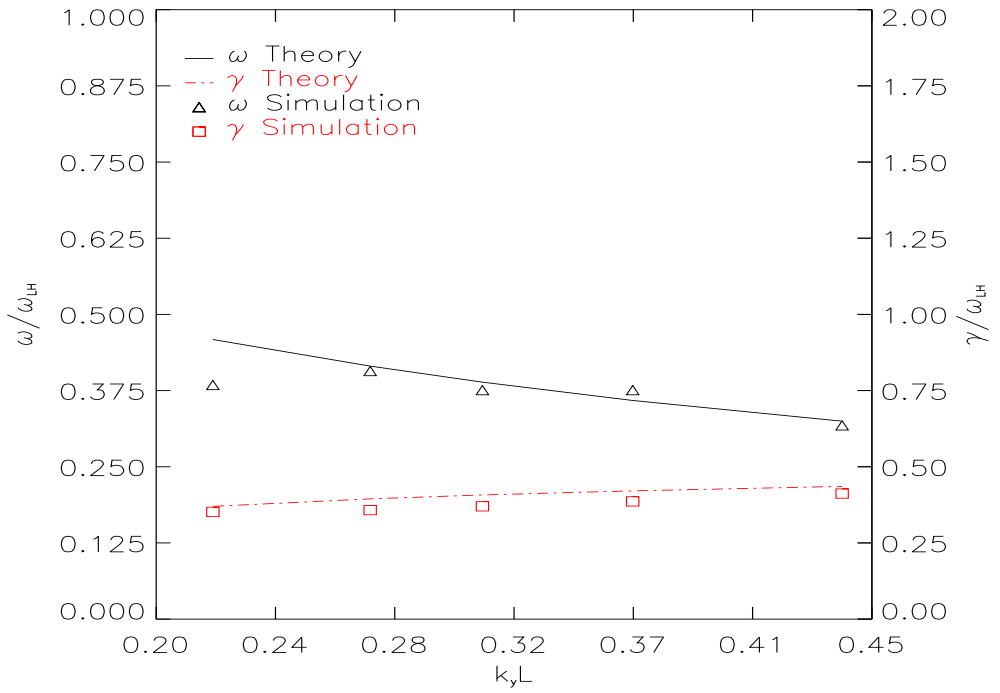

Figure 4.10: Plot of real frequency and growth rate as a function of $k_y L$.

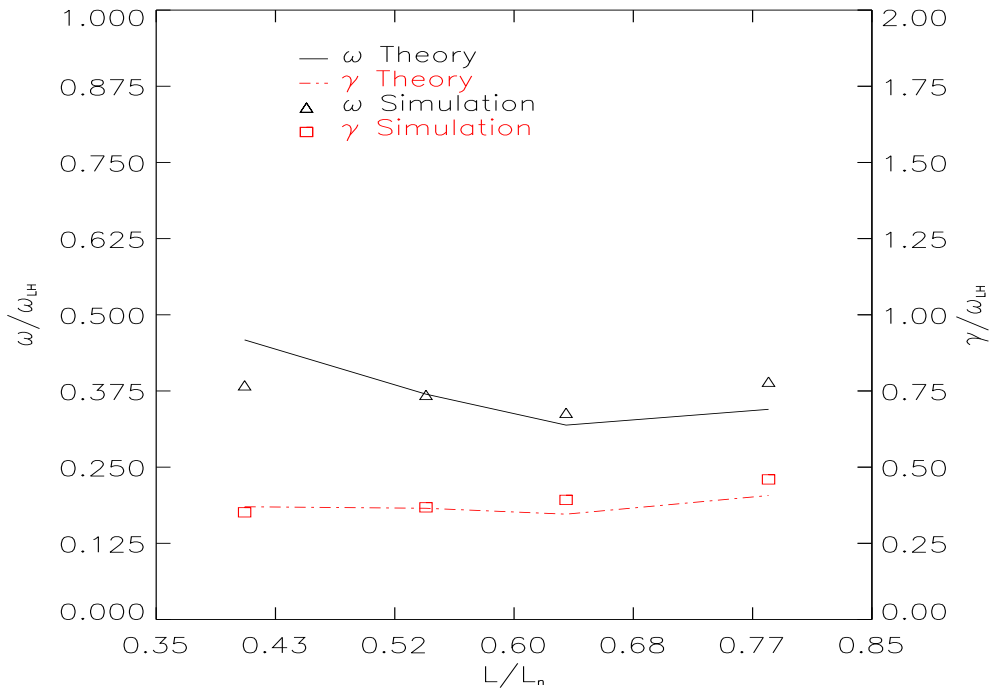

Figure 4.11: Plot of real frequency and growth rate as a function of the ratio L/L_n with $L = 0.35cm$ and $k_y L = 0.22$ being fixed.

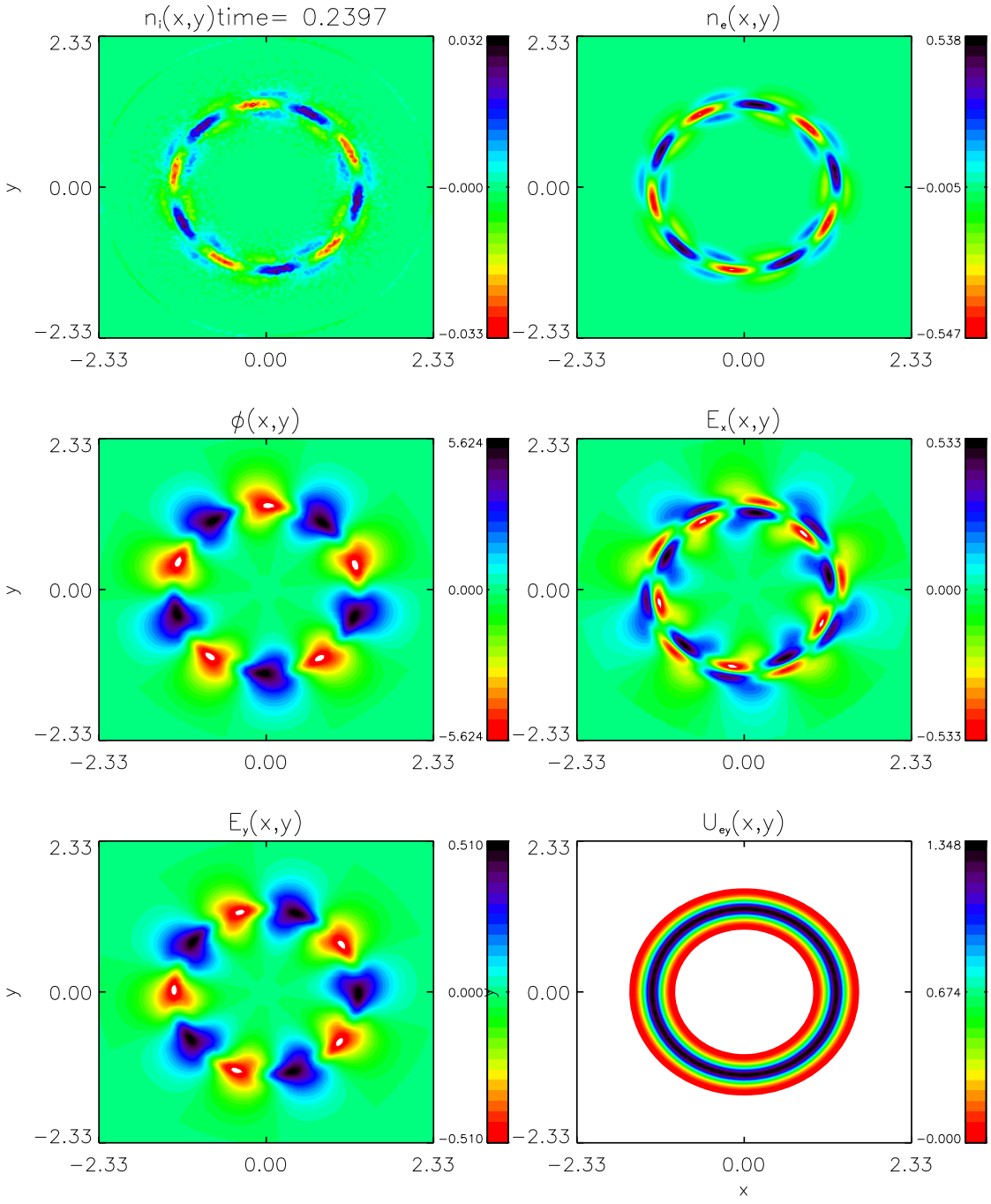

Figure 4.12: Contour plot of perturbed physical quantities in (r, θ) real space

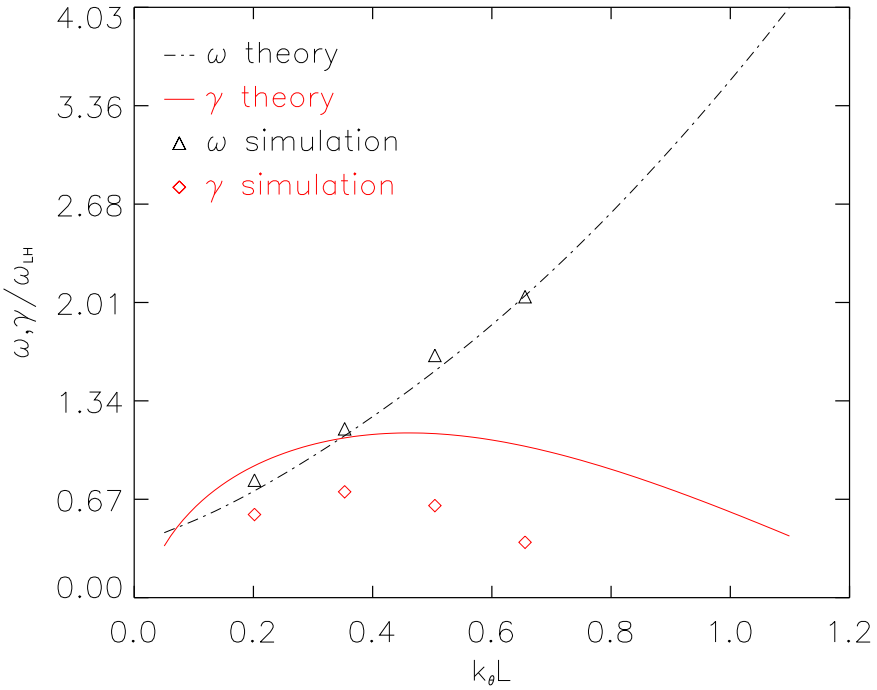

Figure 4.13: Plot of real frequency (ω) and growth rate (γ) normalized to lower hybrid frequency (ω_{LH}), as a function of $k_\theta L$.

are formed near the center of the radial direction. In θ direction, the mode number is clearly shown to be five as expected.

It is of interest for us to compare the simulation results in cylindrical geometry with the theory, although the EIH theory is in a slab geometry. Fig. 4.13 is a plot of real frequency and growth rate as a function of $k_\theta L$ for cases with $\delta = 1.0$ and $\alpha_1 = 0.1$. It can be seen from the figure that real frequencies have excellent agreement with the dispersion relation, while growth rates are in the same trend as that from the dispersion theory. The difference of the growth rates between simulations and theory may be due to the cylindrical effects in our simulations, whereas the theoretical calculation has assumed a slab geometry.

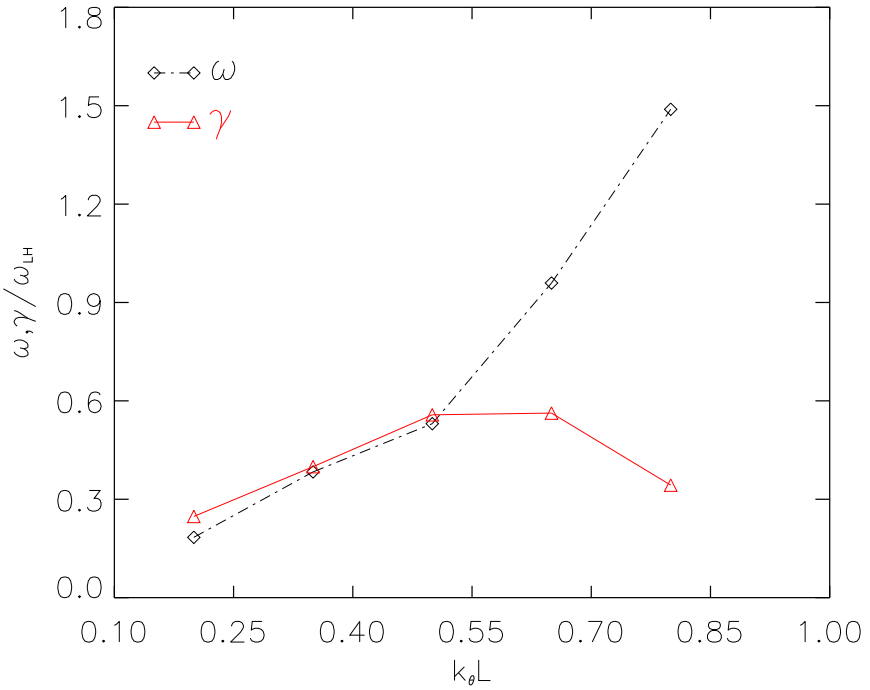

Figure 4.14: Real frequency and growth rate as a function of $k_\theta L$

4.4.5 EIH instability in cylindrical geometry and nonuniform plasma with $k_z = 0$

EIH instability in cylindrical geometry and inhomogeneous plasma with a density gradient L_n in radial direction is studied. The setup of the sheared electric field is the same as before, while the sheared density profile is embedded in the system as a function of r

$$n(r) = n_0 - \frac{\delta n}{2}[1 + \tanh(\frac{r - \frac{L_r}{2}}{L_n})]. \tag{4.24}$$

Here L_r is the domain length in r direction, n_0 is a constant as the lowest density, δn is the difference of the highest density and the lowest density.

Figs. 4.14 and 4.15 are plots of real frequency and growth rate, from measurements of GeFi kinetic simulations, as functions of $k_\theta L$ ($\delta = 1.0, \alpha_1 = 0.1, L/L_n = 0.41$) and α_1 ($\delta = 1.0, k_\theta L = 0.5, L/L_n = 0.41$), respectively. It is seen from fig. 4.14, the frequency increases as $k_\theta L$ increases, while the growth rate increases first to reach a

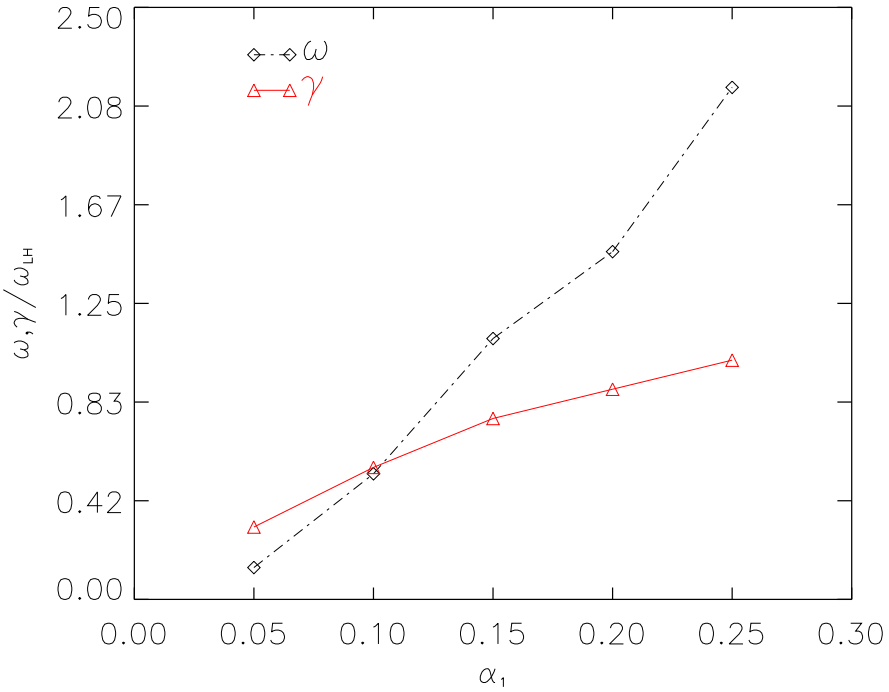

Figure 4.15: Real frequency and growth rate as a function of α_1

peak value, and decrease afterwards. However, both the real frequency and growth rate increase along with α_1, as shown in fig. 4.15.

4.4.6 EIH instability with $k_z \neq 0$

It is also of interest to study finite $k_{\|}$ effects on the excitation of EIH instability. Here, a uniform plasma in cylindrical geometry is used. An external static magnetic field $\mathbf{B_0}$ is in the z direction with unit magnitude, and an electric field as a function of radial positions r, $\mathbf{E}(r)$ is in the radial direction. Thus the $\mathbf{E}\times\mathbf{B}$ drift motion is in θ direction and dependent on r. 3-D simulations are performed in r, θ, z directions, thus k_z ($k_{\|}$) is not zero. The boundary conditions in θ and z directions are set to be periodic, whereas the boundary condition in r direction is a conductor boundary.

Realistic parameters in ALEXIS device are adopted in GeFi kinetic simulations: external magnetic field $B_0 = 127.5$(Gauss), electron temperature $T_e = 5.33$(eV), background density $n_0 = 6.0 \times 10^8(\mathrm{cm}^{-3})$, peak value of external electric field $E_0 =$

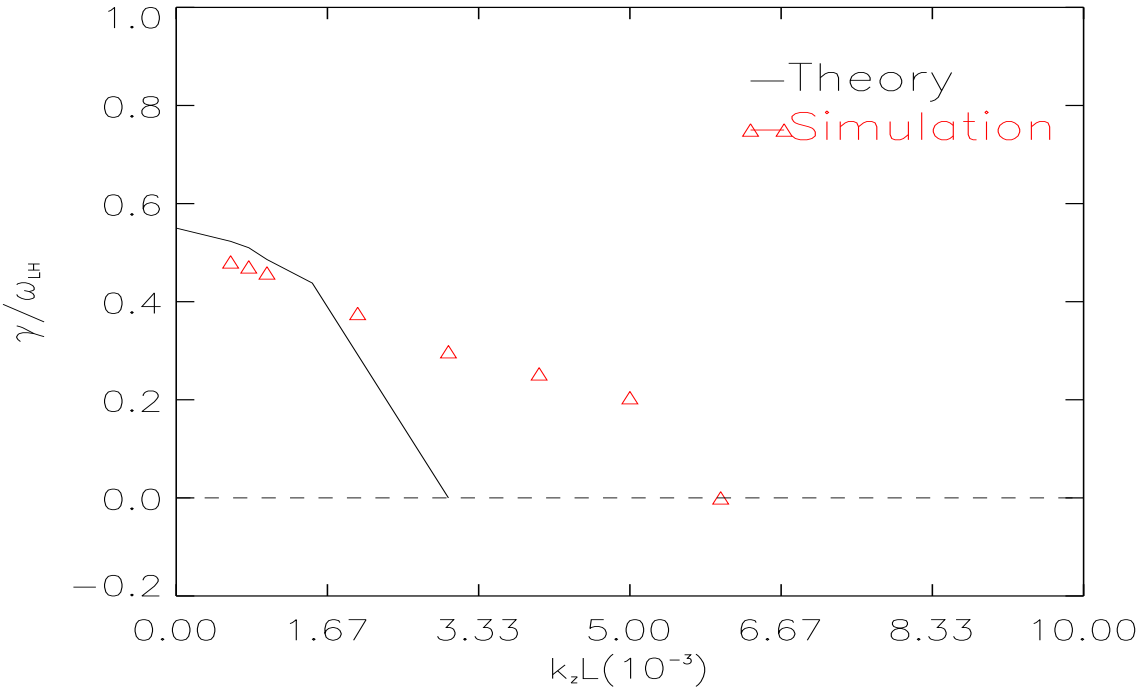

Figure 4.16: Growth rates vs k_zL.

7.0(V/cm), shear scale length of electric field $L = 0.4$(cm) and wave number in θ direction (normalized to L) $k_\theta L = 0.5$. Wave vector in z direction (normalized to L) k_zL varies from 0.0008 to 0.007.

Fig. 4.16 is a plot of growth rates as a function of k_zL from theoretical predications and GeFi kinetic simulations, both of which indicate that the growth rate decreases as the wave vector k_zL increases, and finally the growth rate is zero as k_zL becomes greater than certain values. GeFi simulation result is in the same trend as theory, whereas the theory predicates the growth rate dcreases much faster than the GeFi simulations. From the theory, critical value of k_zL for the growth rate to become zero is about 0.003, while GeFi kinetic simulation determines this value to be about 0.006.

With the same parameters as given above, an experiment is performed in ALEXIS device, and the frequency is measured in the uniform plasma region, as shown in Fig. 4.17. From the figure, it is seen that there is not any frequency observed except the

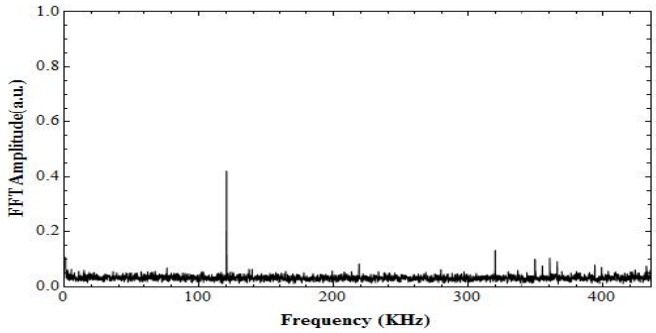

Figure 4.17: A measurement from the ALEXIS experiment, in which no instability is found. The spikes are the noise in the circuit.

noise spikes in the circuit, indicating no instability modes are excited. The reason is that the length of ALEXIS device is $L_z = 1.7$(m), and thus $k_z L$ can be estimated from this length to be about 0.0148, which is much greater than either the critical value from theory 0.003 or that from GeFi simulations 0.006. The result from ALEXIS experiment is consistent with that from GeFi kinetic simulations.

For the values of $k_z L$ that can excite EIH instability, it is interesting to investigate the effects of finite $k_z L$ on the frequencies and growth rates for different $k_\theta L$, as shown in Fig. 4.18. It can be seen from the figure that both frequencies and growth rates from a finite $k_z L = 0.005$ are lower than that from $k_z L = 0.000$. The differences between $k_z L = 0.005$ and $k_z L = 0.000$ in either frequency or growth rate are larger at smaller $k_\theta L$ region and smaller at larger $k_\theta L$ region. It can be concluded that finite $k_z L$ effects decrease either the frequency or the growth rate of EIH instability, and the effects are more significant with small $k_\theta L$ than that with larger $k_\theta L$.

4.5 Nonlinear evolution of EIH instability

Nonlinear GeFi particle simulations are then performed to investigate the nonlinear evolution of EIH instability in a slab geometry and uniform plasma with $k_z L = 0$.

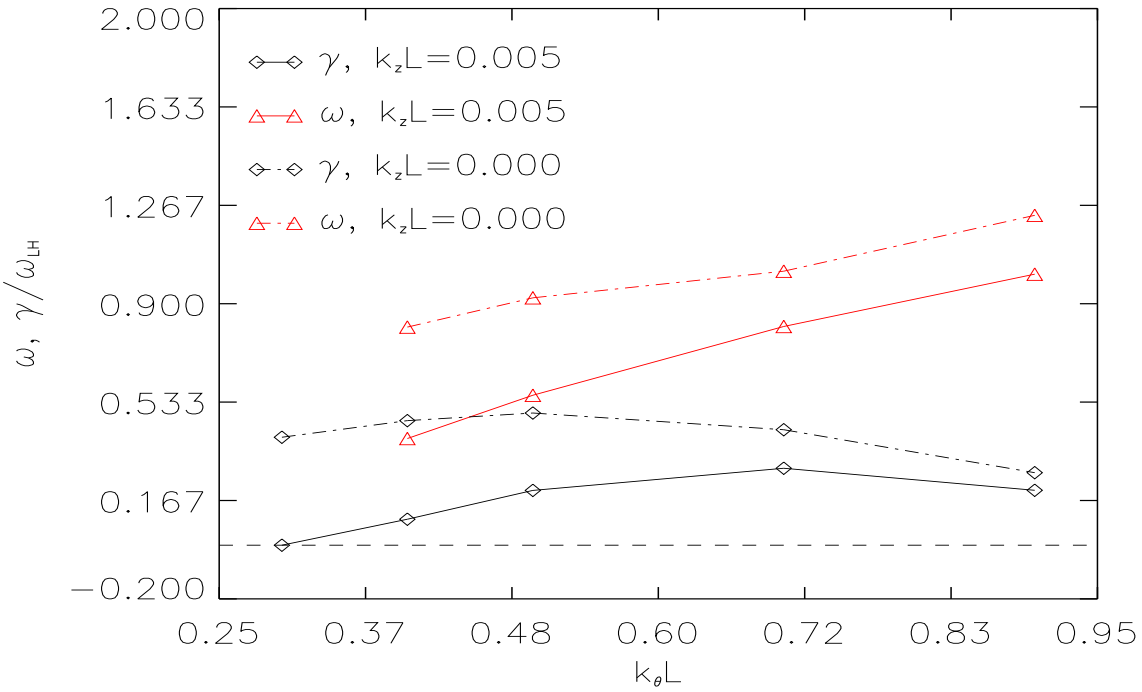

Figure 4.18: Frequencies and growth rates vs $k_\theta L$ for $k_z L = 0.005$ and $k_z L = 0.000$.

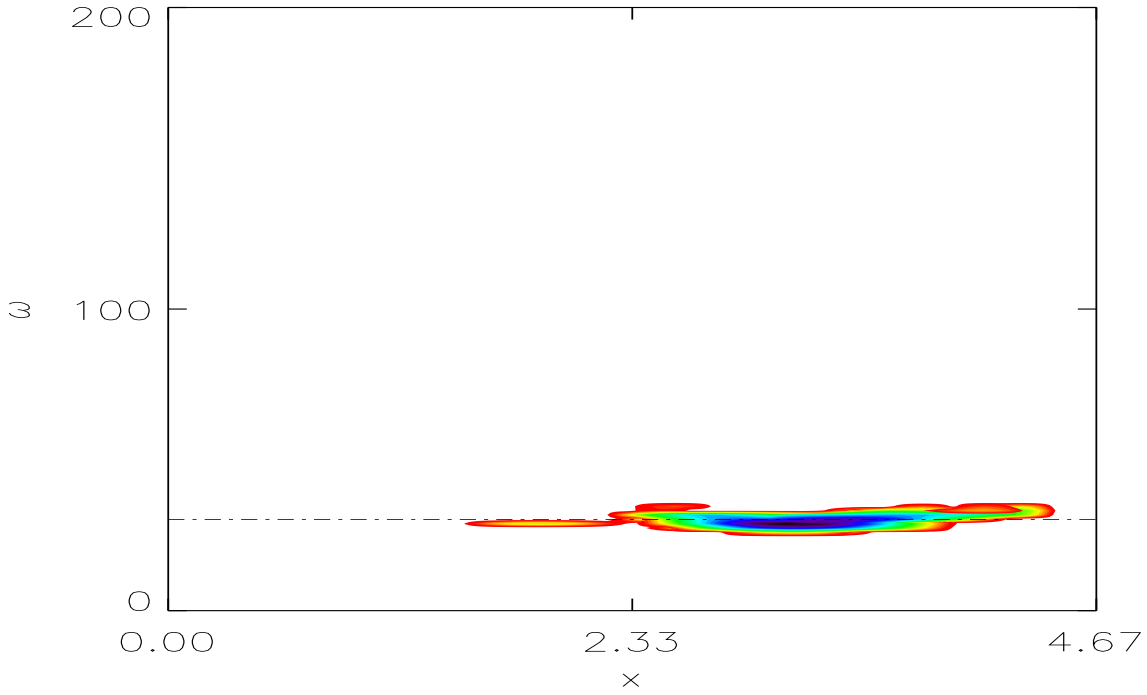

Figure 4.19: Contour plot of electrostatic potential in (ω, x) space in a nonlinear simulation.

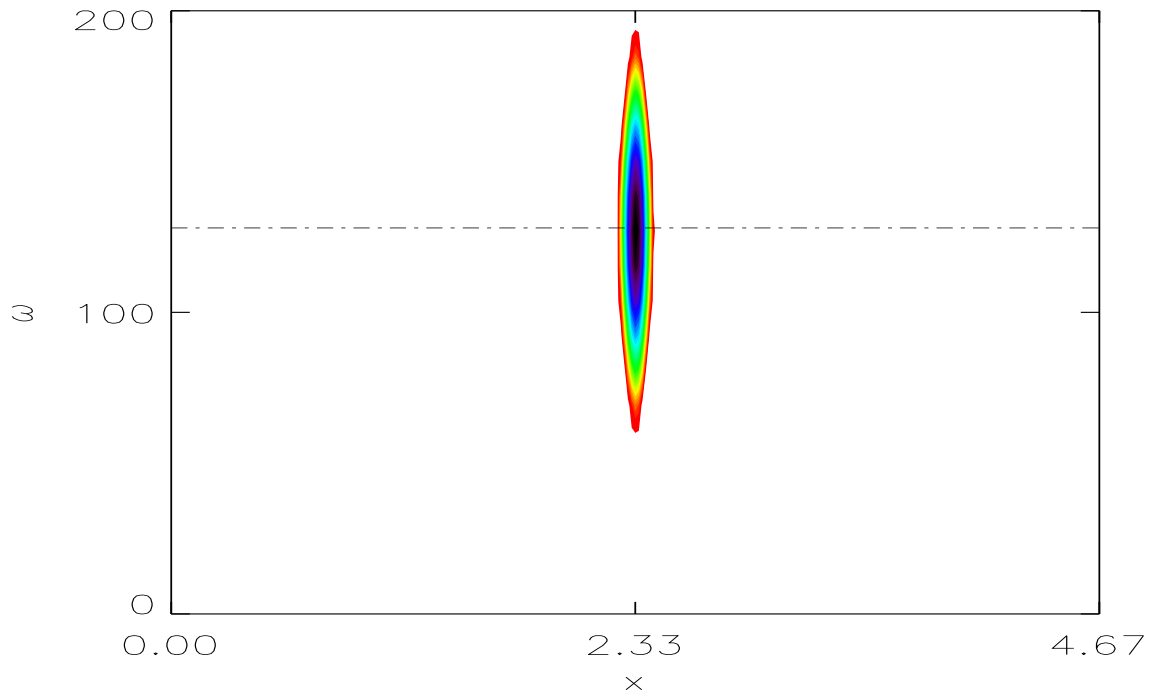

Figure 4.20: Contour plot of electrostatic potential in (ω, x) space in a linear simulation.

Figs. 4.19 and 4.20 are contour plots of electrostatic potentials in (ω, x) space for the case with $\delta = 1.0, \alpha_1 = 0.3, k_y L = 0.5$ in a nonlinear simulation and linear simulation, respectively. The normalization in x axis is ion gyro radius ρ_i, while the normalization in y axis is ion gyro frequency Ω_i. It is seen from Fig. 4.19 that the nonlinear frequency is about $1.0\omega_{LH}$ ($\omega_{LH} = 30.26\Omega_i$ in this case), and the linear frequency from Fig. 4.20 yields $4.24\omega_{LH}$. The linear frequency structure is at the center of x domain, where the shear flow locates, while the nonlinear frequency structure is not at the center of x domain. Figure 4.21 shows the frequency FFT analysis for a nonlinear simulation with $\delta = 1.0, \alpha_1 = 0.1, k_y L = 0.7$. The peak of the plot indicates the nonlinear frequency, which is $1.64\omega_{LH}$. The red dashed lines indicate the linear frequency $2.25\omega_{LH}$. From both cases, the nonlinear EIH frequency is smaller than the linear frquency.

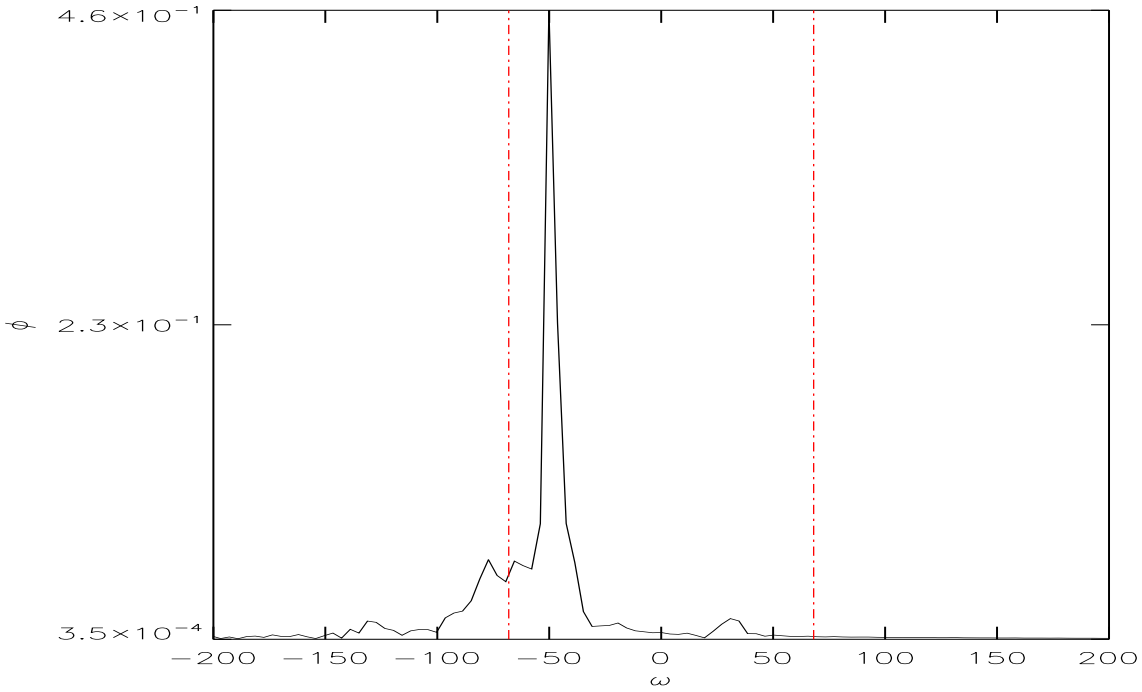

Figure 4.21: Plot of electrostatic potential as a function of ω.

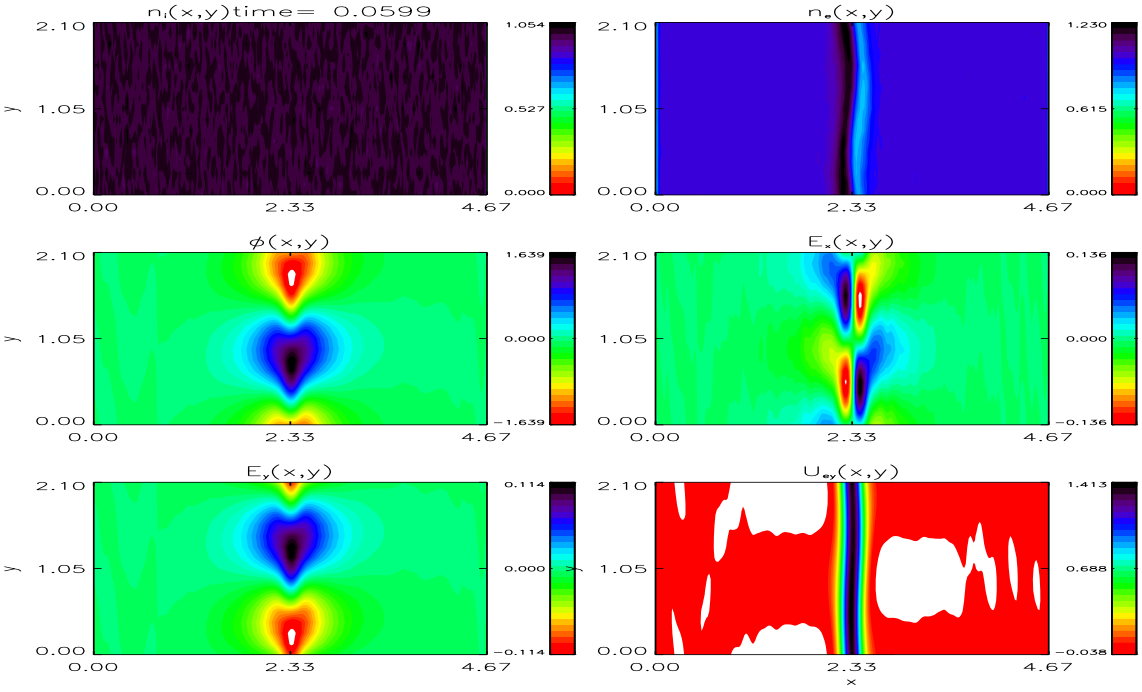

Figure 4.22: Contour plots of physical quantities in real space from a nonlinear simulation with $\delta = 1.0, \alpha_1 = 0.3, k_y L = 0.35$ at $\Omega_i t = 0.0599$.

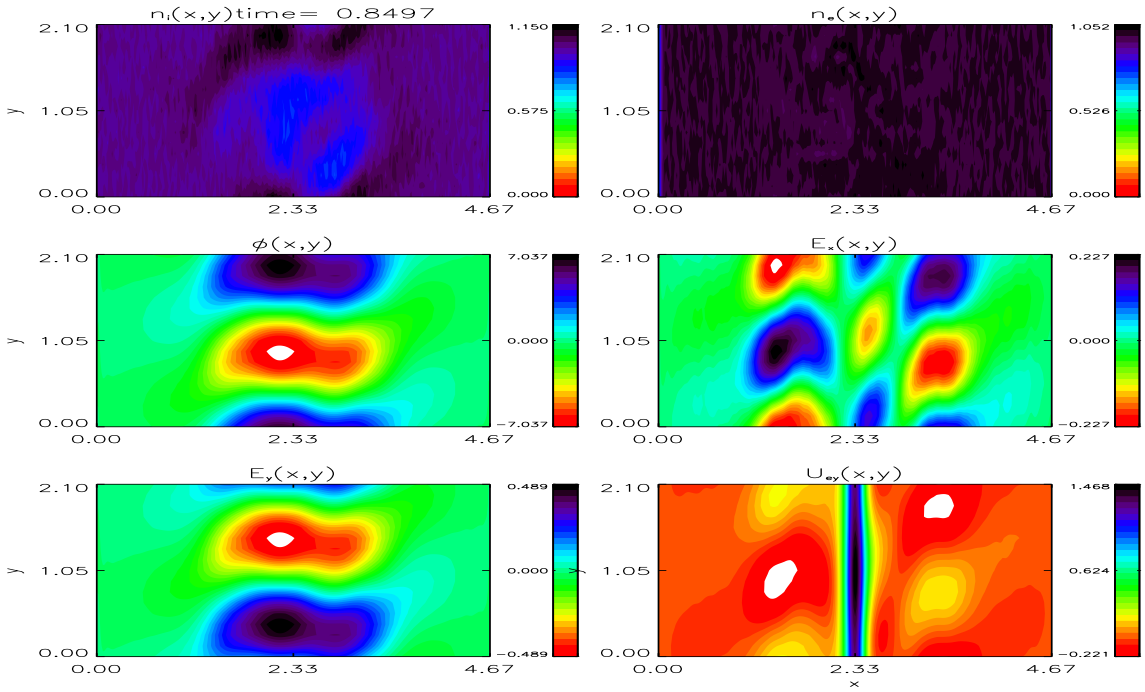

Figure 4.23: Contour plots of physical quantities in real space from a nonlinear simulation with $\delta = 1.0, \alpha_1 = 0.3, k_y L = 0.35$ at $\Omega_i t = 0.8497$.

Figures 4.22 and 4.23 are contour plots of physical quantities in real space from a nonlinear simulation with $\delta = 1.0, \alpha_1 = 0.3, k_y L = 0.35$ at $\Omega_i t = 0.0599$ and $\Omega_i t = 0.8497$, respectively. From the comparison between the two figures, it can be seen that at earlier time $\Omega_i t = 0.0599$, the structures of the EIH instability indicate a shorter wave length ($k\rho_i \sim 12$), while at later time $\Omega_i t = 0.8497$ the structures become wider in x direction, indicating a longer wave length ($k\rho_i \sim 3$).

Figure 4.24 is a plot of EIH frequency from nonlinear GeFi particle simulations as a function of $k_y L$ for cases with $\delta = 1.0, \alpha_1 = 0.1$. It can be seen from the figure that when the wave number $k_y L$ is less than about 0.65, the nonlinear EIH frequency changes slightly, and is around $1.0\omega_{LH}$. When $k_y L$ is greater than 0.65, as $k_y L$ increases, the frequency increases and approaches the corresponding linear EIH frequency.

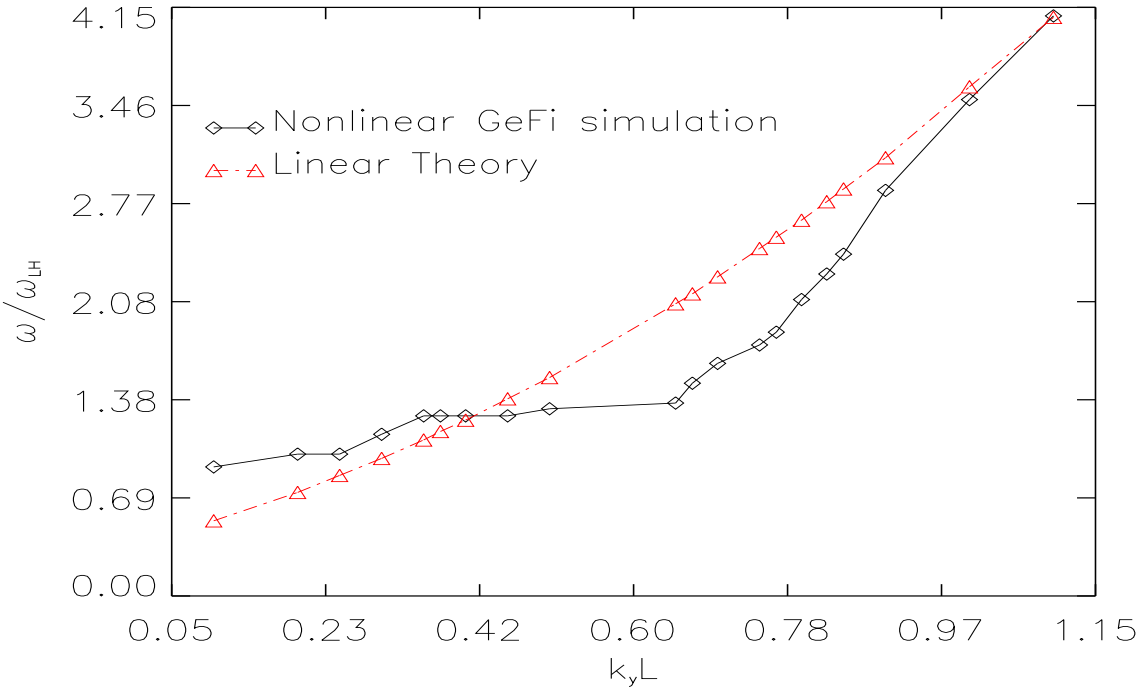

Figure 4.24: Nonlinear EIH frequency as a function of $k_y L$ for cases with $\delta = 1.0, \alpha_1 = 0.1$. Black solid line is nonlinear GeFi particle simulation results, and red dashed line is for linear theory.

4.6 Summary

In this chapter, the electron-ion hybrid (EIH) instability is reviewed in theory and investigated in our GeFi simulations. With a sheared electric field present in either uniform or nonuniform plasma, the EIH instability mode can be generated. The dispersion equation for EIH mode in uniform plasma is introduced as Eq. 4.17, and the dispersion relation in the nonuniform plasma with a density gradient sheared in the length L_n is given in Eq. 4.18. A numerical method is introduced to solve both dispersion equations to obtain the complex eigen function and eigen values. By this numerical method, a shooting code is programmed in Fortran to numerically calculate the eigen functions and values of the dispersions. Various parameters are adopted to obtain the numerical solutions to the dispersion equations, and the results are presented in section 4.1.4.

GeFi model is then used to simulate the EIH instability. The following conclusions can be drawn from GeFi particl simulations.

(1) Results of EIH instability in a uniform plasma and slab geometry from linear GeFi particle simulations have very good agreement with the linear theory.

(2) In the cylindrical geometry, frequencies from linear GeFi particle simulations have good agreement with the linear theory for a slab geometry, while the growth rates are lower than the theoretical values, but in the same trend.

(3) In the uniform plasma in a cylindrical geometry, GeFi particle simulations indicate that the presence of a finite k_z can significantly change the threshold of EIH instability. The results are consistent with ALEXIS experiments.

(4) The nonlinear GeFi particle simulations of the EIH instability in a slab geometry and uniform plasma shows that in the nonlinear stage, the frequency is lower than that in the linear simulations. Structures in the real space show that the instability evolves from a short wavelength mode ($k\rho_i \sim 12$) to a longer wavelength mode ($k\rho_i \sim 3$). The nonlinear EIH instability deserves a further study.

Chapter 5

Nonlinear Parametric Decay Instability of Lower Hybrid Wave

Parametric Instability (PI), a multiple wave modes interaction process, is investigated in the nonlinear propagation of elestrostatic LHWs by utilization of GeFi kinetic particle simulation.

5.1 Introduction

Parametric instability of LHWs has been extensively analyzed due to great interest in *rf* heating of plasmas and current drive in fusion devices, such as tokamaks. Unlike Landau damping of LHWs, which is a wave-particle interaction process between LHWs and electrons and/or ions, PI is a wave-wave interaction process among multiple wave modes. Referring to the literatures on the theory of PI[63, 21, 19, 65, 64], a pump wave $(\omega_0, \mathbf{k_0})$, with frequency ω_0 near lower hybrid wave frequency ω_{LH} and wave vector $\mathbf{k_0}$, decays into two high frequency sidebands $(\omega_{1,2}, \mathbf{k_{1,2}})$, driven by a low frequency mode $(\omega, \mathbf{k})$ from various decay channels. Here $\omega_{1,2} = \omega \pm \omega_0, \mathbf{k_{1,2}} = \mathbf{k} \pm \mathbf{k_0}$ are the selection rules determined by momentum and energy conservation of the coupled modes (subscripts 1, 2 refer to the lower and upper sidebands, respectively).

The theory of PI of electrostatic LHWs has been studied in great details. PI of LHWs has also been observed in some lower hybrid current drive (LHCD) experiments[67, 66]. It has been demonstrated that PI plays important roles in LHCD with spectral broadening of LHWs in the experiments. However, the experimental study of PI still has much more to accomplish in the future work. Few kinetic simulation literatures have been published on PI of LHWs. Computational simulation is one of the most

advanced tools to study complicate nonlinear physics. Thus it is of great interest to investigate PI of LHWs by taking benefits of GeFi kinetic particle simulations.

5.2 GeFi Simulation of Parametric Instability of LHWs

Basic idea of the PI simulation is to drive a LHW with $(\omega_0, \mathbf{k_0})$ (pump wave) in a homogeneous plasma in a slab geometry, and observe the time evolution of the pump LHW. The pump wave decays, and some other wave modes in the system can be excited and grow up. One of the growing wave modes should be identified as the low frequency mode with $(\omega, \mathbf{k})$, and one of the other growing wave modes could be identified as either the lower sideband $(\omega_1, \mathbf{k_1})$ or the upper sideband $(\omega_2, \mathbf{k_2})$, with $(\omega_1 = \omega - \omega_0, \mathbf{k_1} = \mathbf{k} - \mathbf{k_0})$ and $(\omega_2 = \omega + \omega_0, \mathbf{k_2} = \mathbf{k} + \mathbf{k_0})$ being the selection rules. Note that in our previous simulations on the Landau damping of LHWs, the initial value problem was solved, and thus the LHW was driven only once at the beginning of the simulation. Here, in the simulations of PI of LHWs, the pump LHW is driven constantly all through the simulation time.

Simulations are performed in a uniform plasma with an external static magnetic field in x direction. Simulation model is complicated since the PI requires 3 dimensional (3-D) simulations in the space and various decay channels can exist. The pump LHW is placed to propagate in x and z directions, that is $\mathbf{k_0} = k_{0x}\mathbf{e_x} + k_{0z}\mathbf{e_z}$ with $k_{0y} = 0$. But for the low frequency wave mode or the sidebands, they usually have finite wave vectors in x, y, z directions, $\mathbf{k} = k_x\mathbf{e_x} + k_y\mathbf{e_y} + k_z\mathbf{e_z}$ and $\mathbf{k_{1,2}} = k_{1,2x}\mathbf{e_x} + k_{1,2y}\mathbf{e_y} + k_{1,2z}\mathbf{e_z}$. Thus 3-D simulations in the space are required. Moreover, the pump wave is allowed to decay into all kinds of possible wave modes, thus resolutions (grids number) in all three directions should be large enough to exclude the numerical inaccuracy. The large grid numbers in 3 directions require huge amount of simulation time, and data files' sizes are very large as well. It is difficult to analyze enough data files to plot time evolutions and frequencies of wave modes.

Various decay channels allow not only one decay process to occur in one single simulation. This makes it even more difficult to analyze different wave modes in the system and to identify the sidebands and the low frequency mode. Originally, it is expected to find either the lower or the upper sideband and the low frequency mode of the pump wave. However, the sidebands may not be able to be observed, since they can be subjected to another different PI process, following another decay channel to dump away before growing up. This kind of similar processes could possibly occur many times. Finally, several wave modes may grow up, however we may not be able to identify any of them to be the sidebands.

As discussed in the previous chapters, LHWs can decay due to direct wave-particle Landau interactions. In order to exclude Landau damping from damping sources, it is necessary to select a pump wave, which cannot satisfy the Landau damping condition. This is to make sure that the damping source is only the PI process. According to the discussions in the above paragraph, although it may be unable to identify the exact corresponding sidebands and low frequency mode in PI, the conclusion, that PI process is the only mechanism for the decay of the pump LHW, can then be drawn.

Mode number $\mathbf{m}$ instead of wave number $\mathbf{k}$ is used to describe different wave modes. Let the simulation domain length be l for a 1-D simulation, then $m = k/(2\pi/l)$ is the equation to convert wave number to mode number in simulations. Therefore, for a pump wave with $(\omega_0, \mathbf{m_0})$, and a low frequency mode with $(\omega, \mathbf{m})$, the lower sideband and upper sideband should be $(\omega_1, \mathbf{m_1} = \mathbf{m} - \mathbf{m_0})$ and $(\omega_2, \mathbf{m_2} = \mathbf{m} + \mathbf{m_0})$ as the selection rules. Since GeFi kinetic simulations of PI of LHWs are 3-D, the mode number has three components $\mathbf{m} = (m_x, m_y, m_z)$.

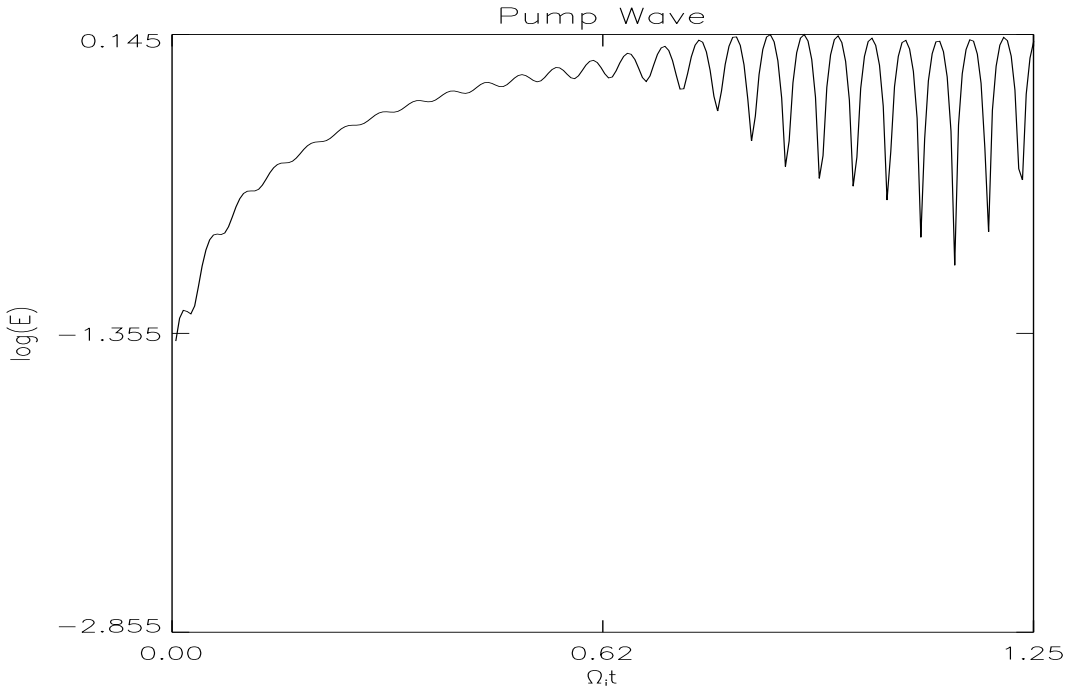

Figure 5.1: Time evolution of the Fourier electric field of the pump wave in a single mode simulation.

5.2.1 Single Mode simulation of Pump Wave

As discussed above, it is necessary to exclude the direct wave-particle Landau damping of the pump LHW from damping sources. A single mode simulation is that all the other wave modes except the pump wave mode in the simulation system are filtered, as in the simulations of Landau damping of LHWs.

The selected pump LHW has wave vector $\mathbf{k_0}\rho_e = (0.004, 0.0, 0.08746)$, thus $k_{0\|}\rho_e = 0.004$ and $k_{0\perp}\rho_e = 0.08746$, where ρ_e is the electron gyro-radius. From Eq. 1.27, the frequency of this pump wave is calculated to be $\omega_0 = 66.77\Omega_i = 2.207\omega_{LH}$. Ion-electron mass ratio $m_i/m_e = 1836$, ion-electron temperature ratio $T_i/T_e = 1.0$, light-Alfvèn speed ratio $c/V_A = 42.8$, external static magnetic field's magnitude is set to be 1.0, electron thermal speed $V_{the} = 1.0$. By these parameters, we have $\omega_{pi} = 42.8\Omega_i$, $\omega_{pe} = 1836\Omega_i$, $\Omega_e = 1836\Omega_i$, and thus $\omega_{LH} = 30.26\Omega_i$.

Figure 5.1 shows the plot of time evolution of Fourier electric field of the pump wave in a single mode simulation. As it is seen from the figure that the amplitude

of the pump wave grows up gradually due to the constantly driving source. After a certain time, the amplitude of the wave saturates down to a constant value due to the nonlinear effects. The pump wave does not decay after the saturation. In other words, there are no or few wave-particle Landau interactions in the propagation of pump wave. Thus this pump LHW is good for PI simulation to exclude the Landau damping from the damping sources. Real frequency of the pump wave from GeFi kinetic simulation is measured to be $\omega_{0s} = 67.88\Omega_i = 2.24\omega_{LH}$, which has a good agreement with the theoretical predication.

5.2.2 GeFi simulation of PI of LHWs

Case 1

Pump LHW with $\mathbf{k_0}\rho_e = (0.004, 0.0, 0.08746)$ is driven constantly in plasmas. Mode number of the pump wave is set to be $\mathbf{m_0} = (4, 0, 4)$. In y direction, a wave vector with $k_y\rho_e = 0.09$ is set to have mode number $m_y = 4$. In the simulation system, all wave modes with mode numbers larger than $(8, 8, 8)$ in any of the three dimensions are filtered. In other words, Only wave modes with $|m_x| \leq 8$ and $|m_y| \leq 8$ and $|m_z| \leq 8$ are allowed to exist in the simulation system. Since in the simulation, waves can propagate in both positive and negative directions, negative wave modes are also present. Therefore, there exist totally $17 \times 17 \times 17 = 4913$ (zero modes included) wave modes in the simulation system.

To be different from the simulations of Landau damping of LHWs, where the initial value problems were solved, here pump LHWs are driven constantly. It is seen from Fig. 5.1, it takes a while for the pump wave to saturate. Thus the strategy of the simulation here is the following. Before the saturation of the pump wave, a single mode simulation is performed. After the pump wave is saturated, other wave modes with mode numbers less than $(8, 8, 8)$ are then allowed in the simulation system. Taking this pump LHW as an example, only the pump wave mode exists in

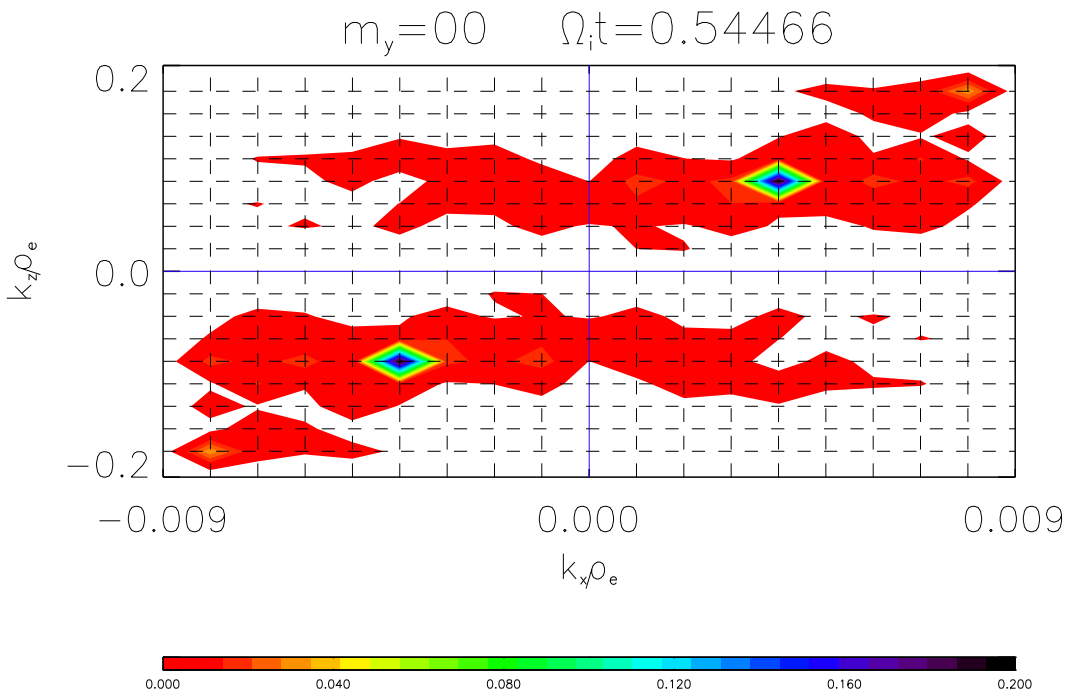

Figure 5.2: Contour plot of the electric field in the (k_x, k_z) space with the mode number in y direction m_y being 0.

the system before $\Omega_i t = 0.5$, and when $\Omega_i t \geq 0.5$ all the wave modes smaller than $(8, 8, 8)$ are allowed to exist.

In order to find out growing wave modes with the largest amplitudes, contour plots of electric field in **k** space are necessary. Since there are three dimensions, mode numbers in y direction m_y are fixed, and contour plots in (k_x, k_z) space are made. Wave modes propagating in positive and negative directions are symmetric, thus it is only necessary to plot the positive m_y and all (m_x, m_z) pairs.

Figure 5.2 shows the contour plot of electric field in (k_x, k_z) space with $m_y = 0$. Vertical (horizontal) dashed lines indicate the mode numbers of m_x (m_z). For example, in the x direction, from the middle $k_x = 0$ ($m_x = 0$) to the right, $m_x = 1, 2, \cdots, 7, 8$ corresponding to the 8 vertical dashed lines, and to the left, $m_x = -1, -2, \cdots, -7, -8$. It can be seen from the figure that there exist two strong dark points that are symmetric, indicating presence of the pump wave with mode numbers $(4, 0, 4)$ (or the symmetric $(-4, 0, -4)$, here and through this chapter, we will not

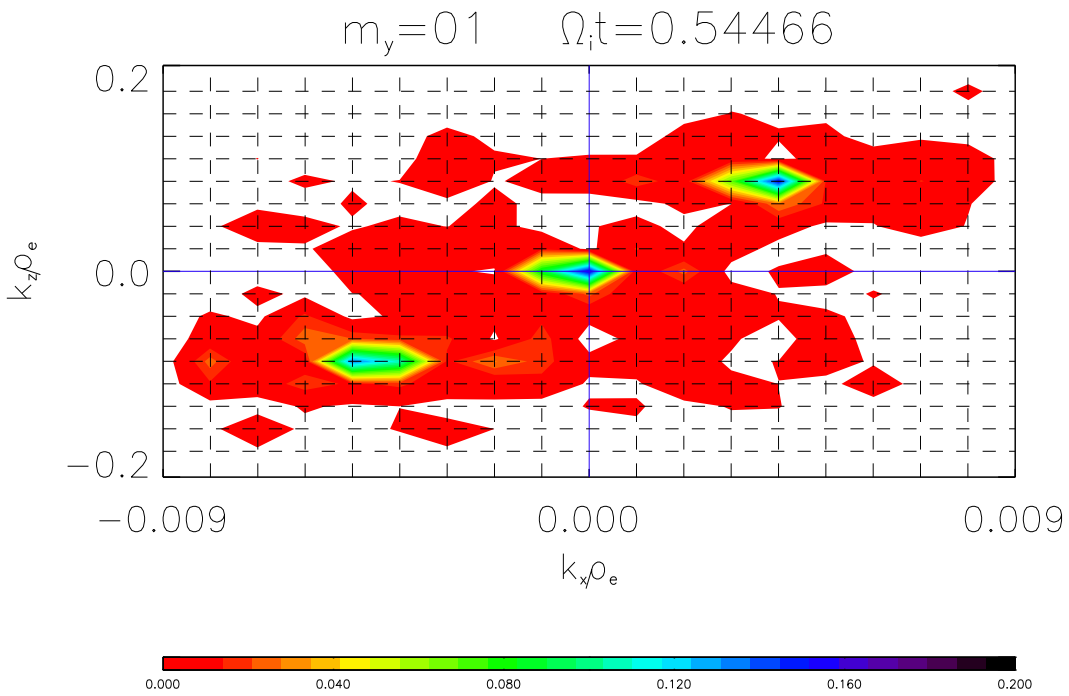

Figure 5.3: Contour plot of the electric field in the (k_x, k_z) space with the mode number in y direction m_y being 1. Wave modes with $(0, 1, 0)$, $(4, 1, 4)$ and $(-4, 1, -4)$ are found to have the largest amplitudes of electric field.

mention the symmetric mode numbers again). Red color in the figure indicates the presence of other wave modes with much smaller amplitude of electric field. In the same way, other wave modes with large amplitude of electric field can be found out by making similar plots for $m_y = 1, 2, \cdots, 7, 8$. By doing this, wave modes $(0, 1, 0)$ and $(4, 1, 4)$ are found to have the largest amplitudes of electric field, as shown in Fig 5.3.

Among all contour plots of electric field in (k_x, k_z) space with different k_y and time, fig 5.3 is found to have two strongest dark points, indicating that both wave modes $(0, 1, 0)$ and $(4, 1, 4)$ have the largest amplitude of electric field (except the pump wave). If both modes $(0, 1, 0)$ and $(4, 1, 4)$ are considered as the lower hybrid wave eigen modes, their eigen frequencies can be calculated from the dispersion equation (Eq. 1.27). The wave mode $(0, 1, 0)$ with wave vector $\mathbf{k_1}\rho_e = (0, 0.0225, 0)$ propagates perpendicular to the magnetic field, and has frequency $\omega = \omega_{LH} \simeq 30.26\Omega_i$.

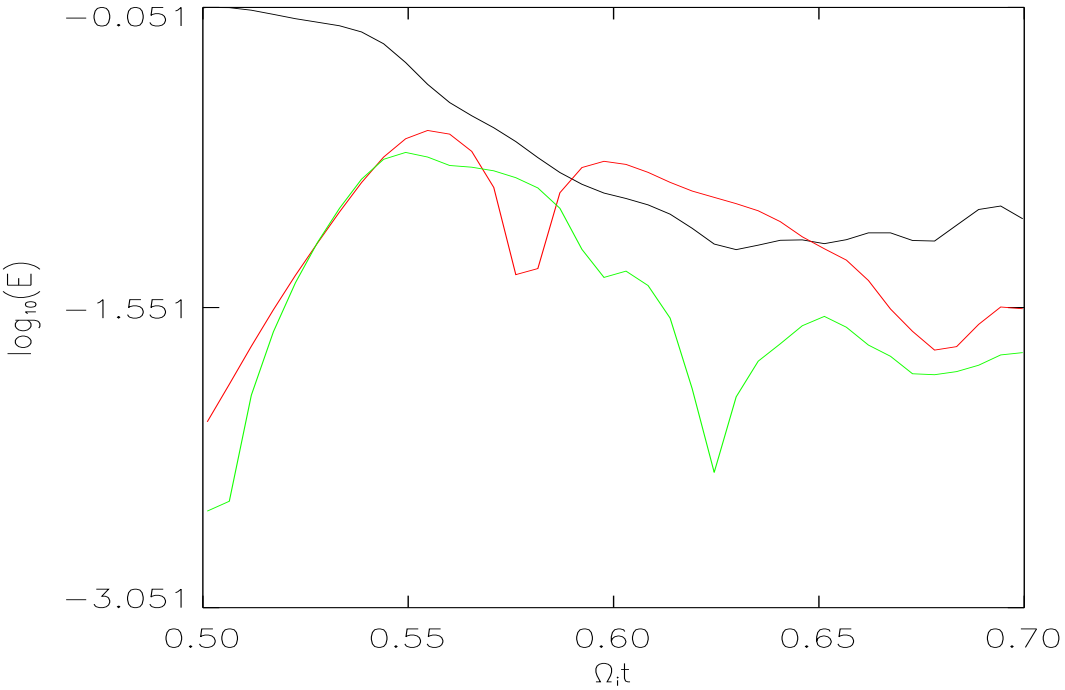

Figure 5.4: Time evolution of Fourier electric field of the 3 wave modes: pump wave $(4, 0, 4)$ (black line), wave mode $(0, 1, 0)$ (red line) and wave mode $(4, 1, 4)$ (green line).

The wave mode $(4, 1, 4)$ with wave vector $\mathbf{k}\rho_e = (0.004, 0.0225, 0.08746)$ is calculated to have frequency $\omega = 2.145\omega_{LH} \simeq 64.92\Omega_i$. Note that the frequencies calculated here are LHW eigen frequencies.

After wave modes with the largest growth amplitude are identified, time evolution of the wave modes are plotted, as shown in Fig. 5.4. The pump wave $(4, 0, 4)$ is depicted as black line; the wave mode $(0, 1, 0)$ is represented by red line; green line is the wave mode $(4, 1, 4)$. In the figure, it can be seen that the pump wave decays after the other wave modes are released in the system. The wave modes $(0, 1, 0)$ and $(4, 1, 4)$ grow up first, and then decay along with the pump wave. The whole process happens very fast within several lower hybrid wave periods. Apparently, wave vectors of the three wave modes can match up to be identified as parametric decay instability, that is $\mathbf{k_1} = \mathbf{k} - \mathbf{k_0}$. However, match of the three frequencies is also necessary to be investigated.

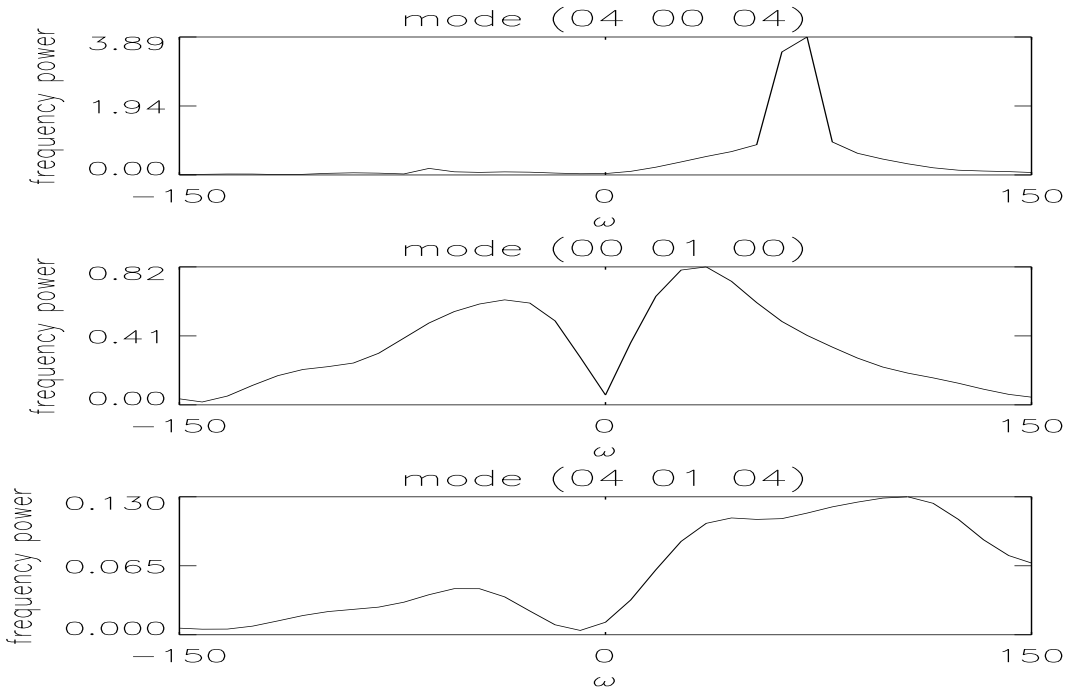

Figure 5.5: Frequencies of pump wave $(4, 0, 4)$, wave mode $(0, 1, 0)$ and wave mode $(4, 1, 4)$ from top to bottom.

Fig. 5.5 is plot of frequencies of pump wave $(4, 0, 4)$, wave mode $(0, 1, 0)$ and wave mode $(4, 1, 4)$ from top to bottom. The x axis is frequency, and the y axis is frequency power. From the plot of wave mode $(4, 0, 4)$, which is the pump wave, frequency can be measured to be $\omega_0 \simeq 68.44 = 2.262\omega_{LH}$, close to the theoretical predication. Frequency of wave mode $(0, 1, 0)$ can be estimated from the peak of the middle plot, $\omega_1 \simeq 30.94 = 1.02\omega_{LH}$, which is very close to its LHW eigen frequency. Wave mode $(0, 1, 0)$ is identified to be a lower hybrid wave since its frequency analysis indicates that it possesses lower hybrid wave eigen frequency. In the bottom plot of Fig. 5.5, the pulse is not obvious, however the measurement of the largest peak yields a frequency $\omega = 101.25\Omega_i = 3.346\omega_{LH}$. It can be seen that frequencies of the 3 wave modes can match up as well, $\omega_1 \simeq \omega - \omega_0$.

From analysis in $\mathbf{k}$ space and frequencies, the following conclusion can be drawn. A constantly driven pump wave with $\mathbf{k_0}\rho_e = (0.004, 0, 0.08746)$ and frequency $\omega_0 \simeq 2.24\omega_{LH}$ decays in to a lower hybrid wave mode $(0, 1, 0)$ with $\mathbf{k_1}\rho_e = (0, 0.0225, 0)$ and

frequency $\omega_1 \simeq 1.02\omega_{LH}$, and a wave mode $(4, 1, 4)$ with $\mathbf{k}\rho_e = (0.004, 0.0225, 0.08746)$ and frequency $\omega \simeq 3.346\omega_{LH}$. This decay process is identified as a parametric decay instability from the aspect of selection rules of wave vectors $\mathbf{k_1} = \mathbf{k} - \mathbf{k_0}$ and frequencies $\omega_1 = \omega - \omega_0$.

In the bottom plot of Fig. 5.5, the largest peak is measured as the frequency of the wave mode ω, while at the left of the peak, there is a broad frequency spectrum in the range $[36, 101]\Omega_i$. Explanation of this smaller frequency is the following. In this broad spectrum, there might be a frequency as the lower hybrid wave eigen frequency of wave mode $(4, 1, 4)$, which is about $64.92\Omega_i$. In the parametric instability simulation and with an ideal condition, the eigen frequency of mode $(4, 1, 4)$ should not be observed in the analysis. However, due to limited simulation time and limited datas used in FFT and the fact that wave mode $(4, 1, 4)$ grows up and damps away within several lower hybrid wave periods, the decay wave mode frequency ($\omega = 3.346\omega_{LH}$) cannot obtain so large a power to completely dominate the eigen frequency of the wave mode in the analysis. In the broad spectrum there is another frequency which should be about $36.94\Omega_i$. This frequency is also from parametric instability process with the same mode $(0, 1, 0)$, but the negative frequency of this mode. It can be seen in the frequency plot of mode $(0, 1, 0)$ in Fig. 5.5, the wave mode has a negative frequency about $\omega_1' = -30.26\Omega_i$. By the selection rules of frequency, $\omega_1' = \omega - \omega_0$, wave mode $(4, 1, 4)$ should have a frequency $\omega = 36.94\Omega_i$. Thus, wave mode $(4, 1, 4)$ might have 3 frequencies $36.94\Omega_i$, $64.92\Omega_i$ and $101.25\Omega_i$. Since the time range of analysis is short, less than $1/\Omega_i$, the resolution of frequency analysis is about $10\Omega_i$. Thus it is not difficult to understand why the frequency pulses in the frequency spectrum of wave mode $(4, 1, 4)$ are not well formed.

The decay channel of this case is also identified. In this simulation case, $k_\parallel V_{te}/\omega = 0.13 < 0.3$, thus it falls in "Case A" discussed in Secthion 1.4.2. And $\omega_0 = 2.26\omega_{LH} > 2\omega_{LH}$, thus the decay channel is identified as that a pump wave decays into two lower

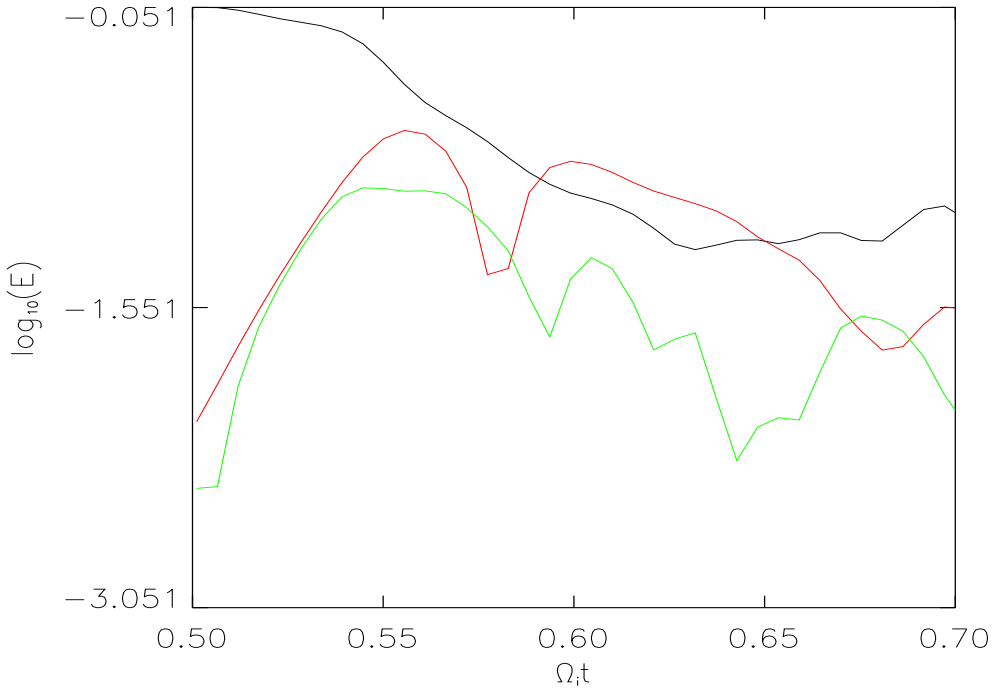

Figure 5.6: Time evolution of Fourier electric field of the 3 wave modes: pump wave $(4, 0, 4)$ (black line), wave mode $(0, 1, 0)$ (red line) and wave mode $(-4, 1, -4)$ (green line).

hybrid waves. From Eq. 1.73, the growth rate in the absence of damping can be estimated to obtain $\gamma_{0t}/\Omega_i \simeq 27.71$. Growth rate in the simulation case is estimated to be $\gamma_{0s}/\Omega_i \simeq 33.61$, which has a good agreement with the theory estimation.

Besides wave modes $(0, 1, 0)$ and $(4, 1, 4)$, it is found that there also exist some other wave modes with very large amplitude of electric field in the simulation system. Take a look at Fig. 5.3 again, there is another highlight black spot at mode $(-4, 1, -4)$. Note that $(-4, 1, -4)$ is not the symetric mode of $(4, 1, 4)$ (its symmetric mode is $(-4, -1, -4)$). Time evolution of Fourier electric field of wave modes $(4, 0, 4)$, $(0, 1, 0)$ and $(-4, 1, -4)$ are plotted in Fig. 5.6 and their respective frequency spectrum is plotted in Fig. 5.7. Denote $(\omega_0, \mathbf{k_0})$, $(\omega_1, \mathbf{k_1})$ and $(\omega, \mathbf{k})$ as wave modes (4,0,4), (0,1,0) and (-4,1,-4), respectively. The selection rules of frequency and wave vectors are $\omega = \omega_1 - \omega_0$ and $\mathbf{k} = \mathbf{k_1} - \mathbf{k_0}$. Rest of the analysis is similar to that above.

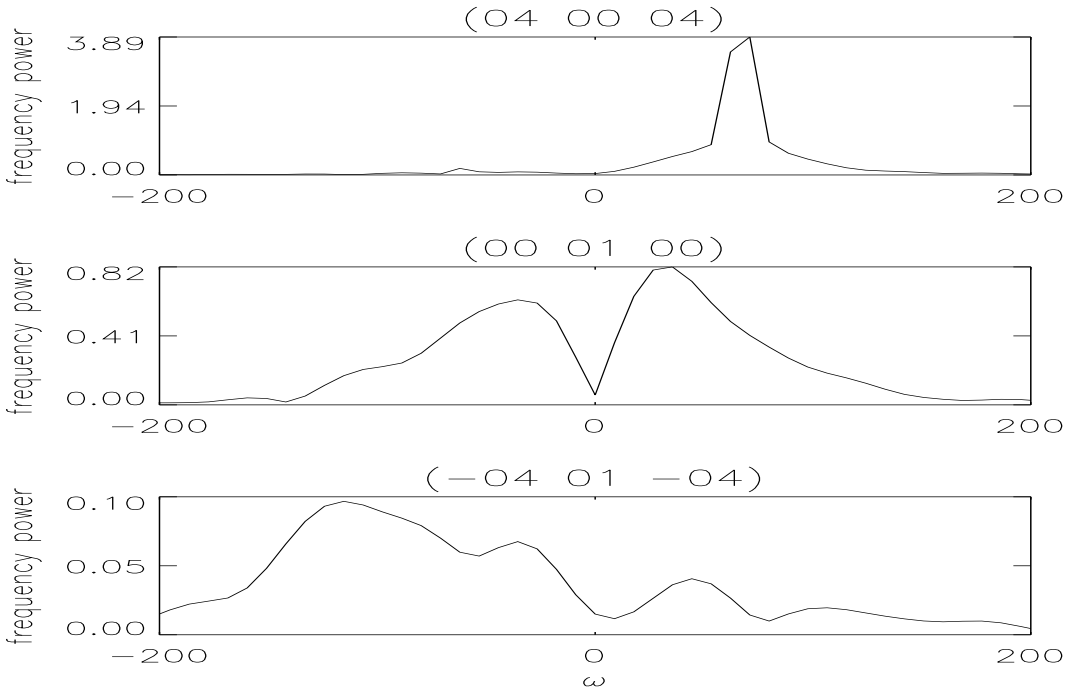

Figure 5.7: Frequencies of pump wave $(4, 0, 4)$, wave mode $(0, 1, 0)$ and wave mode $(-4, 1, -4)$ from top to bottom.

Analysis of wave modes in **k** space also shows some other wave modes with a little smaller but still large amplitudes of electric field. Fig. 5.8 shows the contour plot in (k_x, k_z) space with mode number $m_y = 2$. Three highlight spot are found in the figure at wave modes $(0, 2, 0)$, $(4, 2, 4)$ and $(-4, 2, -4)$. Time evolution and frequency spectrum of these 3 wave modes with the pump wave are plotted in Fig. 5.9 and Fig. 5.10, respectively. Analysis and discussion of these modes by selection rules in frequencies and wave vectors are the same as that above.

Case 2

In case 2, pump LHW has wave vector $\mathbf{k_0}\rho_e = (0.008, 0.000, 0.08746)$, thus the eigen frequency of this wave is $\omega_0 = 122.34\Omega_i = 4.045\omega_{LH}$ from the dispersion relation of LHWs. The pump wave is also set up at wave mode $(4, 0, 4)$. All the other wave modes are filtered until $t\Omega_i \geq 0.5$, when the pump wave is about saturated, wave

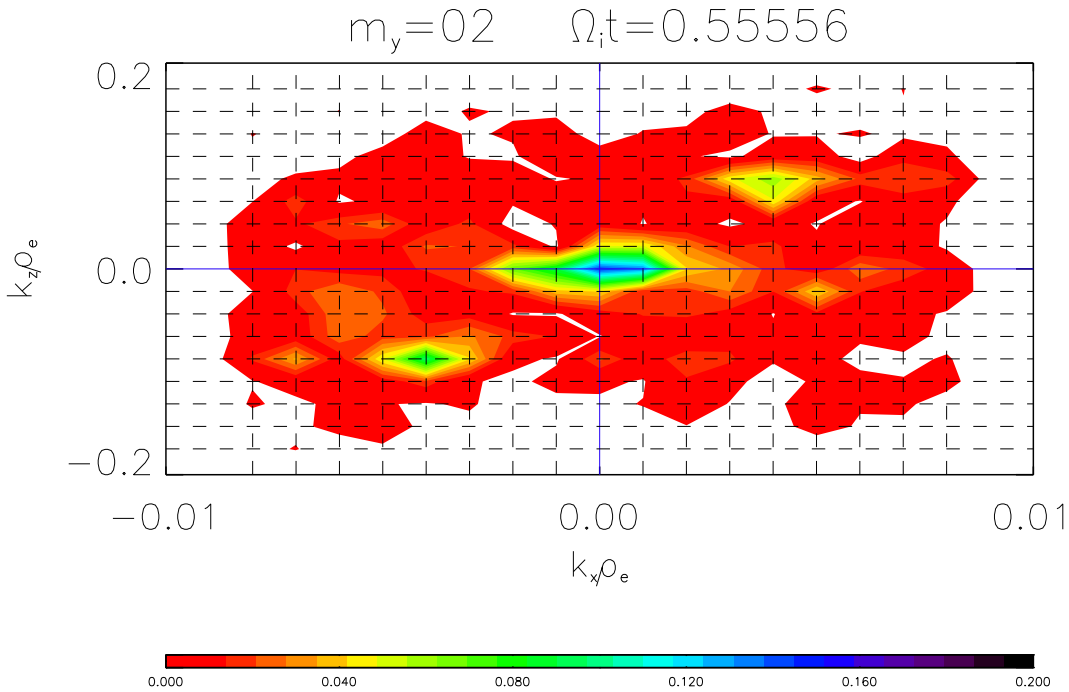

Figure 5.8: Contour plot of the electric field in (k_x, k_z) space with mode number in y direction m_y being 2. Wave modes with $(0, 2, 0)$, $(4, 2, 4)$ and $(-4, 2, -4)$ are found to have the largest amplitudes of electric field.

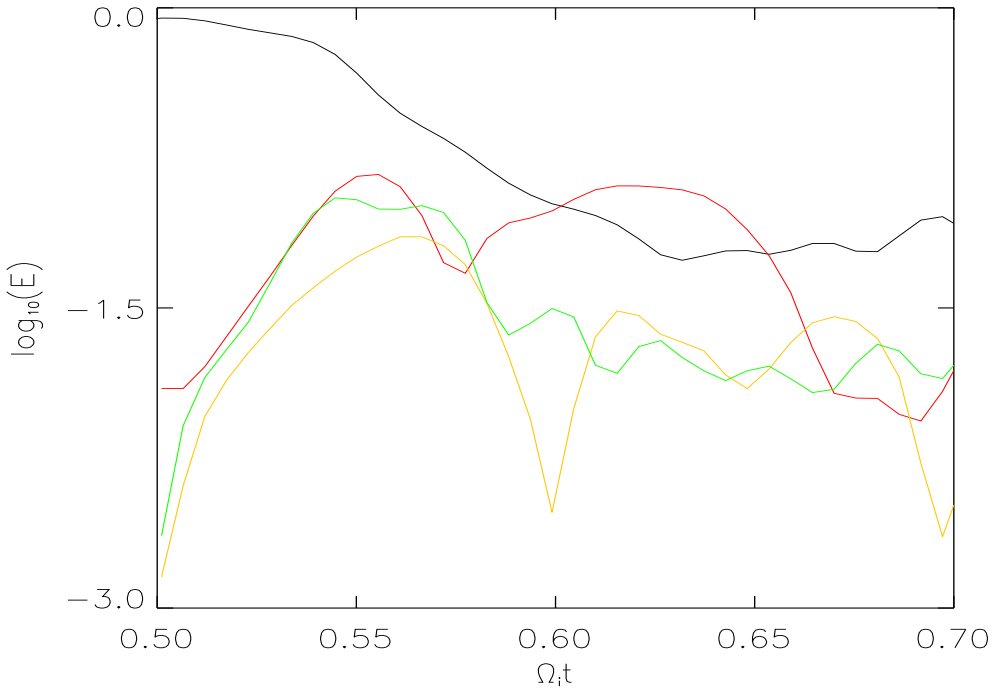

Figure 5.9: Time evolution of Fourier electric field of the 4 wave modes: pump wave $(4, 0, 4)$ (black line), wave mode $(0, 2, 0)$ (red line), wave mode $(4, 2, 4)$ (yellow line) and wave mode $(-4, 2, -4)$ (green line).

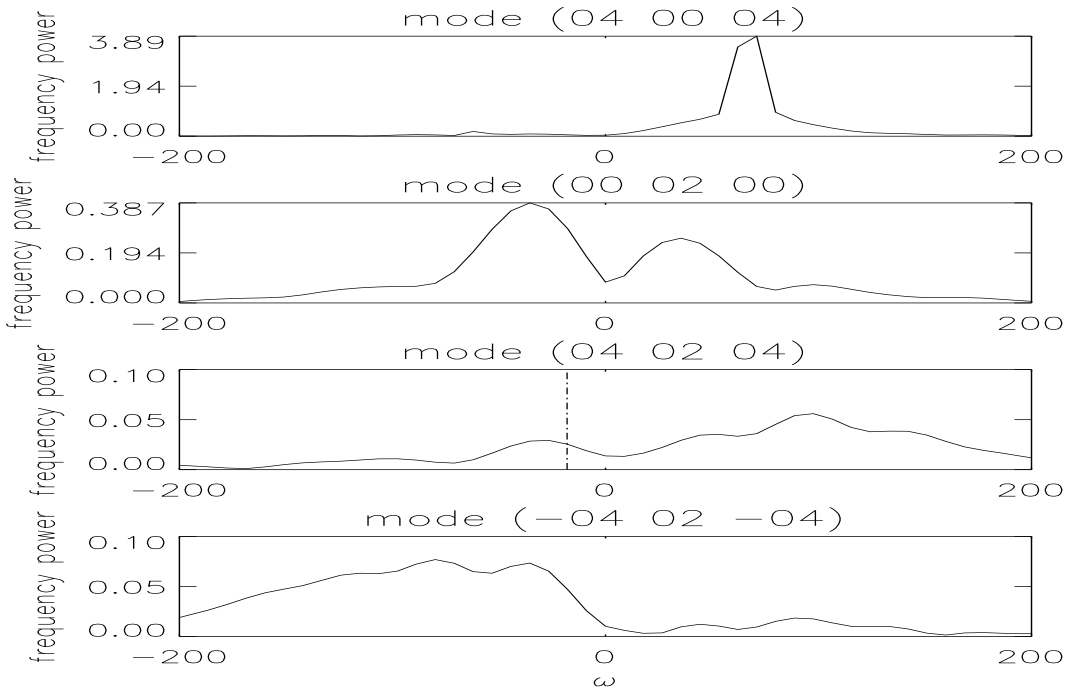

Figure 5.10: Frequencies of pump wave $(4, 0, 4)$, wave mode $(0, 2, 0)$, wave mode $(4, 2, 4)$ and wave mode $(-4, 2, -4)$ from top to bottom.

modes with mode number less than $(8, 8, 8)$ are then allowed to exist in the simulation system.

Analysis of Fourier electric field in (k_x, k_z) space shows that wave modes $(0, 3, 1)$, $(4, 3, 5)$ and $(-4, 3, -3)$ have large amplitude as the highlight spots in Fig. 5.11. Since electric fields of wave modes are oscillating, they may not be observed at a time due to small value at the trough of the oscillations, but they do exist in the simulation system and can be observed some other times when they reach the crest of the oscillations. Figs. 5.12 and 5.13 are contour plots in (k_x, k_z) space at $\Omega_i t = 0.58824$ and $\Omega_i t = 0.54466$, respectively. In the figures, wave modes $(1, 3, 0)$, $(-1, 3, 0)$, $(5, 3, 4)$ and $(-5, 3, -4)$ are found to have large amplitudes.

Time evolutions and frequency spectrums of these wave modes are then plotted. Figs. 5.14 and 5.15 are plots of time evolution and frequency spectrum of modes $(4, 0, 4)$, $(0, 3, 1)$, $(4, 3, 5)$ and $(-4, 3, -3)$. Figs. 5.16 and 5.17 are plots of time evolution and frequency of modes $(4, 0, 4)$, $(1, 3, 0)$ and $5, 3, 4$. Figs. 5.18 and 5.19 are

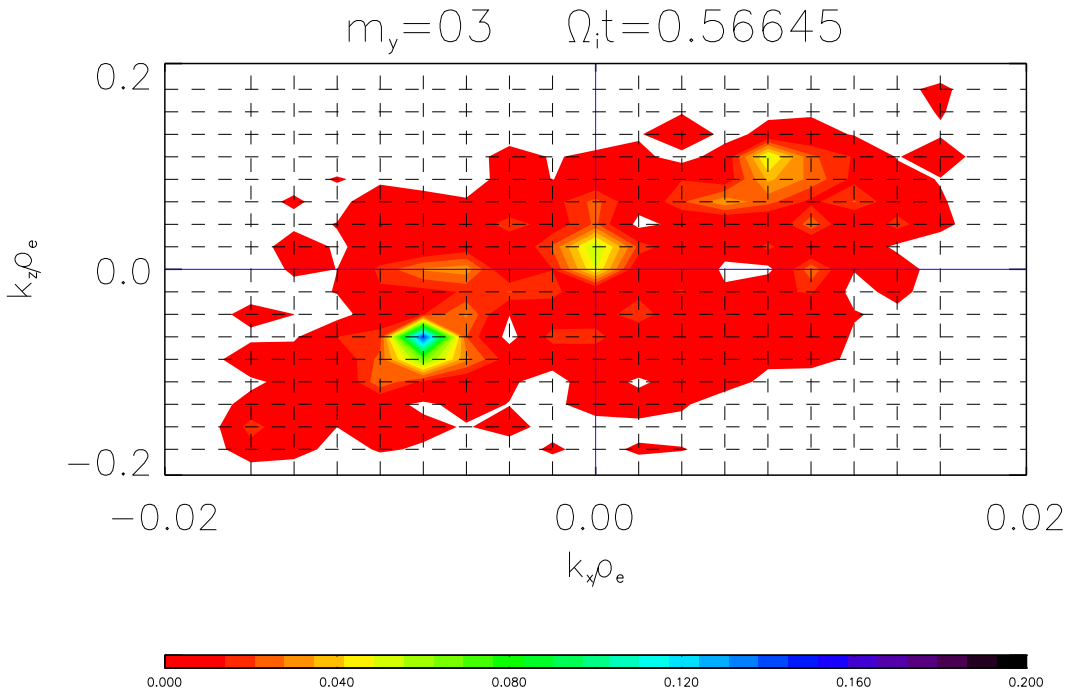

Figure 5.11: Contour plot of the electric field in (k_x, k_z) space with mode number in y direction $m_y = 3$. Wave modes with $(0, 3, 1)$, $(4, 3, 5)$ and $(-4, 3, -3)$ are found to have the largest amplitudes of electric field.

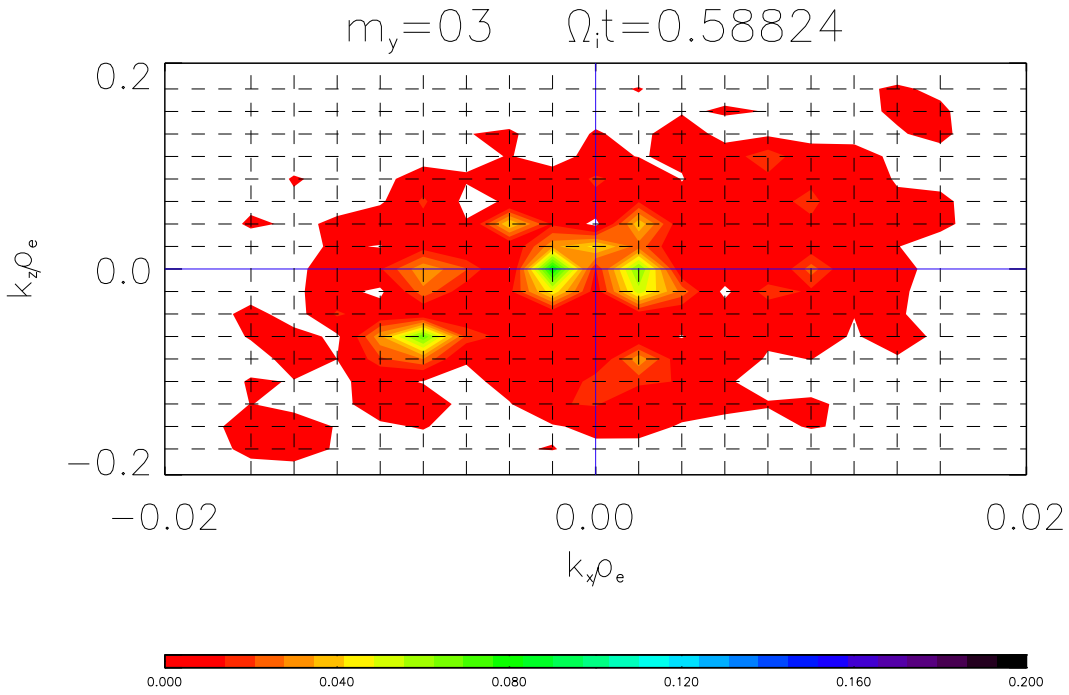

Figure 5.12: Contour plot of the electric field in (k_x, k_z) space with mode number in y direction $m_y = 3$ at $\Omega_i t = 0.58824$. Wave modes $(1, 3, 0)$ and $(-1, 3, 0)$ are found to have large amplitudes of electric field.

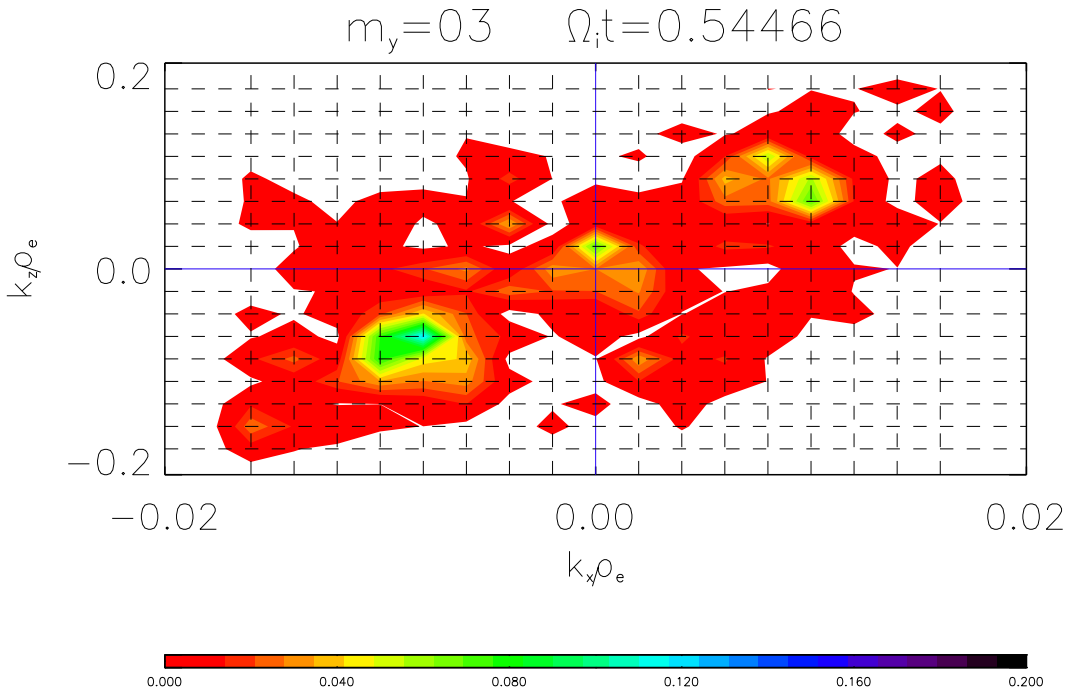

Figure 5.13: Contour plot of the electric field in (k_x, k_z) space with mode number in y direction $m_y = 3$ at $\Omega_i t = 0.54466$. Wave modes with $(5, 3, 3)$ and $(-5, 3, -3)$ are found to have large amplitudes of electric field.

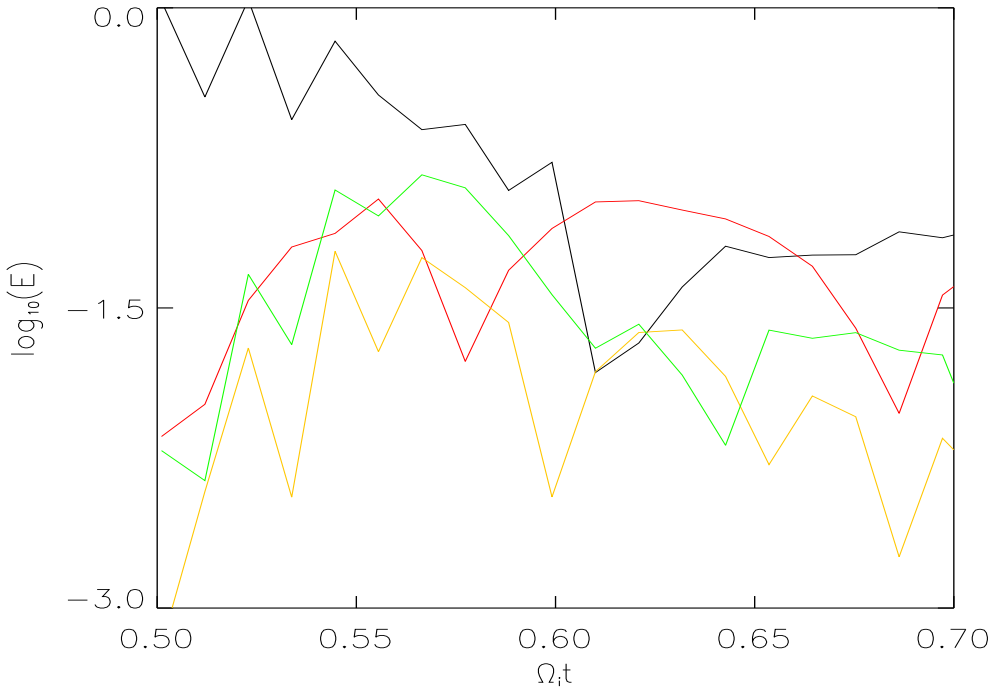

Figure 5.14: Time evolution of Fourier electric field of the 4 wave modes: pump wave $(4, 0, 4)$ (black line), wave mode $(0, 3, 1)$ (red line), wave mode $(4, 3, 5)$ (yellow line) and wave mode $(-4, 3, -3)$ (green line).

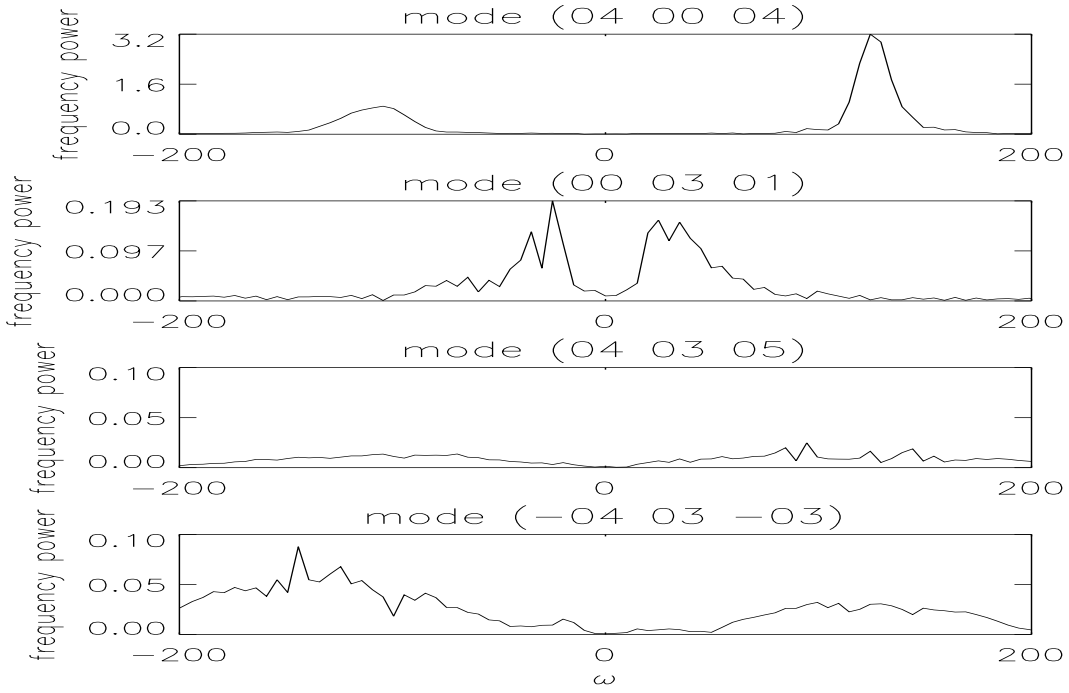

Figure 5.15: Frequencies of pump wave $(4, 0, 4)$, wave mode $(0, 3, 1)$, wave mode $(4, 3, 5)$ and wave mode $(-4, 3, -3)$ from top to bottom.

similar plots for modes $(4, 0, 4)$, $(-1, 3, 0)$ and $-5, 3, -4$. Analysis of these wave modes by the selection rules of wave vectors and frequencies, for the purpose of momentum and energy conservation, are similar to that in case 1. Some wave modes, such as $(4, 3, 5)$, $(5, 3, 4)$ and $(-5, 3, -4)$, have small frequency power. However in their time evolution plots, it can be seen that their peak values of electric field amplitude are as large as other wave modes with much larger frequency power. The explanation for this is that although wave modes $(4, 3, 5)$, $(5, 3, 4)$ and $(-5, 3, -4)$ have large peak values of electric field amplitude, they grow up and damp away very fast, within about $0.1/\Omega_i$. The short time existence of those wave modes causes low frequency power in their frequency spectrums.

5.2.3 Particles distribution in PI simulation

Although wave-wave interaction plays the most important role in the PI process of LHWs, it is also of great interest to study electons and ions distributions in the

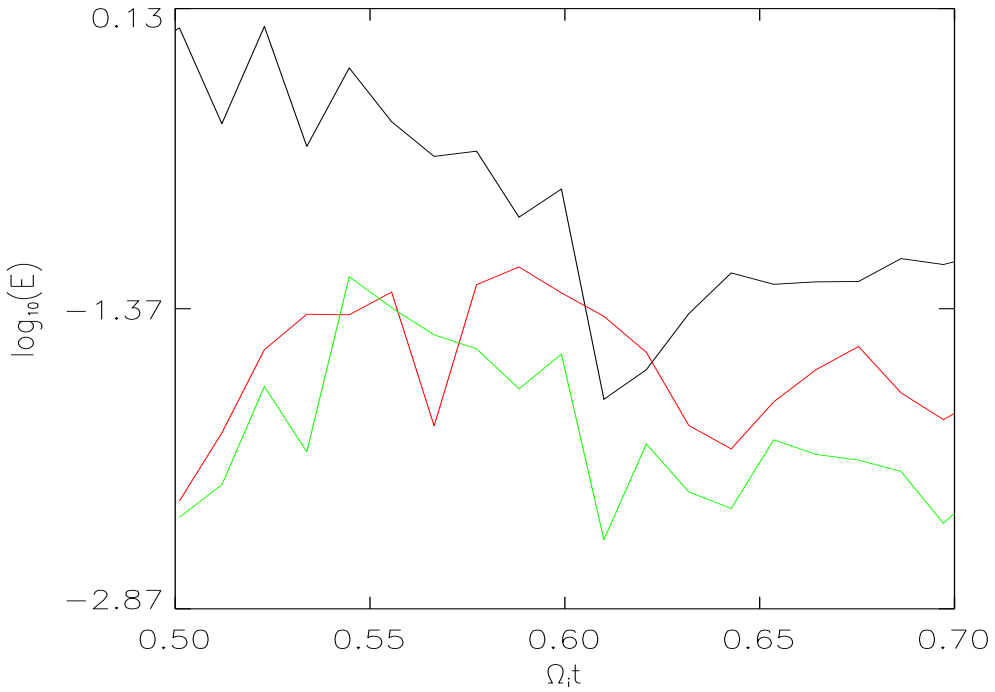

Figure 5.16: Time evolution of Fourier electric field of 3 wave modes: pump wave $(4, 0, 4)$ (black line), wave mode $(1, 3, 0)$ (red line), and wave mode $(5, 3, 4)$ (green line).

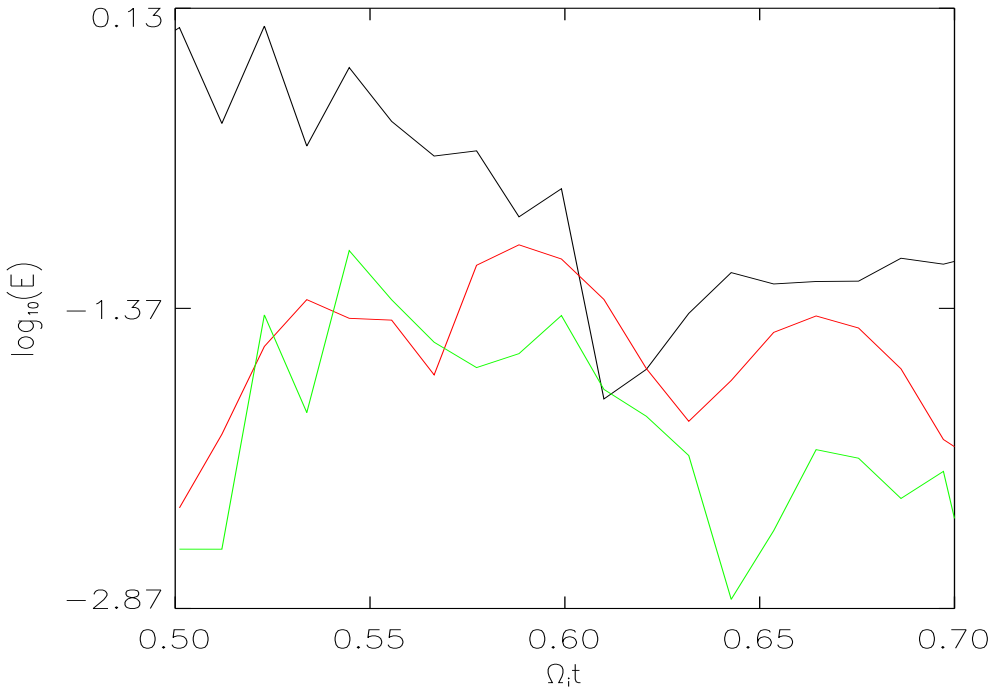

Figure 5.17: Time evolution of Fourier electric field of 3 wave modes: pump wave $(4, 0, 4)$ (black line), wave mode $(-1, 3, 0)$ (red line), and wave mode $(-5, 3, -4)$ (green line).

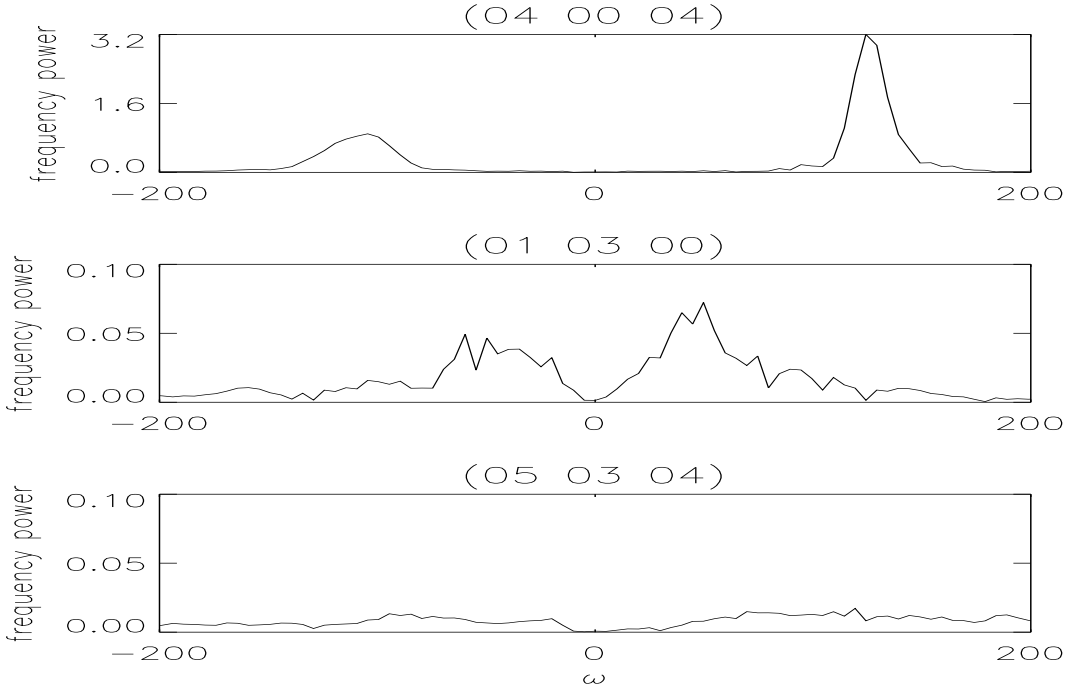

Figure 5.18: Frequencies of pump wave $(4, 0, 4)$, wave mode $(1, 3, 0)$ and wave mode $(5, 3, 4)$ from top to bottom.

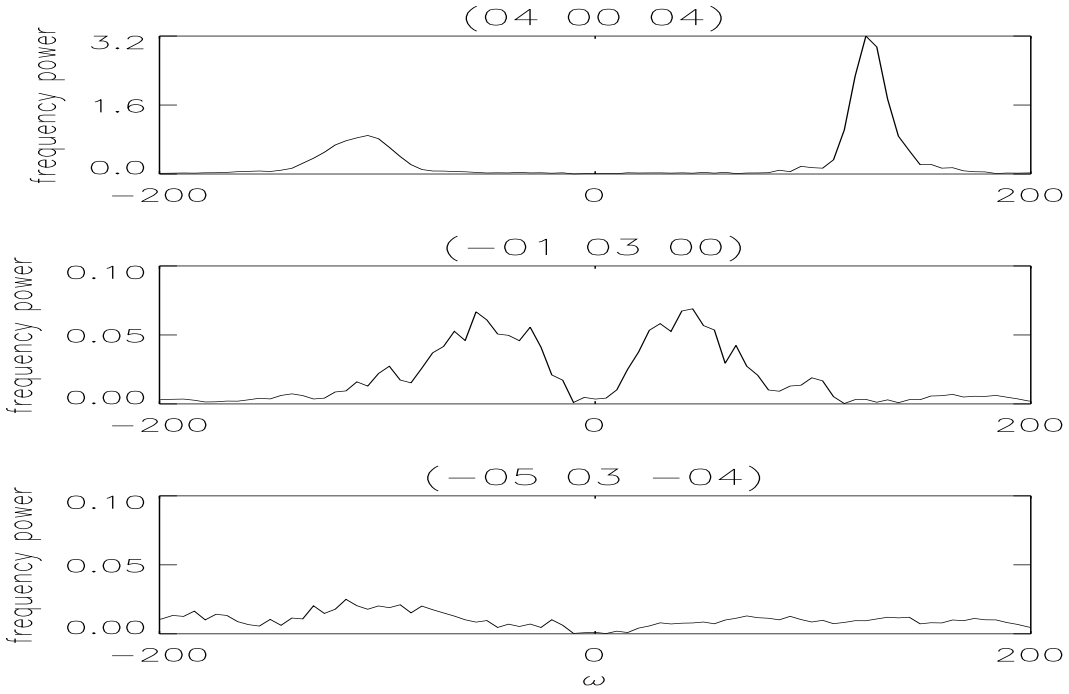

Figure 5.19: Frequencies of pump wave $(4, 0, 4)$, wave mode $(-1, 3, 0)$ and wave mode $(-5, 3, -4)$ from top to bottom.

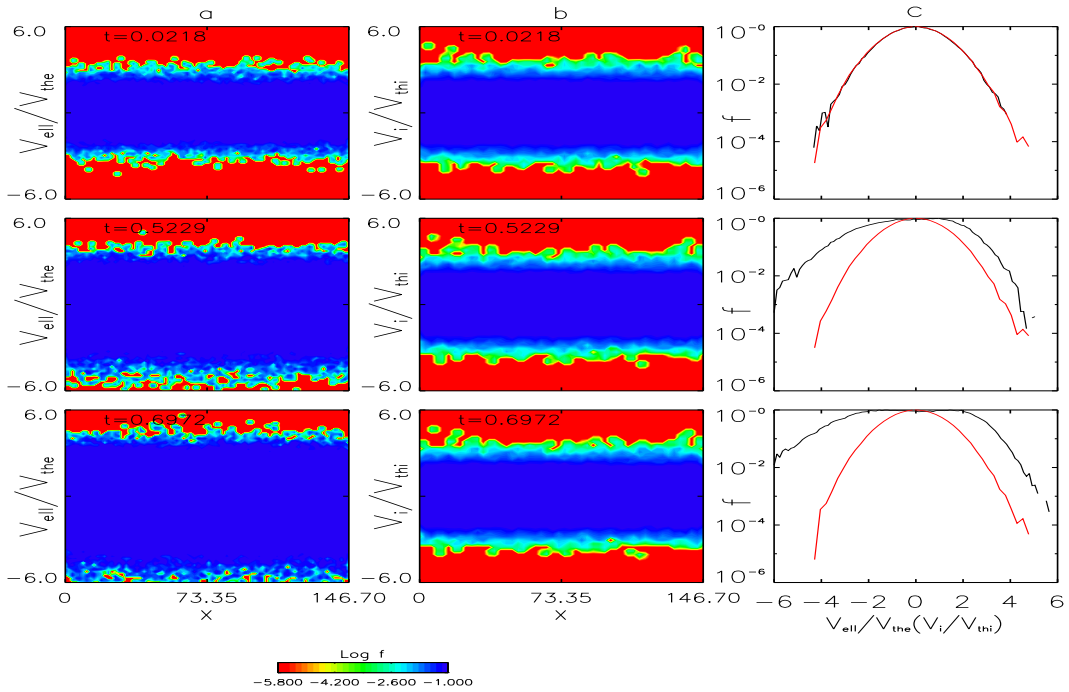

Figure 5.20: Time evolution of electron and ion distributions in Case 1 for $\Omega_i t = 0.0218$ (top), $\Omega_i t = 0.5229$ (middle), $\Omega_i t = 0.6972$ (bottom). Column (a) is electron distribution in phase space $(V_{e\|}, x)$. (b) is ion distribution in phase space (V_i, x). (c) are plots of electron (solid lines) and ion (red lines) distribution functions.

process. Wave-particle interactions change velocity distributions of particles, as presented in the Landau damping of LHWs. The change of the velocity distributions of particles may in turn modify the characteristics of wave modes in the simulation system. Thus it is necessary and interesting to investigate velocity distributions of particles along with properties of wave modes.

Both electron and ion distributions in Case 1 are investigated in phase space and their respective velocity distribution functions at different time in Fig. 5.20. In the figure, column (a) and column (b) are contour plots of electron distribution in phase space $(V_{e\|}, x)$ and contour plots of ion distribution in phase space (V_i, x), respectively. Ion (solid lines) and electron (red lines) velocity distribution functions are plotted in column (c). Electron velocity is normalized to electron thermal speed V_{the}, and ion velocity is normalized to ion thermal speed V_{thi}. From top to bottom, $\Omega_i t = 0.0218$, $\Omega_i t = 0.5229$ and $\Omega_i t = 0.6972$. Note that in Case 1, $\Omega_i t = 0.5$ is

the time when the simulation system is released, and other wave modes besides the pump wave are allowed to exist in the system. It can be seen from column (a) that electrons are heated at time $\Omega_i t = 0.5229$ and $\Omega_i t = 0.6972$. Lots of electrons move to higher velocity region, especially electrons with negative velocities. In column (b), it is seen that the blue structure does not expand to higher velocity region, thus ions are not heated. In velocity distribution functions in column (c), electron distribution function, depicted as black lines, expands at the tail, especially in negative velocity part, while ion distribution function is unchanged as seen from red curves. This change in electron parallel velocity distribution may in turn affect properties of the wave modes. For example, the expected low frequency modes $\omega, \mathbf{k}$ in either Case 1 or Case 2 have large frequencies rather than low frequency ($\sim \Omega_i$). Large frequencies of the expected low frequency modes may be excited by the alteration of electron distribution.

5.3 Summary

In this chapter, parametric instability of LHWs is studied by utilization of GeFi kinetic simulation. A constantly driven source in a uniform plasma is used to generate a pump LHW with wave vector $\mathbf{k_0}$ and frequency ω_0. Single mode simulation shows that the pump LHW saturates at a constant amplitude after some time. In PI simulations, the pump LHW is allowed to grow to saturation as a single mode before other wave modes, with mode numbers smaller than $(8, 8, 8)$, are allowed to exist in simulation system. In either Case 1 or Case 2, the pump LHW is found to decay into a lower sideband lower hybrid wave $(\mathbf{k_1}, \omega_1)$ and an expected low frequency wave mode $(\mathbf{k}, \omega)$. The three waves satisfy the selection rule in both wave vectors and frequencies, $\mathbf{k_1} = \mathbf{k} - \mathbf{k_0}$ and $\omega_1 = \omega - \omega_0$, or $\mathbf{k} = \mathbf{k_1} - \mathbf{k_0}$ and $\omega = \omega_1 - \omega_0$, for the purpose of momentum and energy conservation. Results are concluded in the following.

(1) PI process is observed in the nonlinear propagaton of LHWs in a magnetized uniform plasma in GeFi kinetic simulations. The process is found to be very fast within several lower hybrid wave periods.

(2) More than one PI process usually occur simultaneously. Different decay channels are possible to excite wave modes in different PI processes as shown in both Case 1 and Case 2.

(3) Electron is heated and the electron velocity distribution is modified significantly, while ion is not heated and the ion velocity distribution is unchanged. The alteration of electron parallel velocity distribution has significant effects on low frequency wave modes.

5.4 Future work

In order to understand the parametric instability of LHWs in details, more work needs to be accomplished. Since LHWs can interact with both electrons and ions, it is necessary to decouple the electron nonlinear effects and ion nonlinear effects to understand their respective contributions to the parametric instability. Specifically, since the electron is magnetized, the nonlinear coupling in such a system is dominated by a 3-D physics through the $\mathbf{E} \times \mathbf{B}$ drift velocity. The ions, on the other hand, is nearly unmagnetized. Its dynamics may be predominatly in a 2-D fashion. By systematically singling out the electron and ion nonlinear dynamics in both 2-D and 3-D simulations, we could be able to limit the decay channels to understand the 3-D nonlinear physics. GeFi particle simulations with linear electrons and noninear ions, as well as nonlinear electrons and linear ions are planned to perform in the future work. Based on these analysis, more detailed simulation of both nonlinear electrons and nonlinear ions can be performed, and the physics of the parametric instability of LHWs can be understood.

Chapter 6

Summary

In this thesis, propagation of LHWs as the main topic is investigated in great details in two aspects: wave-particle interactions (Landau damping) and wave-wave interactions (parametric instability) of LHWs. As another application of our GeFi model, the excitation of a shear flow driven instability, electron-ion hybrid instability, is also investigated and discussed.

In chapter 1, physics of Landau damping and parametric instability of lower hybrid waves are reviewed. The theory of Landau damping, including both linear and nonlinear Landau damping rates of Langmuir waves, is introduced. Main characteristics of nonlinear Landau damping, such as particles trapping and long time evolution into a final BGK equilibrium, etc, are discussed by referring to some recent published literatures. For lower hybrid wave, the electromagnetic dispersion relation as well as the electrostatic dispersion relation in both cold and warm plasmas is introduced in great details. The coefficient of linear electron Landau damping of LHWs is derived given the condition that the damping rate is much smaller than the real frequency. The important property of Landau damping of LHWs, that unlike most other wave modes LHWs can interact with both electrons and ions directly, is finally discussed. In the last section, theory of PI is reviewed including both electron and ion nonlinear response effects. The nonlinear dispersion relation equation of parametric instability of LHWs is given as Eq. 1.70. Based on the theory and dispersion equation, various decay channels are categorized according to the quantity $k_{\parallel}v_e/\omega$. For various possible decay channels, growth rates are also estimated.

Original novel GeFi plasma simulation model is introduced in chapter 2. This new model, in which the electrons are treated as GK particles and ions are treated as FK particles, is particularly applicable to problems in which wave modes ranging from magnetosonic and Alfvén waves to lower-hybrid/whistler waves need to be handled on an equal footing. To utilize this code, the simulated physical processes should be dominated by wave frequencies $\omega < \Omega_e$, and wave numbers $k_\parallel < k_\perp$. With fast electron gyromotion and Langmuir oscillations removed from the dynamics, the GeFi model can readily employ realistic m_i/m_e mass ratio. As discussed above, the GeFi model has been improved and modified to allow the existence of modes with wavelengths on the same scale of the background nonuniformity.

In chapter 3, simulation results of Landau damping of LHWs from our novel Gyrokinetic electron and Fully kinetic ion (GeFi) model, including linear and nonlinear propagations of LHWs and calculations of driven electric currents in the process, are presented. Main conclusions are summarized in the following. From the simulations of the linear electron Landau damping of LHWs, it is seen the waves decay into the noise level linearly in logarithm. Both the real frequency and the linear electron Landau damping rate from the simulations show excellent agreement with that from the analytical theory of electron Landau damping of LHWs. Both electrons and ions can resonantly interact with the LHWs. The electrons are magnetized, and their resonance condition follows $\omega = k_\parallel v_{e\parallel}$. On the other hand, the ions are highly unmagnetized in the magnetic field of LHWs, and their resonance condition is determined by $\omega = \mathbf{k} \cdot \mathbf{v_i}$. Trapped electrons are observed correspondingly in the nonlinear electron Landau damping, as predicated by the nonlinear theory. In the long time nonlinear evolution of the LHWs associated with the electron Landau damping, the amplitude of the wave becomes oscillatory asymptotically, reaching a final BGK equilibrium. The ion Landau damping, on the other hand, is dominated by the linear physics in the LHW time scales, with nearly no trapped ions in the wave-particle interaction.

In the case with solely ion resonance or the case in which there exist both the ion and the electron resonance, the wave amplitude is significantly reduced by the ion Landau damping. On the long time scales, however, the ions are still weakly trapped. Behaviors of magnetized ions appear, with a frequency $\sim \Omega_i$. As the initial wave amplitude increases, a transition occurs in the electron Landau damping from a strong linear decay of LHWs to a weak decay, which is dominated by the nonlinear physics. Generation of the parallel currents through the ELD from our GeFi simulations is discussed. While the presence of the ion Landau damping results in a smaller $J_{\parallel}$ than that with solely electron Landau damping, similar trends are observed in the dependence of the currents on the initial wave amplitudes for cases with or without the ion Landau damping. The current increases quickly with the initial wave amplitude when the amplitude is small, but slows down when the initial wave amplitude is large.

Investigation of electron-ion hybrid (EIH) instability is presented in chapter 4. With a sheared electron flow in either uniform or nonuniform plasma, the EIH instability mode can be excited. The dispersion equation for EIH mode in uniform plasma is introduced as Eq. 4.17, and the dispersion relation in nonuniform plasma with a density gradient sheared in the length L_n is given in Eq. 4.18. A numerical method is introduced to solve both dispersion equations to obtain the complex eigen functions and eigen values. By this numerical method, a shooting code is programmed in Fortran to numerically calculate the eigen functions and values of the dispersion equations. Various parameters are adopted to obtain the numerical solutions to the dispersion equations, and the results are presented in section 4.1.4. GeFi particle simulation is then used to simulate the EIH instability. Results of EIH instability in a uniform plasma and slab geometry from GeFi particle simulations have very good agreement with the theory. In the cylindrical geometry, frequencies from GeFi particle simulations have good agreement with the theory for a slab geometry, while the growth rates are in the same trend. In the uniform plasma in a cylindrical geometry,

with a finite k_z, GeFi particle simulations indicate that the presence of a finite k_z can significantly change the threshold of EIH instability. The results are consistent with ALEXIS experiments. In the nonlinear GeFi particle simulations of EIH instability in a slab geometry and uniform plasma, the frequency is lower than that in linear simulations. Structures in the real space show that the instability evolves from a short wavelength mode ($k\rho_i \sim 12$) to a longer wavelength mode ($k\rho_i \sim 3$). The nonlinear EIH instability deserves a further study.

Parametric instability of LHWs is discussed in chapter 5. Our GeFi kinetic scheme is used to simulate the process of the parametric decay of LHWs. A constantly driving source in the plasma is used to generate a pump lower hybrid wave with selected wave vector $\mathbf{k_0}$ and frequency ω_0. The single mode simulation shows that the pump wave saturates at a constant amplitude after a certain time. The pump lower hybrid wave is allowed to grow to the saturation level as a single mode before the other wave modes with mode numbers smaller than $(8, 8, 8)$ are released in the system. After the other wave modes are allowed to exist in the system, the pump LHW is found to decay into a lower sideband lower hybrid wave $(\mathbf{k_1}, \omega_1)$ and a wave mode $(\mathbf{k}, \omega)$. The three wave modes follow the selection rules of energy and momentum, $\mathbf{k_1} = \mathbf{k} - \mathbf{k_0}$ and $\omega_1 = \omega - \omega_0$. The growth rates estimated from the simulation is close to that estimated from the theory. The main conclusions can be drawn as following. PI process is observed in the nonlinear propagaton of LHWs in a magnetized uniform plasma in GeFi kinetic simulations. The process is found to be very fast within several lower hybrid wave periods. More than one PI process usually occur simultaneously. Different decay channels are possible to excite wave modes in different PI processes as shown in both Case 1 and Case 2. Electron is heated and the electron velocity distribution is modified significantly, while ion is not heated and the ion velocity distribution is unchanged. The alteration of electron parallel velocity distribution has significant effects on low frequency wave modes.

Bibliography

[1] L. D. Landau, J. Phys.(Moscow), **10**, 25 (1946).

[2] T. M. O'Neil, Phys. Fluid, **8**, 2255 (1965).

[3] N. J. Fisch, Theory of RF Current-Drive, Reviews of Modern Physics, **59**, 175 (1987).

[4] I.B. Bernstein, J.M. Greene, and M.D. Kruskal, Phys. Rev. **108**, 546 (1957)

[5] G. Manfredi, Phys. Rev. Lett., **79**, 2815 (1997).

[6] M. Brunetti, F. Califano, and F. Pegoraro, Phys. Rev E, **62**, 4109 (2000).

[7] J. R. Danielson, F. Anderegg, and C. F. Driscoll, Phys. Rev. Lett., **92**, 245003 (2004).

[8] J.H. Malmberg and C.B. Wharton, Phys. Rev. Lett. **6**, 184 (1964).

[9] R.R.J. Gagné and M.M. Shoucri, J. Comput. Phys. **24**, 445 (1977).

[10] D.R. Nicholson, Introduction to Plasma Theory (*Wiley, New York*, 1983).

[11] K. Miyamoto, Plasma Physics for Nuclear Fusion (*MIT Press, cambridge*, MA, 1987).

[12] G. Brodin, Phys. Rev. Lett. **7**, 78, 1997

[13] C.B. Wharton, J.H. Malmberg, and T.M. O'Neil, Phys. Fluids, **8**, 17, 1968

[14] J.H. Malmberg and C.B. Wharton, Phys. Rev. Lett. 19, 775 (1967).

[15] N.J. Fisch, Theory of RF current-Drive, Reviews of Modern Physics, **59**, 175 (1987).

[16] T. H. Stix, *Waves in Plasmas*, (AIP, New York, 1992).

[17] P. Bonoli, IEEE Trans. Plasma Sci. **12**, 95, (1984).

[18] M. Brambilla, Plasma. Phys. **18**, 669, (1976).

[19] M. Porkolab, Phys. Fluids, **17**, 1432 (1974).

[20] M. Porkolab, Phys. Fluids **20**, 2058, (1977).

[21] V. K. Tripathi, C. S. Liu, and C. Grebogi, Phys. Fluids **22**, 301, (1979).

[22] P. M. Bellan and M. Porkolab, Phys. Fluids **19**, 995, (1976).

[23] M. Porkolab, et al., Phys. Rev. Lett., **53**, 1229, (1984).

[24] J. J. Schuss, Phys. Fluids **18**, 1178, (1975).

[25] R. E. Bell, S. Bernabei, A. Cavallo, et al., Phys. Rev. Lett. **60**, 1294, (1988).

[26] T.H. Stix, Phys. Rev. Lett. **15**, 878 (1965)

[27] A.L. Verdon, Iver H. Cairns, D.B. Melrose, and P.A. Robinson, Phys. Plasmas, **16**, 052105 (2009)

[28] Y.A. Omer'chenko, R.Z. Sagdeev, V.D. Shapiro, and V.I. Shevchenko, Sov. J. Plasma Phys. **15**, 427 (1989)

[29] R. Bingham, J.M. Dawson, and V.D. Shapiro, J. Plasma Phys. **68**, 161 (2002)

[30] J.B. McBride, E. Ott, J.P. Boris, and J.H. Orens, Phys. Fluids **15**, 2367 (1972)

[31] J.F. Drake, J.D. Huba, and N.T. Gladd, phys. Fluids **26**, 2247 (1983)

[32] Y.A. Omel'chenko, R.Z. Sagdeev, V.D. Shapiro, and V.I. Shevchenko, Sov. J. Plasma Phys. **15**, 427 (1989)

[33] I.H. Cairns, Publ. -Astron. Soc. Aust. **18**, 336 (2001)

[34] B.F. McMillan and I.H. Cains, Phys. Plasmas **14**, 012103 (2007)

[35] Y. Lin, X.Y. Wang, Z. Lin and L. Chen, Plasma Phys. Controled. Fusion, **47**, 657-669 (2005)

[36] Y. Lin, x. Y. Wang, L. Chen, X. Lu and W. Kong, Plasmas Phys. Control. Fusion, **53**, 054013 (2011)

[37] Hoshino M, J. Geophys. Res. **92**, 7368 (1987)

[38] P.L. Pritchett, J. Geophys. Res. **106**, 3783 (2001)

[39] H. J. Cai and Lee. L.C. Phys. Plasmas, **4**, 590 (1997)

[40] M.E. Mandt, E.R. Denton and J.F. Drake, Geophys. Res. Lett. **21**, 73 (1994)

[41] Y. Lin and D. W. Swift, J. Geophys. Res. **101**, 19, 859 (1996)

[42] M. Nakamura and M. Scholer, J. Geophys. Res. **105**, 23179 (2000)

[43] Frieman E. A. and Chen L., Phys. Fluids,**25**, 502 (1982)

[44] Brizard A., J. Plasma Phys. **41**, 541 (1989)

[45] S. Wang, Phys. Rev. E **64**, 056404, (2001)

[46] Chen, L., *Waves and Instabilities of Plasmas, World Scientific, 1987, Chap3*

[47] L. Qi and S. Wang, Phys. Plasmas **16**, 062504, (2009)

[48] Lee W.W., J. Comput. Phys., **72**, 243 (1987)

[49] Hahm T.S., Lee W.W. and Brizard A., Phys. Fluids, **31**, 1940 (1988)

[50] N. J. Fisch, Theory of RF Current-Drive, Reviews of Modern Physics, **59**, 175 (1987).

[51] Porkolab, M., 1985a, in *Wave Heating and Current Drive in Plasmas*, edited by V. L. Granatstein and P.L. Colestock (Gordon and Breach, New York), p. 219.

[52] Charles F. F. Karney and Nathaniel J. Fisch, Phys. Fluids **28**, 116 (1985)

[53] C. F. F. Karney, N. J. Fisch, and F. C. Jobes, Phys. Rev. A **32**, 2554C2556 (1985)

[54] Landau, L., Phys. Z. Sowjetunion, **10**, 154 (1936)

[55] Vedenov, A.A., in *Reviews of PLasma Physics*, edited by M.A. Leontovich (Consultants Bureau, New York), Vol. 3, p. 229 (1967)

[56] S. Chandrasekhar, *Hydrodynamic and Hydromagnetic Stability* (Dover, New York, 1981), Chap. XI.

[57] P.G. Drazin and L.N. Howard, in *Advances in Applied Mechanics* (Academic, New York, 1966), Vol. 9, Chap. 1.

[58] A.B. Mikhailovskii, *Theory of Plasma Instabilities* (Consultants Bureau, New York, 1974), Vol. 1, Chap. 1.

[59] A.B. Mikhailovskii, *Theory of Plasma Instabilities* (Consultants Bureau, New York, 1974), Vol. 2, Chap. 1 and 8.

[60] K.C. Shaing and E.C. Crume, Jr., Phys. Rev. Lett. **63**, 2369 (1989).

[61] R.J. Groebner, K.H. Burrell, and R.P. Seraydarian, Phys. Rev. Lett. **64**, 3015 (1990).

[62] P. Song, R.C. Elphic, C.T. Russell, J.T. Gosling, and C.A. Cattell, J. Geophys. Res. **95**, 6375 (1990).

[63] V.K. Tripathi, C. Grebogi, and C.S. Liu, Physics of Fluids, Vol. 20, No. 9 (1977)

[64] L. Chen, R.L. Berger, Nuclear Fusion **17**, 4 (1977)

[65] R.L. Berger and F.W. Perkins, Physics of Fluids, **19**, 3 (1976)

[66] R.Cesario, *et al* Nucl. Fusion **46** (2006) 462-476

[67] R. Cesario, L. Amicucci, D. De Areangelis, M. Ferrari, F. Napoli, E. Pullara, Journal of Physics: Conference Series **260**, 012008 (2010)

[68] H. Romero, G. Ganguli, P. Palmadesso, and P.B. Dusenbery, Geophys. Res. Lett. **17**, 2313 (1990).

[69] G. Ganguli, Y.C. Lee, P.J. Palmadesso, Phys. Fluids, **31**, 4 (1988)

[70] H.Romero, G. Ganguli, Y.C. Lee, P.J. Palmadesso, Phys. Fluids B **4**, 7 (1992).

[71] G. Ganguli, Y.C. Lee, and P.J. Palmadesso, Phys. Fluids, **31**, 10 (1988)

[72] H. Romero, G. Ganguli, and Y.C. Lee, Phys. Rev. Lett. **69**, 24 (1992)

[73] G. Ganguli, M. J. Keskinen, H. Romero, R. Heelis, T. Moore, and C. Pollock, J. Geophys, Res, **99**, 8873 (1994).

[74] K.E. Atkinson, *An Introduction to Numerical Analysis* (Wiley, New York, 1978), Sec. 2.10.